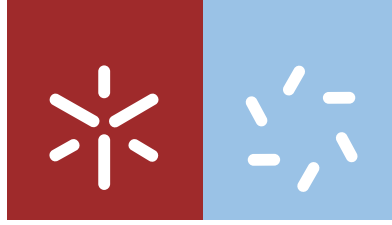


Universidade do Minho
Escola de Ciências

Miguel Matos Ferreira

**Average Lateral Distribution Function
of Muons in 10^{17} eV Extensive Air Showers**



Universidade do Minho
Escola de Ciências

Miguel Matos Ferreira

**Average Lateral Distribution Function
of Muons in 10^{17} eV Extensive Air Showers**

Dissertação de Mestrado
Mestrado em Física
Área de Especialização em Física Aplicada

Trabalho realizado sob orientação do
Professor Doutor António Onofre
e do
Doutor Raul Sarmento

DECLARAÇÃO

Nome: Miguel Matos Ferreira

Endereço electrónico: miguel.ferreira@mfm.net Telefone: 918539693

Número do Bilhete de Identidade: 14150031

Título dissertação: Average Lateral Distribution Function of Muons in 10^{17} eV Extensive Air Showers

Orientador(es): Professor Doutor António Onofre e Doutor Raul Sarmento

Ano de conclusão: 2018

Designação do Mestrado: Mestrado em Física, área de especialização em Física Aplicada

É AUTORIZADA A REPRODUÇÃO INTEGRAL DESTA DISSERTAÇÃO APENAS PARA EFEITOS DE INVESTIGAÇÃO, MEDIANTE DECLARAÇÃO ESCRITA DO INTERESSADO, QUE A TAL SE COMPROMETE;

Universidade do Minho, 10/09/2018

Assinatura: _____

Acknowledgements

First and foremost, I would like to give thanks to my advisor, Professor Raul Sarmento, for all the support, guidance and patience he has given me. It was Raul who showed me the marvels of cosmic rays and for that I will be forever grateful. Such an interesting field.

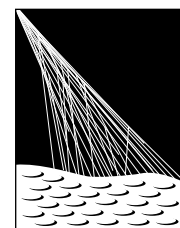
I would also like to thank the Auger group of LIP, for allowing me to work with them and use LIP's infrastructure. A special thanks to Pedro Assis and Luís Mendes.

A special thanks also to Professor Ricardo Ribeiro, for all that he taught me in my bachelor's project.

Finally, I would like to thank everyone who knows me, be it in the academic context or elsewhere.



Universidade do Minho



PIERRE
AUGER
OBSERVATORY

Abstract

Average lateral distribution function of muons in 10^{17} eV extensive air showers

One current debate in the field of high energy cosmic rays is the so called "muon puzzle". Recent studies showed that there is a muon excess of data over simulations. This, allied with the fact that the nature of the primary cosmic ray is sensitive to the muon number, requires a better understanding of the muon component of extensive air showers. In order to have a more precise measurement of this muon component, two RPCs were added below a tank located in the Pierre Auger Observatory, in the Infill array.

The objective of this thesis is to obtain an average muon LDF in 10^{17} eV extensive air showers using those RPCs below the tank. To understand its feasibility and limiting factors, an Heitler-based Monte-Carlo tool was built using a muon LDF parametrization of CORSIKA simulations.

To use data measured by the RPCs, their state had to be validated. For this, the background frequencies in each pad of the RPC were studied. The measured hits are a function of the efficiency of the RPCs. Monitoring data of the RPCs were analyzed to obtain their efficiency over time. To help differentiate between muon hits and EM hits, CORSIKA simulations were analyzed.

Since this is a non-standard experimental setup, the state of the data acquisition system had to be validated.

Resumo

Função de distribuição lateral média de muões para chuviros atmosféricos extensos de 10^{17} eV

Um debate atual na física dos raios cósmicos é o chamado *puzzle* de muões. Estudos recentes mostram que existe um excesso de muões nos dados, quando comparado com o valor respetivo de simulações. Isto, aliado ao facto de que a natureza do raio cósmico primário é sensível ao número de muões, requer um melhor conhecimento da componente muónica de chuviros atmosféricos extensos. Com o objectivo de obter uma medida desta componente muónica, foram instaladas duas RPCs de baixo de um tanque no Observatório de Pierre Auger, no *Infill*.

O objetivo desta tese é obter uma LDF muónica média para chuviros atmosféricos extensos iniciados por uma partícula primária com energia à volta de 10^{17} eV, usando para isso as RPCs de baixo do tanque. De forma a perceber a viabilidade e os fatores limitantes na reconstrução da LDF muónica, foi construída uma ferramenta Monte-Carlo baseada no modelo de Heitler e usando uma parameterização de uma LDF obtida a partir de simulações CORSIKA.

Para usar dados medidos pelas RPCs, o seu estado tem de ser estudado. Para isso, a taxa de fundo foi analisada. Os hits medidos são função da eficiência da RPC. Foram portanto analisados dados de monitorização das RPCs para obter a sua eficiência ao longo do tempo. De forma a diferenciar, nos dados das RPC, muões de partículas electromagnéticas, foram analisadas simulações CORSIKA.

Como a configuração experimental usada não é comum, o estado do sistema de aquisição de dados teve de ser verificado.

CONTENTS

ACRONYMS

XXIII

| | | |
|-------|---|----|
| 1 | INTRODUCTION | 1 |
| 2 | COSMIC RAY PHYSICS | 3 |
| 2.1 | Energy Spectrum | 3 |
| 2.1.1 | Knee Structure | 3 |
| 2.1.2 | Ankle Structure | 4 |
| 2.1.3 | Flux Suppression And The GZK Limit | 6 |
| 2.1.4 | Some Calculations For The GZK Effect | 6 |
| 2.2 | Origin Of Cosmic Rays | 8 |
| 2.3 | Acceleration Mechanisms | 10 |
| 2.3.1 | Bottom-Up Scenarios | 10 |
| 2.3.2 | First And Second Order Fermi Acceleration | 10 |
| 2.3.3 | Top-Down Scenarios | 11 |
| 2.4 | Composition Of UHECRs | 12 |
| 2.5 | Arrival Directions | 13 |
| 2.5.1 | Anisotropy | 14 |
| 2.6 | Shower Components | 14 |
| 2.6.1 | Electromagnetic Component | 14 |
| 2.6.2 | Hadronic Component | 16 |
| 2.6.3 | Muonic Component | 16 |
| 2.7 | Heitler Model | 16 |
| 2.8 | Hadronic Interaction Models | 19 |
| 2.8.1 | Simulations of Extensive Air Showers | 21 |
| 3 | PIERRE AUGER OBSERVATORY | 23 |
| 3.1 | Fluorescence Detectors | 23 |
| 3.2 | Surface Detectors | 25 |
| 3.2.1 | Cherenkov Radiation | 26 |
| 3.3 | Triggers | 27 |
| 3.3.1 | Triggering System of the Fluorescence Detectors | 27 |
| 3.3.2 | Triggering System of the Surface Detectors | 28 |
| | Single detector triggers | 28 |
| | Surface array triggers | 28 |
| 3.4 | Enhancements to the Pierre Auger Observatory | 30 |
| 3.4.1 | AMIGA | 30 |

Contents

| | | |
|-------|--|----|
| 3.4.2 | HEAT | 30 |
| 3.4.3 | Radio Detectors | 31 |
| 3.4.4 | Auger Prime: Surface Scintillator Detectors | 32 |
| 3.5 | Weather Monitorization | 32 |
| 3.6 | Event Reconstruction | 34 |
| 3.6.1 | Shower geometry | 34 |
| 3.6.2 | Lateral Distribution Function (LDF) | 35 |
| 3.6.3 | Energy reconstruction | 36 |
| 3.7 | MARTA | 36 |
| 3.7.1 | Resistive Plate Chambers (RPCs) | 36 |
| 4 | MUONS IN EXTENSIVE AIR SHOWERS | 37 |
| 4.1 | General Summary of Muon Studies | 37 |
| 4.2 | Study of muons with the Pierre Auger Observatory | 38 |
| 4.2.1 | Mean number of muons in highly inclined events | 38 |
| 4.2.2 | Muon Production Depth | 42 |
| 4.2.3 | Testing hadronic interactions | 45 |
| 4.3 | Study of muons with the IceCube/IceTop observatory | 47 |
| 4.4 | Study of muons with the Telescope Array | 51 |
| 4.5 | Study of muons with the EAS-MSU observatory | 54 |
| 5 | TOWARDS AN MLDF AT TdF | 57 |
| 5.1 | Algorithm | 57 |
| 5.2 | Parametrization of a muonic LDF | 58 |
| 5.2.1 | Fit to the CORSIKA Simulations | 59 |
| 5.2.2 | Parametrization of $\beta(E)$ and $N_\mu(E)$ | 62 |
| 5.2.3 | Comparison of a parametrized LDF with full simulations | 63 |
| 5.3 | Monte-Carlo simulation studies | 65 |
| 5.3.1 | Flux of cosmic rays: Number of events | 66 |
| 5.3.2 | Input Distributions | 67 |
| 5.3.3 | Lateral Trigger Probability | 70 |
| 5.3.4 | Output Distributions | 71 |
| 5.3.5 | Reconstruction of the MLDF | 74 |
| 5.3.6 | Stability of fit parameters | 75 |
| 5.4 | Electromagnetic contamination | 75 |
| 6 | DATA ANALYSIS | 81 |
| 6.1 | Experimental Setup | 81 |
| 6.1.1 | Data Acquisition System | 82 |
| 6.2 | T3 requests to TdF | 83 |
| 6.2.1 | Querying CDAS files | 84 |
| 6.2.2 | Querying ADST files | 85 |
| 6.3 | RPC's data | 88 |
| 6.3.1 | Background particles | 88 |

| | | |
|-------|--|-----|
| 6.3.2 | Secondary particles detected by the RPC | 91 |
| 6.3.3 | Density of muons | 95 |
| 6.3.4 | Bridge between RPC's data and reconstructed events | 95 |
| 6.4 | Monitoring of the RPCs | 96 |
| 6.4.1 | Data clean-up and monitoring information | 97 |
| 6.4.2 | Efficiency calculation | 101 |
| 7 | CONCLUSION | 105 |
| | APPENDIX A DISTANCE TO THE SHOWER AXIS | 107 |
| | APPENDIX B RPC'S BACKGROUND DATA | 109 |
| | APPENDIX C RPC'S DATA | 119 |
| | APPENDIX D RPC'S MONITORING DATA | 125 |
| | BIBLIOGRAPHY | 127 |

LIST OF FIGURES

| | | |
|------|---|----|
| 2.1 | Spectrum of cosmic rays with an energy greater than 10^8 eV measured by different collaborations. [5] | 4 |
| 2.2 | Combined energy spectrum measured at the Pierre Auger Observatory and the fitting function with the fitting parameters. The first value of the uncertainty is statistical and the second is systematic. [7] | 5 |
| 2.3 | Proton energy as a function of propagation distance through the 2.7 K CMB for different initial energies. [3] | 7 |
| 2.4 | Magnetic field as a function of the size of the acceleration system. Sources above the red line are able to accelerate protons up to an energy of 10^{21} eV and sources above the green line are able to accelerate iron up to 10^{20} eV. [16] | 9 |
| 2.5 | Comparison of cosmic ray and Solar System nuclear abundances. [20] | 12 |
| 2.6 | The mean (left) and the standard deviation (right) of the X_{\max} distributions measured at Auger as a function of energy compared to air-shower simulations for proton and iron primaries. [23] | 13 |
| 2.7 | Map of the sky in equatorial coordinates, using an Hammer projection, showing the cosmic ray flux above 8 EeV smoothed with a 45° top-hat function. The asterisk represents the galactic center and the dashed line is the galactic plane. [25] | 14 |
| 2.8 | Schematic view of the shower components of an extensive air shower. [26] | 15 |
| 2.9 | Average (a) lateral and (b) longitudinal shower profiles for an air shower produced by a vertical proton of 10^{19} eV. The lateral distribution of the particles at ground is calculated for 870 g cm^{-2} , the depth of the Pierre Auger Observatory. The energy thresholds of the simulation were 0.25 MeV for γ and e^\pm and 0.1 GeV for muons and hadrons. [27] | 15 |
| 2.10 | Scheme view of (a) an electromagnetic cascade and (b) a hadronic cascade. In the hadronic cascade, dashed lines are neutral pions. Diagrams are not to scale. [30] | 17 |
| 2.11 | Inelastic p-p cross section, σ_{inel} as a function of the center of mass energy. The red box indicates the average prediction of all models at 100 TeV. [41] | 21 |
| 2.12 | Per event charged particle probability (within $ \eta < 1$) in inelastic p-p collisions at $\sqrt{s} = 100$ TeV. Full distribution on the right side and zoom at low multiplicities on the left side. [41] | 21 |
| 3.1 | Layout of the Pierre Auger observatory with a representation of the fluorescence detectors and telescopes. [45] | 24 |
| 3.2 | Fluorescence spectrum of nitrogen measured by the AIRFLY collaboration showing the 21 major transitions. [46] | 24 |
| 3.3 | a) Building of a fluorescence detector and its communication tower. b) Scheme of a fluorescence telescope showing its main components. [45] | 25 |

List of Figures

| | | |
|------|--|----|
| 3.4 | a) Surface detector station. b) Scheme of a surface detector station with a description of its main components. [45] | 26 |
| 3.5 | Scheme of the emission of Cherenkov radiation: Cherenkov cone. [1] | 26 |
| 3.6 | Sample of hits, in a PMT matrix, from a real extensive air shower and from noise. [47] | 27 |
| 3.7 | Schematic view of the trigger system of Auger's surface detector array.[48] | 29 |
| 3.8 | Example of T3 configurations. 3-fold T3 mode (ToT2C ₁ &3C ₂) on the left and 4-fold mode (2C ₁ 3C ₂ &4C ₄) on the right. C _n indicates the nth set of neighbors.[48] | 29 |
| 3.9 | Hierarchy of the T4 and T5 triggers of the Auger surface detector. [48] | 30 |
| 3.10 | Schematic view of the AMIGA layout. Plastic scintillators of 30 m ² are buried under $\approx 280g/cm^2$ of vertical mass at each SD tank that make up the infill array, in which surface detectors are distanced by 750 m. The unitary cell indicates a prototype of the muon detectors. [45] | 31 |
| 3.11 | Schematic view of the HEAT telescopes. a) Horizontal mode for calibration and b) Upward mode for shower detection. [45] | 31 |
| 3.12 | Map of the AERA on the left and a photograph of one radio station on the right. [49] | 32 |
| 3.13 | a) Schematic view of a WCD with a scintillator detector on top. b) Schematic view of the scintillator bars. [49] | 33 |
| 3.14 | Schematic figure of the atmospheric monitoring devices in the Pierre Auger Observatory. [45] | 33 |
| 3.15 | Scheme of a) plane shower front and b) spherical shower front. [50] | 34 |
| 4.1 | Expected number of muon hits per SD station as predicted by a reference profile $\rho_{\mu,19}$, for $\theta = 80^\circ$ and $\phi = 0^\circ$, in cylindrical coordinates around the shower axis. [58] | 39 |
| 4.2 | Hybrid events above 4×10^{18} eV and a fit of the power law $\langle R_\mu \rangle = a \langle E/10^{19} \text{ eV} \rangle^b$. The error bars are statistical detection uncertainties. The inset is an histogram of the residuals around the fitted curve (black dots).[58] | 39 |
| 4.3 | Average muon content per shower energy as a function of the shower energy. The circles are data and the black line represents the fit to equation 4.2.4. Square brackets are the systematic uncertainty of the measurement and the diagonal offsets represent the correlated effect of systematic shifts in the energy scale. The grey band is the statistical uncertainty of the fit. The simulated curves are for $\theta = 67^\circ$ for proton and iron primaries. Black triangles at the bottom show the energy bin edges. Different bins have the same number of events.[58] | 40 |
| 4.4 | Average logarithmic muon content $\langle \ln R_\mu \rangle$ as a function of the average shower depth $\langle X_{\max} \rangle$ at 10^{19} eV. Model predictions are obtained from showers simulated at $\theta = 67^\circ$. [58] | 41 |

| | | |
|------|--|----|
| 4.5 | (Left) Comparison of the mean logarithmic muon content $\langle \ln R_\mu \rangle$ at 10^{19} eV obtained from Auger data with model predictions for proton and iron showers simulated at $\theta = 67^\circ$, and for such mixed showers with a mean logarithmic mass that matches the measured $\langle X_{max} \rangle$. The dotted lines represent the interval obtained by adding systematic and statistical uncertainties in quadrature. Brackets indicate systematic uncertainties. (Right) Comparison of the logarithmic gain $d\langle \ln R_\mu \rangle / d \ln E$ between 4×10^{18} eV and 5×10^{19} eV with model predictions, similar as to the graphic on the left. [58] | 42 |
| 4.6 | Geometry used to obtain the traveled distance by a muon and its time delay. [22] | 43 |
| 4.7 | MPD distributions produced by an iron shower with an energy of 10^{19} eV with two different zenith angles, 41° (left) and 60° (right) using EPOS-LHC. The histograms are normalized to have the same maximal height. [22] | 43 |
| 4.8 | $\langle X_{max}^\mu \rangle$ as a function of energy for data (black circles) and simulations by Epos-LHC and QGSJet-II-04 initiated by a proton (red) and an iron (blue). Brackets represent the systematic uncertainty. [22] | 44 |
| 4.9 | Conversion of $\langle X_{max}^\mu \rangle$ and $\langle X_{max} \rangle$ to $\langle \ln A \rangle$ as a function of energy for two reference hadronic models, QGSJet-II-04 (left) and EPOS-LHC (right). Brackets represent systematic uncertainties. [22] | 45 |
| 4.10 | Left: Illustrative measurement of a longitudinal profile with its matching simulated showers, using QGSJet-II-04. Right: Observed and simulated ground signal for the same event. The curves are an LDF fit to the signal. [65] | 45 |
| 4.11 | Best fit values of R_E and R_{had} . The ellipses and gray boxes show the 1σ statistical and systematic uncertainties. R_{had} is the scaling of the hadronic component of the extensive air shower and R_E is the scaling of the EM component. [65] . . . | 46 |
| 4.12 | Sketch of an air shower over the IceCube Neutrino Observatory. [62] | 47 |
| 4.13 | Lateral profiles of muon density as observed in IceTop for near vertical showers (average $\theta \approx 13^\circ$) for several energy bins. The average energy per bin is shown in text. Dotted and dashed lines are estimates based on alternative models used to fit background of non-muon signals. Open dots represent discarded results due to the impact of non-muon background: their systematic uncertainty becomes too large for distances closer to the shower axis. These profiles are results obtained directly from fits of signal distributions without applying any composition-dependent correction. [62] | 48 |
| 4.14 | Top: Muon density at 600 m and 800 m as a function of primary energy for near vertical showers. Lines show the expected values for proton (red) and iron (blue) simulated with CORSIKA and SIBYLL 2.1. Bottom: Same as above but with densities normalized to the expected density for proton showers. Brackets represent systematic uncertainties and the muon densities were corrected for a small composition-dependent bias. [62] | 49 |
| 4.15 | Signal distribution as a function of lateral distance for showers with an energy $4PeV < E < 5PeV$ and a zenith angle $28^\circ < \theta < 32^\circ$. [60] | 49 |

List of Figures

| | | |
|------|--|----|
| 4.16 | Distribution of signals at two fixed lateral distances, 257 m and 646 m. The energy and zenith angle are the same as figure 4.15. The yellow line corresponds to EM particles and the red line to accidental coincidences. The green line represents 1 or more muons and its model is explained in [60]. | 50 |
| 4.17 | (a): Muon density as a function of lateral distances for showers with a zenith angle $\approx 13^\circ$. (b): Interpolated value for 600 m from the shower axis and comparison to the expected simulated value using QGSJet-II-04, EPOS-LHC and SIBYLL 2.1 for two different primary compositions, proton and iron. [60] . . . | 50 |
| 4.18 | Lateral distributions for data and simulations for $30^\circ < \theta < 45^\circ$ and $150^\circ < \phi < 180^\circ$ as a function of distance to the shower axis. The thin vertical error bars are statistical errors while the grey thick error bars represent quadratic sums of statistical and systematic errors. (a) Average signal assuming a Poisson distribution and (b) average ratio of data over simulations. The simulations are for a proton primary.[63] | 51 |
| 4.19 | Same as figure 4.18 but with additional simulations using different hadronic interaction models. (a) In order for the error bars to be easily seen, the plot for the 3 last hadronic interaction models are shifted to the right. (b) Average ratio of data over simulations.[63] | 52 |
| 4.20 | Ratio of signal size of data over simulations for proton and iron primaries using QGSJet-II-03. The vertical thin error bars are statistical errors while the thick shaded bars represent quadratic sums of statistical and systematic errors.[63] | 52 |
| 4.21 | Ratio of the signal size of data over simulations as a function of muon purity for several conditions of the zenith and azimuth angle. The hadronic interaction model used is QGSJet-II-03. The vertical thin error bars are statistical errors while the thick shaded bars represent quadratic sums of statistical and systematic errors.[63] | 53 |
| 4.22 | Distribution of $\rho_\mu(100)$. Points with error bars are data and the blue histogram are MC simulations using QGSJet-II-04 based on a primary composition inferred from surface-detector data (43% protons and 57% iron).[61] | 55 |
| 4.23 | χ^2 per degree of freedom for the muon scaler coefficient, k . Blue line assumes the EAS-MSU surface-detector composition, the green dashed line assumes the KASCADE-Grande composition and the red dotted line the Tunka-133 composition. The horizontal line represents 68% confidence level.[61] | 55 |
| 5.1 | Fit of CORSIKA data set for a proton primary with energy 10^{17} eV. The fit was done using an KASCADE-Grande like function given by equation 5.2.1. The fit parameters can be seen in table 5.2. | 59 |
| 5.2 | Fit of CORSIKA data set for a proton primary with energy $10^{17.5}$ eV. The fit was done using an KASCADE-Grande like function given by equation 5.2.1. The fit parameters can be seen in table 5.2. | 60 |
| 5.3 | Fit of CORSIKA data set for an iron primary with energy 10^{17} eV. The fit was done using an KASCADE-Grande like function given by equation 5.2.1. The fit parameters can be seen in table 5.2. | 60 |

| | | |
|------|--|----|
| 5.4 | Fit of CORSIKA data set for an iron primary with energy $10^{17.5}$ eV. The fit was done using an KASCADE-Grande like function given by equation 5.2.1. The fit parameters can be seen in table 5.2. | 61 |
| 5.5 | Parametrization of β and N_μ as a function of the primary energy, 10^{17} and $10^{17.5}$ eV. All data points are for a proton primary and a zenith angle of 40° | 62 |
| 5.6 | Parametrized LDF given by equation 5.2.5 are in green, blue and purple, and full CORSIKA simulations is in black. Green is with $\beta_H = 0.90$, blue with $\beta_H = 0.87$ and purple $\beta_H = 0.93$. CORSIKA simulations for a proton primary with energy 10^{17} eV and a zenith angle of 40° | 63 |
| 5.7 | Parametrized LDF given by equation 5.2.5 are in green, blue and purple, and full CORSIKA simulations is in black. Green is with $\beta_H = 0.90$, blue with $\beta_H = 0.87$ and purple $\beta_H = 0.93$. CORSIKA simulations for a proton primary with energy $10^{17.5}$ eV and a zenith angle of 40° | 64 |
| 5.8 | Parametrized LDF given by equation 5.2.5 are in green, blue and purple, and full CORSIKA simulations is in black. Green is with $\beta_H = 0.90$, blue with $\beta_H = 0.87$ and purple $\beta_H = 0.93$. CORSIKA simulations for an iron primary with energy 10^{17} eV and a zenith angle of 38° | 64 |
| 5.9 | Parametrized LDF given by equation 5.2.5 are in green, blue and purple, and full CORSIKA simulations is in black. Green is with $\beta_H = 0.90$, blue with $\beta_H = 0.87$ and purple $\beta_H = 0.93$. CORSIKA simulations for an iron primary with energy $10^{17.5}$ eV and a zenith angle of 38° | 65 |
| 5.10 | Distribution of the ground positions generated by the Toy-MC algorithm before the LTP was applied. The point (0, 0) is the position of TdF's detector. | 67 |
| 5.11 | Distribution with the mass of the primary particle generated by the Toy-MC algorithm before the LTP was applied. | 68 |
| 5.12 | Distribution with the zenith and azimuth angles of the primary particle generated by the Toy-MC algorithm before the LTP was applied. | 68 |
| 5.13 | Distribution with the energy of the primary particles generated by the Toy-MC algorithm before the LTP was applied. | 69 |
| 5.14 | Distribution of the surface-distance and distance to the shower axis (minimum distance) of the events to the surface detector before the LTP was applied. | 69 |
| 5.15 | Graphic of equation 5.3.4. Trigger efficiency as a function of energy for proton (upper graphic) and iron (bottom graphic) for different zenith angles. | 70 |
| 5.16 | Distribution of the ground positions generated by the Toy-MC algorithm after the LTP was applied. The point (0, 0) is the position of TdF's detector. | 71 |
| 5.17 | Distribution with the mass of the primary particle generated by the Toy-MC algorithm after the LTP was applied. | 72 |
| 5.18 | Distribution with the zenith and azimuth angles of the primary particle generated by the Toy-MC algorithm after the LTP was applied. | 72 |
| 5.19 | Distribution with the energy of the primary particles generated by the Toy-MC algorithm after the LTP was applied. | 73 |
| 5.20 | Distribution of the surface-distance and distance to the shower axis (minimum distance) of the events to the surface detector after the LTP was applied. | 73 |

List of Figures

| | | |
|------|--|----|
| 5.21 | Distribution of the distance to the shower axis and respective number of particles generated by the Toy-MC algorithm. | 74 |
| 5.22 | Muon lateral distribution function reconstructed/obtained by the Toy-MC. The fit was done by a χ^2 minimization method and begins at 25 m. | 75 |
| 5.23 | Graphics of the relative change of the fit parameters with the acquisition time and number of pads. The default acquisition time is 30 days and the default number of pads is 48. $\delta\beta/\beta$ is the relative uncertainty in β | 76 |
| 5.24 | Average number of EM particles relative to the average number of muons measured by 4 RPCs below WCDs as a function of the core distance. Top is for a proton primary with 10^{17} eV and bottom for a proton primary with $10^{17.5}$ eV. Both for $\theta = 40^\circ$. The simulations consist of 422 events for the top graphic and 498 for the bottom one. The hadronic interaction model used is QGSJet-II-04. | 78 |
| 5.25 | Average number of EM particles relative to the average number of muons measured by 4 RPCs below WCDs as a function of the core distance. Top is for an iron primary with 10^{17} eV and bottom for an iron primary with $10^{17.5}$ eV. Both for $\theta = 38^\circ$. The simulations consist of 438 events for the top graphic and 405 for the bottom one. The hadronic interaction model used is QGSJet-II-04. | 79 |
| 6.1 | Picture of TdF's station. Below the tank there are 2 RPC units, one on top of the other. [74] | 82 |
| 6.2 | Picture representing the position of the two RPCs in TdF's station a zoom of the RPCs. [74] | 82 |
| 6.3 | Left: Scheme of a top view of TdF's station. Light blue represents the Cherenkov tank and in dark blue, numbered from 1 to 3, are the PMTs. In dark-grey are the concrete precasts which serve to lift the tank. Below the tank, represented as green, there are 2 RPCs, one on top of the other. Image is not to scale. Right: Map of pad's positions. | 83 |
| 6.4 | Reconstructed energy of the primary particle for the events that are both in the T3 file and ADST files, had T3 accepted by TdF and in which TdF participates. | 86 |
| 6.5 | Reconstructed zenith angle of the primary particle for the events that are both in the T3 file and ADST files, had T3 accepted by TdF and in which TdF participates. | 87 |
| 6.6 | Distribution of the axis' distance to TdF's station for the events that are both in the T3 file and ADST files, had T3 accepted by TdF and in which TdF participates. | 87 |
| 6.7 | Efficiency of the 3ToT trigger for both the infill and regular array from simulations of iron and proton primaries. [75] | 88 |
| 6.8 | Number of active pads as a function of date for the top (top figure) and bottom (bottom figure) RPCs. | 89 |
| 6.9 | Average value of the background frequency as a function of date for the top (left figures) and bottom (right figures) RPCs, for all channels (top figures) and active channels only (bottom figures). The top figures are TProfiles: the interception of the horizontal bar (width of each bin) with the vertical bar is the mean value of the background and the vertical bar is the standard error on the mean. In the bottom figures, each point represents a single measurement. | 90 |

| | | |
|------|--|-----|
| 6.10 | Distribution of the number of particles considering active pads (9 through 56) for the top RPC. | 91 |
| 6.11 | Distribution of pairs of pad numbers showing cross-talk effects for a multiplicity of 13. As an example if a cosmic ray event triggered pads number 1, 4 and 7 (multiplicity 3), then an entry will be added to (1,4), (1,7) and (4,7). | 92 |
| 6.12 | Map of pad's positions. The pads with a red strike-through are pads that are removed from the analysis due to cross-talk effects. The numbering follows the numbering in the RPC file, for example, 17th bit of the channel's column corresponds to the pad number 17. | 93 |
| 6.13 | Distribution of the number of particles considering pads 9 through 56 with the exception of the pads numbered 9, 16, 17, 24, 25, 32, 33, 40, 41, 48, 49, 52 and 56 for the top RPC. | 93 |
| 6.14 | Rate of events as a function of date for the pads that are not striked-through in figure 6.12. The X-axis are time bins with a width of 24 h and the points are centered in their respective bin. The error bars in the rate of events is \sqrt{Nr} events in bin/ Δt , where Δt is the width of the time bin, in seconds. | 94 |
| 6.15 | Rate of total hits as a function of date. Only 35 pads were used for particle detection. The X-axis are time-bins with a width of 24 h and the points are centered in their respective bin. The error-bars in the flux of particles is \sqrt{Nr} particles in bin/ Δt , where Δt is the width of the time bin, in seconds. | 94 |
| 6.16 | Average multiplicity per bin as a function of date. Only 35 pads were used for particle detection. The X-axis are time-bins with a width of 24 h and the points are centered in their respective bin. The error-bars in the average multiplicity is given by $\left \frac{1}{Nr \text{ events}} \right \times \sqrt{Nr \text{ hits}} + \left \frac{Nr \text{ hits}}{Nr \text{ events}^2} \right \times \sqrt{Nr \text{ events}}$ | 95 |
| 6.17 | Efficiency curve as a function of the reduced electric field. The red line is a fit using a sigmoid function given by equation 6.4.5. The fit parameters are given in table 6.3. | 97 |
| 6.18 | Average voltage for the top RPC as a function of acquisition date. | 98 |
| 6.19 | Average current for the top RPC as a function of acquisition date. | 99 |
| 6.20 | Average temperature for the top RPC as a function of acquisition date. | 99 |
| 6.21 | Average relative humidity for the top RPC as a function of acquisition date. | 100 |
| 6.22 | Pressure for the top RPC as a function of acquisition date. | 100 |
| 6.23 | $R_{cm^2}I$ for the top RPC as a function of acquisition date. $R_{cm^2}I$ was calculated using equations 6.4.3 and 6.4.4 | 101 |
| 6.24 | Effective voltage for the top RPC as a function of acquisition date. V_{eff} was calculated using equation 6.4.2. | 102 |
| 6.25 | Reduced electric field for the top RPC as a function of acquisition date. E/N was calculated using equation 6.4.1. | 102 |
| 6.26 | Efficiency for the top RPC as a function of acquisition date. The efficiency was calculated using the parametrization given by equation 6.4.5. | 103 |
| 6.27 | Efficiency for the top RPC as a function of the reduced electric field. The efficiency was calculated using the parametrization given by equation 6.4.5 and the reduced electric field using equation 6.4.1. | 103 |

List of Figures

| | | |
|-----|---|-----|
| 7.1 | Mind-map of the thesis. The arrow in red represents a bridge that could not be done. | 106 |
| B.1 | Number of particles as a function of date for each pad, from the 1st to the 6th pad. These pads are part of the bottom RPC. | 109 |
| B.2 | Number of particles as a function of date for each pad, from the 7th to the 14th pad. The 7th and 8th pad are part of the bottom RPC. | 110 |
| B.3 | Number of particles as a function of date for each pad, from the 15th to the 22nd pad. | 111 |
| B.4 | Number of particles as a function of date for each pad, from the 23rd to the 30th pad. | 112 |
| B.5 | Number of particles as a function of date for each pad, from the 31st to the 38th pad. | 113 |
| B.6 | Number of particles as a function of date for each pad, from the 39th to the 46th pad. | 114 |
| B.7 | Number of particles as a function of date for each pad, from the 47th to the 54th pad. | 115 |
| B.8 | Number of particles as a function of date for each pad, from the 73rd to the 78th pad as well as the 55th and 56th. The 73rd through the 78th are pads from the bottom RPC. | 116 |
| B.9 | Number of particles as a function of date for pads 79th and 80th, which are pads from the bottom RPC. | 117 |
| C.1 | Number of particles as a function of date for each pad, from the 10th to the 15th pad. | 119 |
| C.2 | Number of particles as a function of date for each pad, from the 18th to the 27th pad with the 24th and 25th pads as an exception. | 120 |
| C.3 | Number of particles as a function of date for each pad, from the 28th to the 37th pad with the 32nd and 33rd pads as an exception. | 121 |
| C.4 | Number of particles as a function of date for each pad, from the 38th to the 47th pad with the 40th and 41st pads as an exception. | 122 |
| C.5 | Number of particles as a function of date for each pad, from the 50th to the 55th pad with the 52nd pad as an exception. | 123 |
| D.1 | Individual temperatures as a function of date of measurement. These figures are post data-clean-up explained in section 6.4.1. | 125 |
| D.2 | Voltage, current and average humidity as a function of date of measurement. These figures are post data-clean-up explained in section 6.4.1. | 126 |

LIST OF TABLES

| | | |
|-----|---|----|
| 2.1 | Basic properties of particle production in p-p collisions at $\sqrt{s} = 100$ TeV. [41] . | 22 |
| 2.2 | Measurement of σ_{p-air} in two energy regions. [42] | 22 |
| 2.3 | Computing time for different thinning levels using CORSIKA. [44] | 22 |
| 3.1 | Atmospheric measurements in the Pierre Auger Observatory and respective instruments. [45] | 34 |
| 4.1 | Comparison of several studies on the muon excess (data over MC). r is the distance to the shower axis and R_0 is 80 m. The difference between the two lines for IceTop are mainly the distance from the shower axis and primary energy. Please see the text below and section 4.3 for the relevant discussion. [61] | 37 |
| 4.2 | Ratio of the observed signal size by the SD to the expected value using simulations with QGSJet-II-03 as a function of the distance to the shower axis, R . Statistical and systematic errors are also shown.[63] | 53 |
| 5.1 | Data sets of CORSIKA used to find a parametrization of a muonic lateral distribution function. The azimuth angle of the primary particle was random in -180° to 180° and the observation level was 1400 m (Auger's altitude) for all sets. There are 100 events for each set. All simulations were done using QGSJet-II-04. | 58 |
| 5.2 | Fit values of the free parameters of the muon LDF function, β and N_μ , and respective uncertainties for each CORSIKA data-set. The number of iterative cycles is the number until convergence was achieved. | 61 |
| 5.3 | Values for $\rho_\mu(450)$ calculated, for each data set, by the functions given by the fits to the CORSIKA data and equation 5.2.5, for different β_h . $\%_{diff}$ is given by equation 5.2.6, where $\beta_h = 0.9$ | 63 |
| 5.4 | Initial conditions for the Toy-MC algorithm. There are 48 active pads in the RPC below the TdF's tank. | 66 |
| 5.5 | Parameters of the infill T4 trigger efficiency model for proton and iron primaries. [70] | 70 |
| 6.1 | Information relative to the comparison of the T3 file with the CDAS files. All numbers are correspondent to cosmic ray data taken between 07/December/2016 and 11/January/2017. % of saved events is the ratio between the number of events in the T3 file and the T3 requests to TdF (obtained by the CDAS) in that time period. | 85 |

| | | |
|-----|--|----|
| 6.2 | Information relative to the comparison of the T3 file with ADST files. All numbers correspond to cosmic ray data taken between 07/December/2016 and 11/January/2017. <i>Hits</i> refers to events that are simultaneously in both the T3 file and in an ADST file. | 86 |
| 6.3 | Parameters of the fit to the RPC's efficiency as a function of the reduced electric field, figure 6.17. The parameters are defined in equation 6.4.5. | 97 |

ACRONYMS

| | |
|-------|--|
| ADST | Advanced Data Summary Tree |
| CDAS | Central Data Acquisition System |
| CR | Cosmic Ray |
| EAS | Extensive Air Shower |
| FD | Fluorescence Detector |
| LDF | Lateral Distribution Function |
| LTP | Lateral Trigger Probability |
| MARTA | Muon Array with RPCs for Tagging Air showers |
| MC | Monte-Carlo |
| MLDF | Muon Lateral Distribution Function |
| PAO | Pierre Auger Observatory |
| RPC | Resistive Plate Chamber |
| SD | Surface Detector |
| TdF | Tierra Del Fuego |
| UHECR | Ultra High Energy Cosmic Ray |
| WCD | Water Cherenkov Detector |

1 INTRODUCTION

Radioactive materials can be detected by using a charged electroscope, which discharges faster when there is emission of charged particles ionizing the air around the electroscope. By using a well insulated electroscope and finding that it still detected ionizing radiation, the idea was that this radiation had an Earth origin. C.T.R. Wilson was one of the first to suggest that the ionization of the atmosphere could be caused by radiation of extra-terrestrial origin. To confirm this hypothesis, he experimented in tunnels and found no reduction in ionization.

Before being challenged by Domenico Pacini, the consensus was still that the atmospheric ionization measured by electroscopes was due to a residual radiation from the crust of the Earth. Pacini found that, for electroscopes placed 3 m underwater, their discharge rate was significantly decreased, by about 20 %. This was in 1910. He concluded that the radiation was not coming from Earth.

Prior to that, in 1909, Theodor Wulf measured the ionization rate at the top of the Eiffel Tower and found that the decrease of the ionization rate, when compared to ground measurements, was too small to confirm the consensus. He still believed the hypothesis that the radiation came from the Earth's crust.

Still in 1909, in Switzerland, Albert Gockel ascended a balloon and made measurements up to 3000 m above sea level. Gockel found that the ionization rate did not decrease with altitude.

The issue was, however, still not closed until Victor Hess established that the radiation causing the atmospheric ionization was from extra-terrestrial origin. In 1912, Hess showed, by using a balloon and an ion chamber, that after a small decrease of the radiation at altitudes near the ground, the penetrating radiation increased with altitude. He reached 5200 m a.s.l. and concluded that the radiation was coming from above. The term *cosmic-ray* was coined by Robert A. Milikan. [1]

The importance of cosmic rays was understood when, in 1933, Carl Anderson discovered *the positive electron* while studying tracks of cosmic ray particles passing through a cloud chamber with a magnetic field.[2] This was the discovery of anti-matter. Many other particles were also discovered due to cosmic rays, such as muons and pions.

In 1938, Pierre Auger and Roland Maze, observed that cosmic ray particles arrived in time coincidence even when separated by distances as large as 20 m. This indicated that the cosmic ray particles that they observed were in fact secondary particles from the same source. This was what was causing the unprompted discharge of the electroscopes. As early as 1962, extremely high energy cosmic rays were being detected, one being of energy 10^{20} eV observed by John Linsley using an array of 8 km² of scintillation counters. [3]

More than 100 years since Victor Hess discovered cosmic rays and they are as interesting as ever.

1 Introduction

This is a thesis in cosmic-rays and it is divided in 7 sections. The 1st section is this [Introduction](#). The 2nd section, [Cosmic Ray Physics](#), is a very brief introduction to the energy spectrum, nature, origin, propagation and current understanding of cosmic-rays. The 3rd section, [Pierre Auger Observatory](#), will present the largest detector of cosmic rays while the 4th section is [Muons In Extensive Air Showers](#), recent measurements of the muon content in EAS. The 5th section, [Towards an MLDF at TdF](#), is a Monte-Carlo study of the expected results for a mean muon LDF at 10^{17} eV extensive air showers measured with a specific-non-standard experimental setup at the Pierre Auger Observatory. This experimental setup uses RPCs and the 6th section, [Data Analysis](#), presents an analysis to the state of both the RPCs and the data acquisition system. This is *ground-work* needed to obtain the so desired MLDF. The 7th and last chapter concludes this thesis.

2 COSMIC RAY PHYSICS

Cosmic rays are high energy particles with extraterrestrial origin. Once they interact with Earth's atmosphere, they produce a shower of secondary particles that may be detected on the surface using, among others, surface detectors. The discovery of cosmic rays is attributed to Victor Hess in 1912, having won the Nobel Prize in Physics in 1936 for this discovery [4]. This chapter will focus on the physics and experimental results of cosmic rays, namely their energy spectrum, composition, arrival directions and shower components. The Heitler model and the importance of muons in high energy cosmic rays will be explained. An introduction will also be made on Hadronic Interaction Models.

2.1 ENERGY SPECTRUM

It can be seen on figure 2.1 that the energy spectrum extends for over 13 orders of magnitude in energy and 32 in flux, going from just a few particles per m^2 per second to less than 1 particle per km^2 per century. Due to this low flux, in order to study the most energetic cosmic rays it is necessary to have a large area of detection with a long operation time.

The cosmic rays' flux can be described by a power law (equation 2.1.1), where γ is the spectral index and is approximately 3.

$$\frac{dN}{dE} \approx E^{-\gamma} \quad (2.1.1)$$

However, there are 2 visible structures in the energy spectrum where the spectral index changes:

- The "Knee" at around $3\text{-}5 \times 10^{15}$ eV; [6]
- The "Ankle" at around 5×10^{18} eV; [7]

For energies below the knee, the spectral index is approximately 2.7 while at energies above the ankle the spectral index is 2.5. Between the knee and the ankle, the spectral index is roughly 3.3.

There's also a region where the spectrum does not follow a power law and a suppression in the flux is visible. The energy at which this suppression occurs is 3.9×10^{19} eV [7] as measured by the Pierre Auger Collaboration. Telescope Array measured a suppression at 6×10^{19} eV [8].

2.1.1 KNEE STRUCTURE

The knee structure is a visible change in the spectral index of the energy spectrum at around $3\text{-}5 \times 10^{15}$ eV. The KASCADE experiment showed that this structure is due to a distinct decrease in the flux of primaries with light mass ($Z < 6$) [9], which can be explained by the Larmor radius,

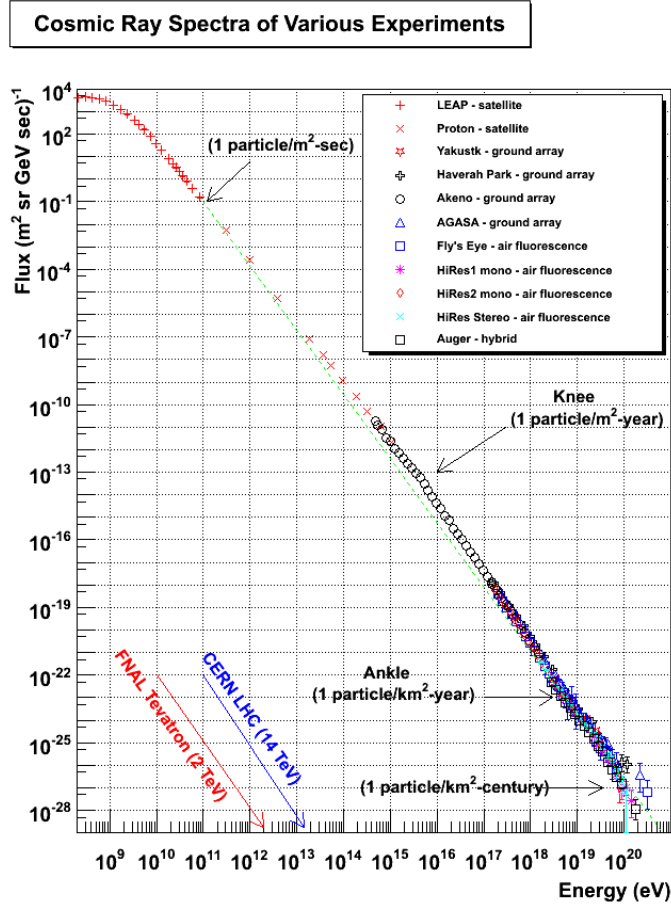


Figure 2.1 – Spectrum of cosmic rays with an energy greater than 10⁸ eV measured by different collaborations. [5]

which is given by $r = \frac{E}{Bc|q|}$, where E , B , c and q are the energy, magnetic field, the speed of light in vacuum and the charge, respectively. The maximum energy that known galactic sources can accelerate cosmic rays. For supernova remnants, the maximum energy that a charged particle could achieve is approximately $300 \times Z$ TeV [1].

Regarding their origin, it is thought that for energies below that of the energy of the knee, the cosmic rays are produced by astrophysical sources in our galaxy. For higher energies the Larmor radius becomes bigger than the radius of our galaxy and so cosmic rays are not confined.

There is also a second-knee as measured by KASKADE-Grande [9] at around 8.32×10^{16} eV. While the knee is thought as being a break in the flux of the light component, the second knee is attributed to being caused by a decrease in the flux of the heavy component.

2.1.2 ANKLE STRUCTURE

The energy of the ankle is currently found to be at $(5.08 \pm 0.06 \pm 0.8) \times 10^{18}$ eV.

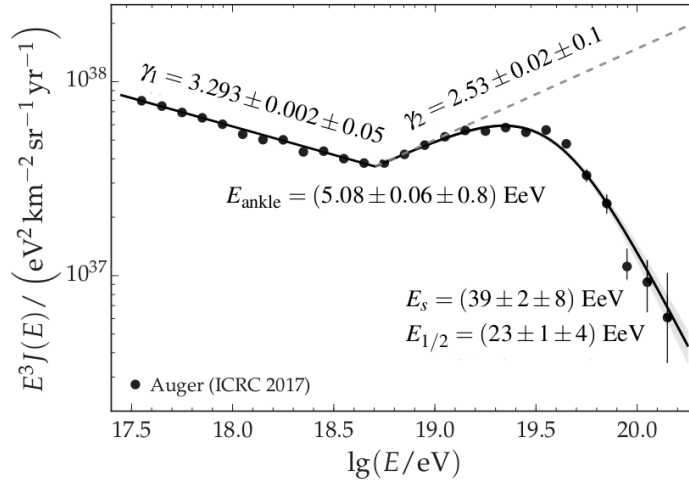


Figure 2.2 – Combined energy spectrum measured at the Pierre Auger Observatory and the fitting function with the fitting parameters. The first value of the uncertainty is statistical and the second is systematic.[7]

In figure 2.2, the spectral parameters are found after fitting the energy spectrum with the following function:

$$E = \begin{cases} J_0 \left(\frac{E}{E_{ankle}} \right)^{-\gamma_1} & E \leq E_{ankle} \\ J_0 \left(\frac{E}{E_{ankle}} \right)^{-\gamma_2} \left[1 + \left(\frac{E_{ankle}}{E_s} \right)^{\Delta\gamma} \right] \left[1 + \left(\frac{E}{E_s} \right)^{\Delta\gamma} \right] & E > E_{ankle} \end{cases} \quad (2.1.2)$$

The energy where the flux suppression occurs is E_s and $E_{1/2}$ is the energy at which the integral spectrum drops by a factor of two below what would be expected with no steepening. E_s is defined as being the energy at which the differential flux falls to half of the value of the extrapolation by the power law for the intermediate region. [7]

The reason for the ankle is not yet understood. There are several models of transition from galactic cosmic rays to extra-galactic cosmic rays such as the ankle models, the mixed composition models and the dip models [10]. The ankle models state that the galactic component is represented by iron, the extra-galactic is assumed to be pure proton and the transition between these two regions occurs at the ankle. The mixed composition models state that the extra-galactic component are nuclei of various types and the transition from GCR to EGCR implies a transition from iron to lighter nuclei of mixed composition. This transition occurs at the ankle or at a nearby energy, such as the second-knee. The dip models consider that the transition from galactic to extra-galactic sources begins at the second knee and is completed at the beginning of the dip ($\approx 10^{18}$ eV), with the dip being a pair production dip of the interaction of protons with the CMB. This latest model assumes an almost pure proton composition above $E \approx 1$ EeV and pure iron composition below.

According to [11], the composition at the ankle region is not pure, it is mixed. Their findings indicate that various nuclei (including masses $A > 4$) are accelerated to ultra-high energies and are

able to escape their source. As such, the dip models (which propose almost pure compositions) are currently disfavored in favor of the mixed composition models.

2.1.3 FLUX SUPPRESSION AND THE GZK LIMIT

As can be seen in figure 2.2, for energies above $\approx 10^{19.5}$ eV the spectrum is not defined by a power law. The energy at which there is a suppression of the flux is 3.9×10^{19} eV.

There are mainly two hypothesis for this cut-off. One of them is that the acceleration mechanisms reached their energy limit and the other is the GZK effect, which can be mimicked by the first.

The Greisen-Zatsepin-Kuzmin limit (GZK limit) is a theoretical upper limit, computed in 1966 independently by Kenneth Greisen [12], Vadim Kuzmin and Georgiy Zatsepin [13], on the energy of cosmic rays produced from distant sources. Its value is 5×10^{19} eV.

This GZK limit comes from the energy loss of cosmic rays from distant sources due to their interaction with the background radiation: the cosmic microwave background (CMB), infrared background (IR) and radio background (RB). Two main processes explain this, pion production and photo-disintegration, by both proton and nuclei.

$$p + \gamma_{CMB} \rightarrow p + \pi^0 \quad (2.1.3)$$

$$p + \gamma_{CMB} \rightarrow n + \pi^+ \quad (2.1.4)$$

$$A + \gamma_{CMB,EBL} \rightarrow (A - nN) + nN \quad (2.1.5)$$

The dominant process is one nucleon emission ($n = 1$) [10].

Figure 2.3 shows the proton energy as a function of the propagation distance through the 2.7 K cosmic microwave background for different initial energies. It can be seen that after traveling for over 100 Mpc in the CMB, the proton will be found with an energy less than 10^{20} eV. A cosmic ray proton with energy greater than 10^{20} eV suggests of a nearby source. Thus, the GZK effect is sensitive to the local deficit of sources [14].

2.1.4 SOME CALCULATIONS FOR THE GZK EFFECT

In this section ¹, the following question will be answered:

- What energy does the proton have to have, in order for the process 2.1.3 to occur?

Knowing that the temperature of the CMB is approximately 2.726 Kelvin [1] and that $E_\gamma = 3K_B T$, with K_B being the Boltzmann constant, the mean energy of a CMB photon is $E_\gamma \approx 7 \times 10^{-4}$ eV.

Since we want the minimum energy the proton can have in order to interact with the CMB photon, we consider the case where the produced proton and the pion will be at rest.

Equation 2.1.6 equals the square of the total 4-momentum in the lab frame (before the collision) with the square of the total 4-momentum of the produced particles in their centre of mass

1. This section's convention is that bold letters represent 4-momentum and the ordinary vectors are presented by an arrow.

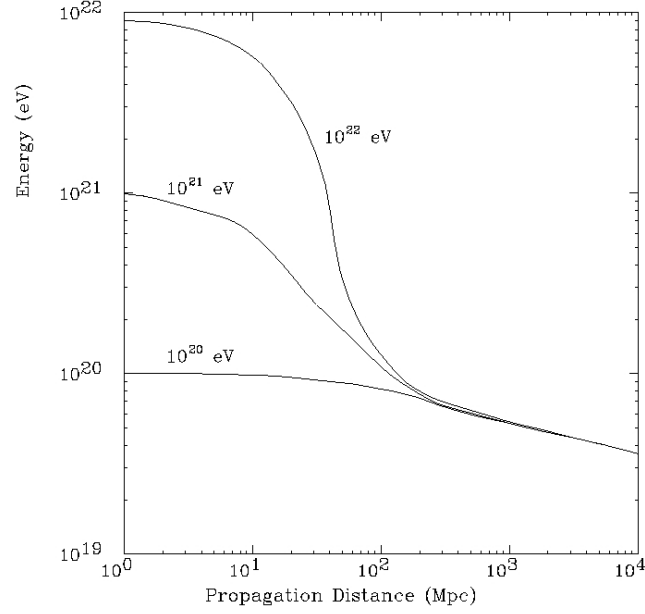


Figure 2.3 – Proton energy as a function of propagation distance through the 2.7 K CMB for different initial energies. [3]

frame (after the collision)². In their centre of mass frame their total momentum is zero and the total energy of the produced particles (proton and neutral pion) is $(M_n + M_\pi)c^2$.

$$(\mathbf{p}_p + \mathbf{p}_\gamma)^2 = (\mathbf{p}'_p + \mathbf{p}_\pi)^2 \quad (2.1.6)$$

$$(\mathbf{p}'_p + \mathbf{p}_\pi)^2 = -(M_p + M_\pi)^2 c^2 \quad (2.1.7)$$

The right hand side of the equation 2.1.6 is known, now it is the left hand side that needs to be solved:

$$(\mathbf{p}_p + \mathbf{p}_\gamma)^2 = \mathbf{p}_p^2 + 2\mathbf{p}_p \cdot \mathbf{p}_\gamma + \mathbf{p}_\gamma^2 \quad (2.1.8)$$

Remembering that the four-momentum of a particle is given by

$$\mathbf{p} = \begin{pmatrix} E/c \\ \vec{p} \end{pmatrix} \quad (2.1.9)$$

the square of the 4-momentum is

$$\mathbf{p} \cdot \mathbf{p} = \mathbf{p}^2 = -\left(\frac{E}{c}\right)^2 + \vec{p} \cdot \vec{p} = -m_0^2 c^2 \quad (2.1.10)$$

2. We can do this because the square of the total four momentum is Lorentz invariant.

2 Cosmic Ray Physics

From the previous equation we see that the square of the four-momentum for the photon is 0, which gives:

$$-M_p^2 c^2 + 2\mathbf{p}_p \cdot \mathbf{p}_\gamma = -(M_p + M_\pi)^2 c^2 \quad (2.1.11)$$

All that is left now is to find the dot product of the 4-momenta of the proton and photon. Knowing that in the highly relativistic regime $E_p = p_p c$, it follows that

$$\mathbf{p}_p \cdot \mathbf{p}_\gamma = -2 \frac{E_p E_\gamma}{c^2} \quad (2.1.12)$$

From equation 2.1.11, we have:

$$M_p^2 c^2 + 4 \frac{E_p E_\gamma}{c^2} = (M_p + M_\pi)^2 c^2 \quad (2.1.13)$$

Solving for E_p gives:

$$E_p = \frac{M_\pi^2 c^4 + 2M_p M_\pi c^4}{4E_\gamma} \quad (2.1.14)$$

Finally, substituting the values of the mass of the proton, neutral pion as well as the energy of a CMB photon, we get:

$$E_p \approx 9.7 \times 10^{19} \text{ eV} \quad (2.1.15)$$

This means that protons with energies higher than E_p will interact with the CMB radiation.

Now that this final expression is known, one can easily find the threshold energy of the proton for the reaction 2.1.4. Doing that, one arrives at the value of $E_p = 1 \times 10^{20}$ eV. Considering only this reaction, protons with energy higher than E_p would never reach Earth because they would interact with photons of the CMB and would convert to a neutron and a charged pion.

2.2 ORIGIN OF COSMIC RAYS

The origin of high-energy cosmic rays is still an open question. The search for the acceleration mechanisms and origin of cosmic rays needs to consider certain constraints, that need to be met in the acceleration sites [15]:

- Geometry: The cosmic ray particle should not leave its source before reaching the required energy;
- Power: The source needs to be able to provide the required energy;
- Radiation losses: The radiation losses in the acceleration field should be smaller than the energy gained by the primary particle;
- Interaction losses: The loss of energy by interaction with other particles should be smaller than the energy gained by the particle in the acceleration field;
- Emissivity: The source needs to have a density and power that can explain the observed flux of cosmic rays;

Considering only the geometric constraint, which is to say that once a particle leaves its source it is unable to gain more energy, the maximum energy that said particle can reach is given by:

$$E_{\max} = qBR\beta \quad (2.2.1)$$

where q is the charge of particle, B is the magnetic field of the acceleration region, $\beta = V/c$ is the velocity and R is the size of the acceleration system. Since it ignores energy losses, it is essentially an upper limit of the energy provided by different astrophysical sources. This equation also considers that the Larmor radius of the particle is smaller than the acceleration site. This equation serves as a base for the well known Hillas plot, which can be seen in figure 2.4.

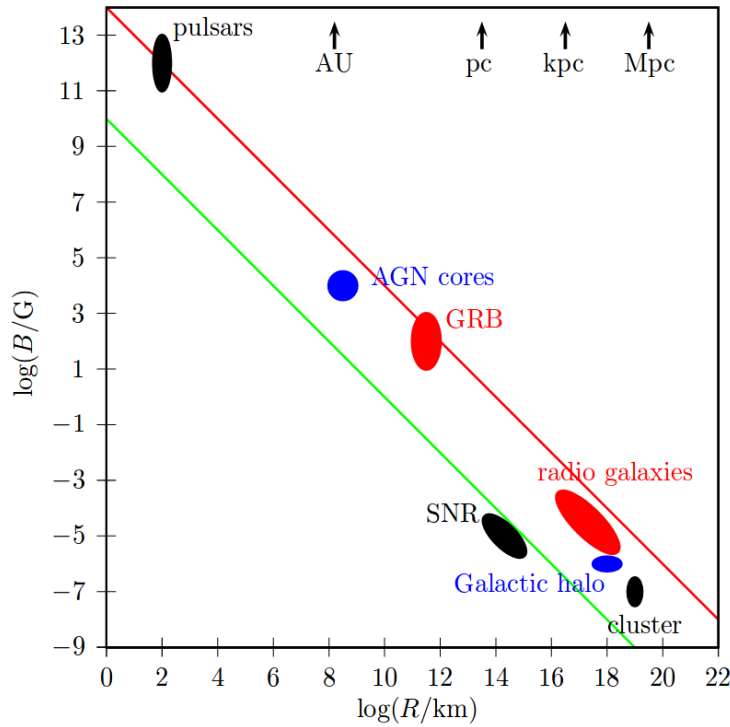


Figure 2.4 – Magnetic field as a function of the size of the acceleration system. Sources above the red line are able to accelerate protons up to an energy of 10^{21} eV and sources above the green line are able to accelerate iron up to 10^{20} eV. [16]

The most promising candidates as the origin of high-energy are cosmic rays gamma ray bursts (GRB) and active galactic nuclei (AGN), such as supermassive black holes. Among others, other possible candidates are supernova remnants, pulsars and jets, lobes, knots and hot spots of powerful active galaxies. [16] [15]

2.3 ACCELERATION MECHANISMS

2.3.1 BOTTOM-UP SCENARIOS

Bottom-up scenarios are proposed in order to explain ultra-high-energy cosmic rays. In bottom-up models, cosmic rays result from the acceleration of particles by astrophysical structures. An example of such a scenario is the Fermi Acceleration Mechanism.

2.3.2 FIRST AND SECOND ORDER FERMI ACCELERATION

In 1949, Fermi proposed a mechanism, now called Fermi-acceleration [17], in which particles could be accelerated in stochastic collisions. This mechanism models acceleration in shock waves, which can be thought as remnants of gravitational collapses.

Let a particle collide with a shock-wave/cloud with energy E_1 and velocity v in the laboratory frame. With $\beta = V/c$, where V is the cloud velocity, E_1^* the energy of the particle in the cloud's frame. Finally, θ_1 is the angle of entry and θ_2 the exit-angle of the particle.

Neglecting the particle's mass with respect to its kinetic:

$$E_1^* = \gamma E_1 (1 - \beta \cos(\theta_1)) \quad (2.3.1)$$

where $\gamma = \frac{1}{\sqrt{1 - v^2/c^2}}$. In the cloud's reference frame, $E_2^* = E_1^*$. In the observer's frame, the energy of the particle after leaving the cloud is

$$E_2 = \gamma E_2^* (1 + \beta \cos(\theta_2)) \quad (2.3.2)$$

Thus, the relative energy change is:

$$\frac{\Delta E}{E} = \frac{E_2 - E_1}{E_1} = \frac{1 - \beta \cos(\theta_1) + \beta \cos(\theta_2) - \beta^2 \cos(\theta_1) \cos(\theta_2)}{1 - \beta^2} - 1 \quad (2.3.3)$$

Inside the cloud, the particle collides many times, which makes its output angle basically random. From that comes:

$$\langle \cos \theta_2 \rangle = 0 \quad (2.3.4)$$

So the average of the relative energy change is given by equation 2.3.5.

$$\left\langle \frac{\Delta E}{E} \right\rangle = \frac{1 - \beta \langle \cos \theta_1 \rangle}{1 - \beta^2} - 1 \quad (2.3.5)$$

The probability of having the cosmic ray collide with the cloud is proportional to their relative velocity:

$$P \propto (v - V \cos \theta_1) \approx (1 - \beta \cos \theta_1) \quad (2.3.6)$$

and so the following is true:

$$\langle \cos \theta_1 \rangle = \frac{\int_{-1}^1 \cos(1 - \beta \cos \theta_1) dx}{\int_{-1}^1 (1 - \beta \cos \theta_1) dx} = -\frac{\beta}{3} \quad (2.3.7)$$

The average energy increase is thus:

$$\left\langle \frac{\Delta E}{E} \right\rangle \approx \frac{4}{3} \beta^2 \quad (2.3.8)$$

This is the second-order Fermi acceleration mechanism. The name "second-order" comes from the fact that the term β is squared.

We now consider the case where instead of a cloud we have a plane shock front moving with velocity $-u_1$. The shocked gas moves away with velocity $-u_2$. In the observers' frame, the gas behind the shock moves to the left with velocity $V = -u_1 + u_2$. The difference between these two cases is in the angular averages. The angles θ_1 and θ_2 have now the constraints $-1 \leq \cos \theta_1 \leq 0$ and $0 \leq \cos \theta_2 \leq 1$, respectively. Their mean values are:

$$\langle \cos \theta_1 \rangle = \frac{\int_{-1}^0 \cos^2 \theta_1 d \cos \theta_1}{\int_{-1}^0 \cos \theta_1 d \cos \theta_1} = -\frac{2}{3} \quad (2.3.9)$$

$$\langle \cos \theta_2 \rangle = \frac{\int_0^1 \cos^2 \theta_2 d \cos \theta_2}{\int_0^1 \cos \theta_2 d \cos \theta_2} = \frac{2}{3} \quad (2.3.10)$$

The energy gain is, in this case (shock wave front):

$$\frac{\Delta E}{E} \approx \frac{4}{3} \beta \quad (2.3.11)$$

This is a first order Fermi-Acceleration. This mechanism explains the cosmic ray energy spectrum better than the second-order mechanism. [1] [18]

2.3.3 TOP-DOWN SCENARIOS

Top-Down scenarios are an alternative to the bottom-up scenarios. These are also candidate explanations to the origin of high energy cosmic rays [19]. The observed isotropy in the arrival directions is a motivation for these models, and they are of two types:

1. Based on heavy relics (for example heavy particles);
2. Based on topological defects;

The first type has heavy relics from the early universe as the base for the UHECRs. They are assumed to decay at the present time, originating the ultra-high-energy-cosmic rays. They are multi-nature, in the sense that they can be heavy particles, black-holes, microscopic fundamental strings, cosmical defects, etc. In order to explain UHECRs, the life-time of these objects has to be the age of the Universe.

The second type is based on the existence of a network of topological defects, which were formed during phase transitions in the early Universe.

Both of these scenarios have a problem: the needed lifetime. Topological defects and heavy particles, would have to have a lifetime in the order of the age of the universe and have to decay in the present time, in order to explain high energy cosmic rays. Their mass has to be the same as the observed cosmic ray, namely in the order of 10^{20} eV/ c^2 .

There is also a scenario based on the annihilation, when they collide, of the relic super heavy particles (wimpzillas).

Top-down scenarios are currently disfavored, because of the following signatures:

- Top-down generated spectra does not follow a power law;
- Nature at the source is mostly gamma rays (which have not yet been observed by Auger) and neutrinos (5 % of the energy is in protons);

2.4 COMPOSITION OF UHECRs

The composition of cosmic rays is one of the biggest open-questions in astro-particle physics. It is known that for lower energies their composition goes "hand-in-hand" with the nuclear abundance in the solar system, with some exceptions, as seen in figure 2.5.

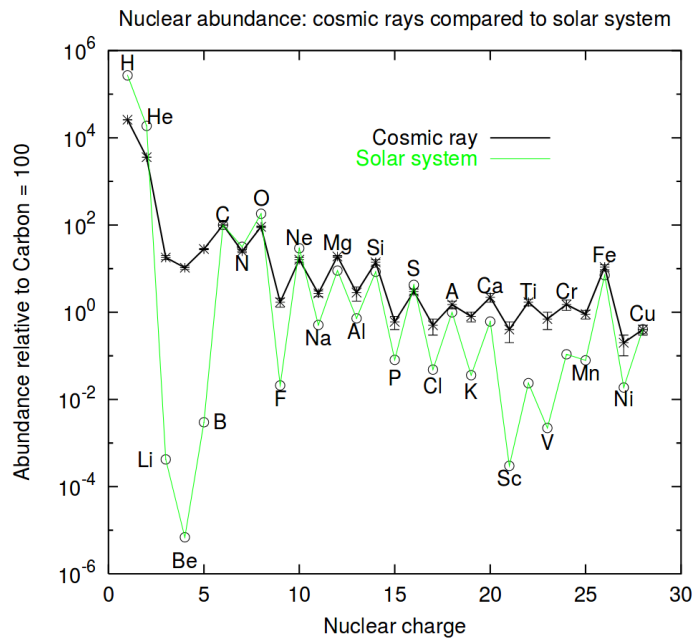


Figure 2.5 – Comparison of cosmic ray and Solar System nuclear abundances. [20]

The exceptions, Lithium, Beryllium and Boron, are thought to be secondary cosmic rays, which is to say that they are produced in the interaction of the heavier primary cosmic rays with interstellar gas, or with Earth's atmosphere, in a process called spallation.

For higher energies, however, the mass composition is an unknown/problem, it is still a matter of study. The main observable used to distinguish between primaries of different mass is

the X_{\max} . X_{\max} is the shower depth of maximum particles, which represents the position in the atmosphere where the shower reaches its maximum size [21].

The mass composition of cosmic rays can be found by comparing measured data with simulations, which rely on extrapolations of accelerator data at energies orders of magnitude below UHECRs. Simulations are thus the biggest source of systematic uncertainties. Data from the Pierre Auger Collaboration disagrees with that from HiRes/TA collaborations. Auger claims a light composition around 3EeV and a gradual increase towards higher energies while HiRes/TA cannot, due to statistical limitations, discriminate between a composition dominated by protons with a changing one. [22]

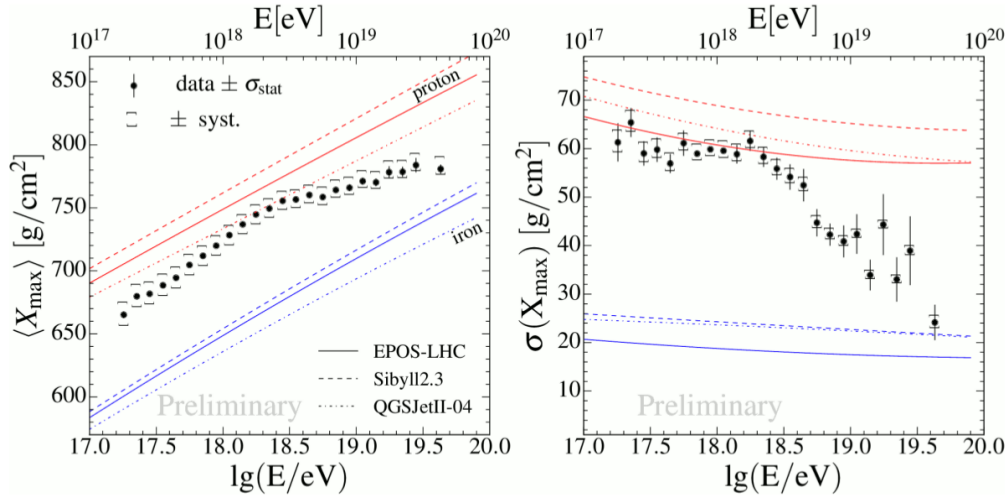


Figure 2.6 – The mean (left) and the standard deviation (right) of the X_{\max} distributions measured at Auger as a function of energy compared to air-shower simulations for proton and iron primaries. [23]

It can be seen in figure 2.6 that between $10^{18.2}$ eV and $10^{18.33}$ eV, the average value of X_{\max} is increasing, which indicates that the average mass of the primary cosmic rays is decreasing (towards proton). At $10^{18.33}$ eV the average value of X_{\max} is increasing with energy at a lower rate than predicted for a constant mass, indicating that the primary mass is increasing.

2.5 ARRIVAL DIRECTIONS

As already mentioned, the origin of high-energy cosmic rays and their acceleration mechanism is still an open question. Empirical evidence of the sources of high-energy cosmic rays come from studying their arrival directions. This is the most direct method available.

The study of the sources of cosmic-rays is not an easy task since they are deflected by magnetic fields and that deflection has an amplitude that is proportional to the atomic number of the cosmic-ray, Z , to the integral along the trajectory of the magnetic field perpendicular to the direction of propagation and to the inverse of their energy. This means that the deflection due to galactic magnetic fields is higher for heavier particles. [24]

2.5.1 ANISOTROPY

Data recorded at the Pierre Auger Observatory between 1 January 2004 and 31 August 2016 was used to find an anisotropy in the arrival directions. Figure 2.7 shows the arrival directions, in equatorial coordinates, for a cosmic-ray flux above 8 EeV and a zenith angle smaller than 80°. A dipole was detected at more than 5.2σ level of significance with an amplitude of $6.5_{-0.9}^{+1.3}\%$ towards right ascension $\alpha_d = (100 \pm 10)$ degrees and a declination $\delta_d = -24_{-13}^{+12}$ degrees. By comparing the magnitude and direction with phenomenological predictions, it was found that it is consistent with an extragalactic origin for these particles. [25]

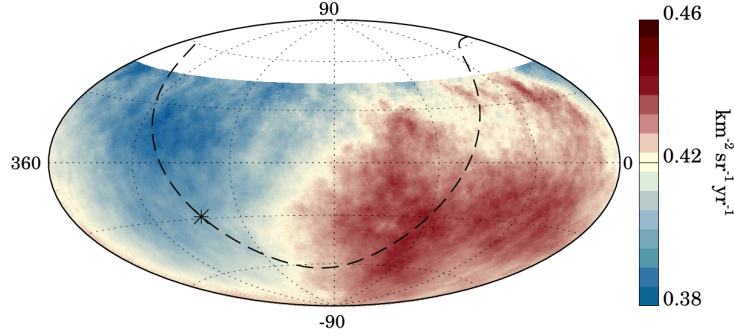


Figure 2.7 – Map of the sky in equatorial coordinates, using an Hammer projection, showing the cosmic ray flux above 8 EeV smoothed with a 45° top-hat function. The asterisk represents the galactic center and the dashed line is the galactic plane. [25]

2.6 SHOWER COMPONENTS

An extensive air shower produced by the interaction of a cosmic ray with a molecule of Earth’s atmosphere will create secondary particles that can be divided into three main components: the electromagnetic, the hadronic and the muonic components. Figure 2.8 is a scheme of these three shower components.

Figure 2.9 shows the lateral and longitudinal shower profiles obtained by using CORSIKA [28] simulations.

2.6.1 ELECTROMAGNETIC COMPONENT

The electromagnetic component of an air shower consists of electrons (e^-), positrons (e^+) and photons (γ), which are mainly the result of pair-production and Bremsstrahlung³ interactions. It can be seen in figure 2.9 that it is the, usually, dominant component of extensive air showers. The main processes involved in the EM component are as follows:

$$\pi^0 \rightarrow \gamma + \gamma \quad (2.6.1)$$

3. Bremsstrahlung radiation, also known as deceleration energy, is the production of electromagnetic radiation by the deceleration of a charged particle when deflected by another. The loss of kinetic energy of the main particle is converted into a photon.

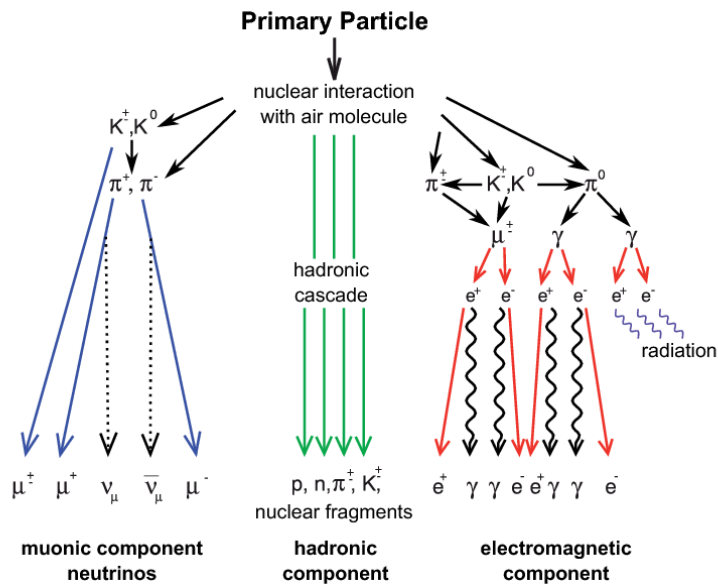


Figure 2.8 – Schematic view of the shower components of an extensive air shower. [26]

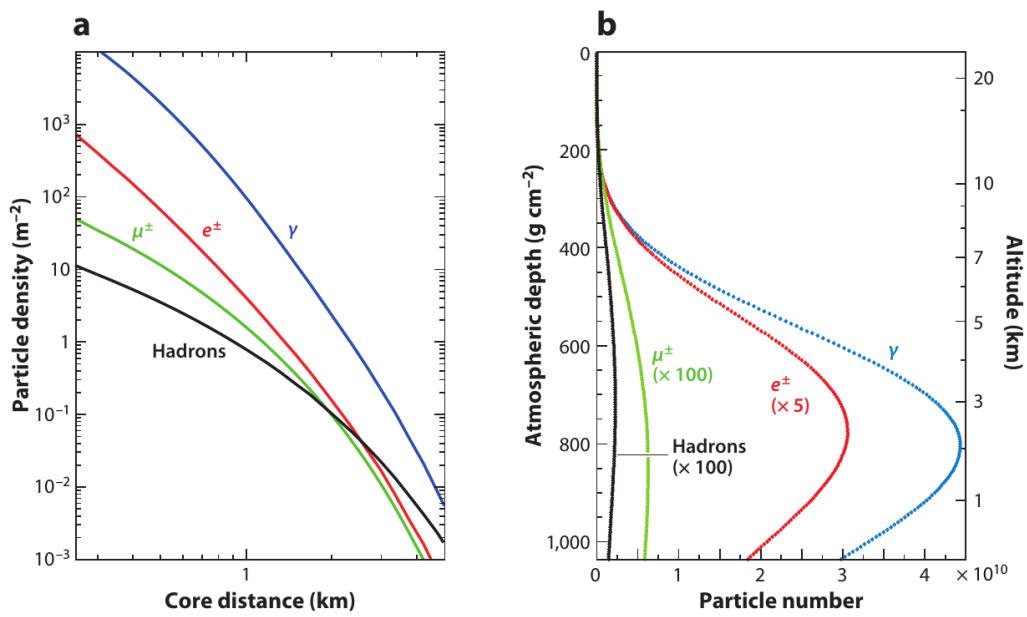


Figure 2.9 – Average (a) lateral and (b) longitudinal shower profiles for an air shower produced by a vertical proton of 10^{19} eV. The lateral distribution of the particles at ground is calculated for $870\ g\ cm^{-2}$, the depth of the Pierre Auger Observatory. The energy thresholds of the simulation were 0.25 MeV for γ and e^\pm and 0.1 GeV for muons and hadrons. [27]

$$\gamma \rightarrow e^+ + e^- \tag{2.6.2}$$

$$\mu \rightarrow \nu_\mu + e + \nu_e \quad (2.6.3)$$

Neutral pions decay into two photons, photons decay into electron-positron pairs and the muon decay is the main source of low-energy electrons at sea level [29].

2.6.2 HADRONIC COMPONENT

Pions and kaons (mesons) are the main secondary particles of the hadronic component. There are other hadronic particles, for example, protons and neutrons (baryons). The neutral pions will decay into two photons and as such will feed the EM component. Charged pions will interact at high energies and decay at low energies. This is because their interaction length is smaller than their decay length. The primary decay modes of charged pions, given by 2.6.4 and 2.6.5, will feed the muon component.

$$\pi^+ \rightarrow \mu^+ + \nu_\mu \quad (2.6.4)$$

$$\pi^- \rightarrow \mu^- + \bar{\nu}_\mu \quad (2.6.5)$$

2.6.3 MUONIC COMPONENT

As seen in the previous section, the muonic component can be fed by the hadronic component by having charged pions decay into muons. The lifetime of a muon is $\tau \approx 2 \mu\text{s}$ and the fact that they reach Earth's surface is an example of time-dilation. For a muon of energy 5 GeV, the distance crossed is roughly 30 km, which is approximately the atmospheric depth.

2.7 HEITLER MODEL

The development of an extensive air shower is so complex that a simple, semi-empirical model to study it is needed: the Heitler model[30].

In high energy cascades, there are two things that make the use of the Heitler model appealing:

1. It is computationally and mathematically simple;
2. It provides good results, in agreement with full simulations;

Despite that, it is not a substitute for full simulations.

Electromagnetic Showers

In the electromagnetic component of Heitler's model, electrons, positrons and photons undergo two-body splittings. The processes involved are electron-positron pair production and/or the loss of energy (by radiating a photon) by electron or positrons. This later process is called Bremsstrahlung⁴.

4. In reality, multiple photons are radiated during this process, not just one.

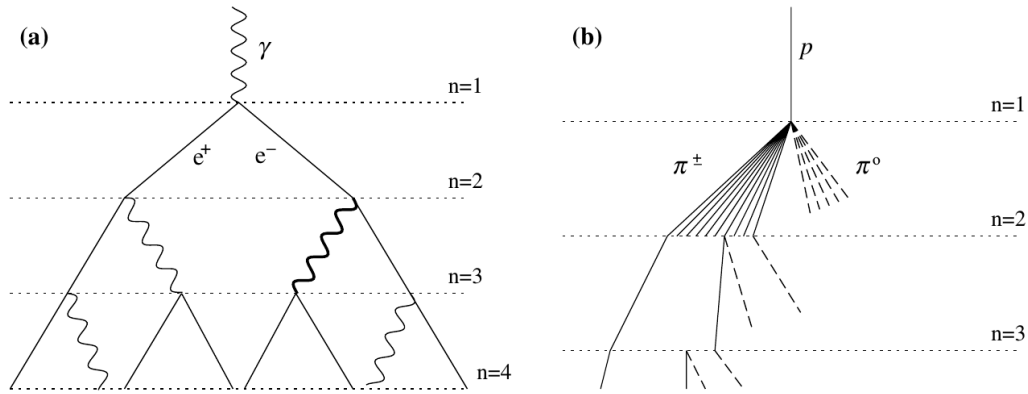


Figure 2.10 – Scheme view of (a) an electromagnetic cascade and (b) a hadronic cascade. In the hadronic cascade, dashed lines are neutral pions. Diagrams are not to scale. [30]

After splitting n times, there are 2^n (N_{\max}) particles in the shower. This splitting process stops when the particles reach a so called critical energy (E_c). When this happens, the average collisional losses exceed the radiative energy losses.

If the primary particle's energy is E_0 , then, after n splittings, the energy per particle is $E_0/2^n$. The total number of particles is, therefore, $2^n = \frac{E_0}{E_c}$. It follows that:

$$n = \frac{1}{\ln 2} \ln \left(\frac{E_0}{E_c} \right) \quad (2.7.1)$$

A splitting length is the average distance that an electron travels before radiating a photon. This distance is $\lambda_r \ln 2$, where λ_r is the radiation length in the medium. After n splittings, the shower depth is $n\lambda_r \ln 2$. Therefore, the X_{\max} is given by:

$$X_{\max} = n\lambda_r \ln 2 = \lambda_r \ln \left(\frac{E_0}{E_c} \right) \quad (2.7.2)$$

In this model, it is assumed that the energy of a particle is equally divided between the two produced particles. It is also important to note that this model does not consider attenuation phenomena, so the detected number of particles is usually different than what is expected from this model. Because of the simplifications of this model, some corrections need to be done to the electromagnetic component, namely in the calculation of the number of electrons from the shower size. This can be more precisely obtained by using $N_e = N/g$, where $g = 10^5$ is a good approximation.

Hadronic Showers

Since cosmic rays are nuclei, an air shower is not usually initiated by an electromagnetic particle. The focus of the remaining of this chapter will be hadron generated showers.

5. This value can be more precise by comparing results of Heitler's model with full simulations

After travelling a length of $\lambda_I \ln 2$, where λ_I is the interaction length, the hadron produces N_{ch} charged pions and $1/2N_{ch}$ neutral pions. Neutral pions decay to photons, which will initiate an electromagnetic shower and charged pions are assumed to decay to muons, after reaching the critical energy as seen in equations 2.6.4 and 2.6.5. The critical energy in this case is the energy at which the decay length of a π^\pm is smaller than the remaining interaction distance. In the hadronic component of a shower, $\frac{1}{3}$ of the energy goes towards π^0 and $\frac{2}{3}$ to π^\pm , which decay to muons.

After n interactions, there will be $(N_{ch})^n$ number of charged particles, where N_{ch} is known as the multiplicity, that is, the number of charged particles generated at each interaction. The energy per charged pion, after n interactions will be $\left(\frac{2}{3}\right)^n \frac{E_0}{(N_{ch})^n}$ and the shower depth is $n\lambda_I \ln 2$. At the critical energy, when production of charged pions stops:

$$n = \frac{\ln\left(\frac{E_0}{E_c}\right)}{\ln\left(\frac{3N_{ch}}{2}\right)} \quad (2.7.3)$$

where n is the number of charged interactions until the critical energy was reached. The number of muons in the shower is obtained by using $N_\mu = N_\pi^+ = (N_{ch})^n$. It follows that

$$N_\mu = \left(\frac{E_0}{E_c}\right)^\beta \quad (2.7.4)$$

$$\text{with } \beta = \frac{\ln N_{ch}}{\ln\left(\frac{3N_{ch}}{2}\right)}.$$

We now consider the X_{\max} , which, as previously discussed, is the point at which the electromagnetic component reach their maximum numbers. For a proton induced shower, the X_{\max} is given by:

$$X_{\max}^p = X_0 + \lambda_r \ln\left(\frac{E_0}{3N_{ch}E_c^e}\right) \quad (2.7.5)$$

with X_0 being the point of first interaction and $X_0 = \lambda_I \ln 2$. Here λ_I is the interaction length of the primary proton.

Nuclear Primaries

The primary particle needs not be a proton, as seen in section 2.4. In the case of a nuclear primary the process is simplified by using a super-position model. In this principle, a nucleus with mass number A and total energy E_0 is divided as A individual nucleons each with E_0/A energy. The resulting air shower is treated as the sum of A separate proton air showers starting at the same point in the atmosphere. According to the super-position principle, the following changes arise:

$$N_\mu^A \propto N_\mu^p A^{1-\beta} \quad (2.7.6)$$

$$X_{max} \propto X_{max}^p - \lambda_r \ln(A) \quad (2.7.7)$$

The consequence of this is that the number of muons increases with the mass of the primary particle and X_{max} goes in the opposite direction, decreases with the mass of the primary, as is observed in figure 2.6.

Up until now it was not considered that upon interaction of two hadrons, one particle (leading particle) can carry a significant fraction of the energy, that is, the energy is not uniformly distributed. The energy of the leading particle is not immediately available for the production of new particles. By correcting this, the N_μ and the X_{max} will be affected. This correction is given by a parameter k , known as the inelasticity of a single interaction. It is the fraction of the total energy directed into new pion production and is given by equation 2.7.8.

$$k = 1 - \frac{E_{lead}}{E_0} \quad (2.7.8)$$

$$\text{With this correction, } N_\mu = \left(\frac{E_0}{E_c}\right)^\beta \text{ but now } \beta = \frac{\ln[1 + N_{ch}]}{\ln[(1 + N_{ch})/(1 - \frac{1}{3}k)]}.$$

2.8 HADRONIC INTERACTION MODELS

An extensive air shower begins with the interaction of the primary cosmic ray with a nucleon of the atmosphere. These hadronic interactions are described by Quantum Chromodynamics (QCD), which is the theory of the strong interaction between quarks and gluons (partons).

Quantum Chromodynamics is a quantum field theory, namely a non-abelian gauge theory with symmetry group SU(3). It is not possible to calculate the bulk of particle production with QCD but processes with large momentum transfer (called "hard processes") are accessible by perturbative methods. Extensive air showers are, however, dominated by soft processes. One has to combine perturbative QCD (pQCD) and general theoretical constraints with phenomenological modeling in order to accurately describe multiparticle production (at accelerator energies) and to make predictions and extrapolate the measured data into unmeasured regions. The free parameters of these models are chosen to agree with accelerators' measurements but the extrapolation of those measurements to unmeasured regions is dependent on the model. The different predictions for the same observable between different hadronic interaction models is an effect of that. [27] In air shower simulations it is necessary to have both low energy models and high energy models. Some frequently used low energy models, which cover energies up to approximately 200 GeV, are GHEISHA, FLUKA [31] [32] and UrQMD [33] [34].

In QCD, a property called color is the analog of the electric charge and gluons are the messenger (or force-carrier). It exhibits two main properties:

- Asymptotic freedom;
- Color confinement;

The property of asymptotic freedom in QCD is the reason for the shared Nobel prize in Physics, in 2004, to David Gross and Frank Wilczek [35] and David Politzer [36]. It is a reduction in the interactions' strength between partons as the energies increase (distances decrease). At

high energies (short distances), quarks interact weakly and perturbative calculations give accurate results.

Partons (quarks and gluons) are never observed as isolated single particles, only as composite particles, with no color. Color confinement is a consequence of the increasing force between two colored particles as the separation between them increases. The distance between the particles requires an ever increasing amount of energy, which will eventually give rise to pair production: a quark-anti-quark pair. In the regime of long distances one has to use phenomenological models since perturbative methods do not apply.

In cosmic ray physics, the majority of the reactions are in the forward region where soft processes dominate. In this region, the Gribov-Regge theory is used, which is an effective field theory supporting multiple actions happening in parallel. In this theory an elementary interaction is represented by a phenomenological object called a pomeron, treated as a quasi-particle. [37]

The two most used models for high energy hadronic interactions are QGSJet and EPOS. The latest version of these models, namely QGSJet-II-04 [38] and EPOS-LHC [39], already reproduce accelerator data. Both of these models are based on Gribov-Regge multiple scattering, QCD and string fragmentation.

EPOS-LHC is a minimum bias Monte-Carlo hadronic generator for heavy ion interactions and cosmic ray shower simulations based on EPOS 1.99 but tuned to reproduce the largest body of accelerator data, LHC data included. It is a consistent quantum mechanical multiple scattering approach based on partons and strings, in which cross sections and particle production are calculated consistently taking into account, in both cases, energy conservation (other models do not consider energy conservation for calculations of cross section).

QGSJet-II-04 is a minimum bias hadronic interaction model optimized for air shower simulations based on Quark-Gluon and Strings model. It has the least number of free parameters in order to reduce extrapolation uncertainties. Due to this, it also has a less detailed description of the final stage of hadronic interactions. [40]

Equation 2.7.5 shows the importance of both the multiplicity of secondary particles and the cross section in the development of an extensive air shower.

The total p-p scattering cross-section is an input parameter in all hadronic interaction models, hence it is well described, as can be seen in figure 2.11, by those very same models at low energies, where data exists. Figure 2.11 also shows that the differences in $\sigma_{inel}(pp)$ between EPOS-LHC and QGSJet-II-04 are small.

Figure 2.12 shows the multiplicity distribution of charged particles produced at central rapidities in inelastic p-p events. It can be seen that EPOS-LHC and QGSJet predict similar yields at low multiplicities ($N_{ch} < 3$) and that the maximum difference between those models, in terms of multiplicity, is in the intermediate region, around $N_{ch} \approx 80 - 130$.

The values for the inelastic cross-section of p-p collisions and respective charged multiplicity are in table 2.1 and in table 2.2 the values for the cross section of p-air in two energy intervals. Despite some differences in the underlying models, the predictions for p-p collisions at $\sqrt{s} \approx 100$ TeV and p-air at these two energy intervals are quite similar.

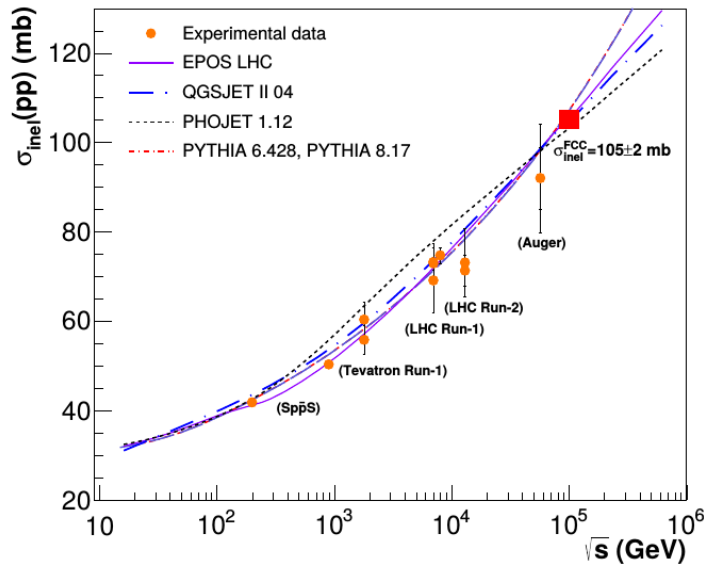


Figure 2.11 – Inelastic p-p cross section, σ_{inel} as a function of the center of mass energy. The red box indicates the average prediction of all models at 100 TeV. [41]

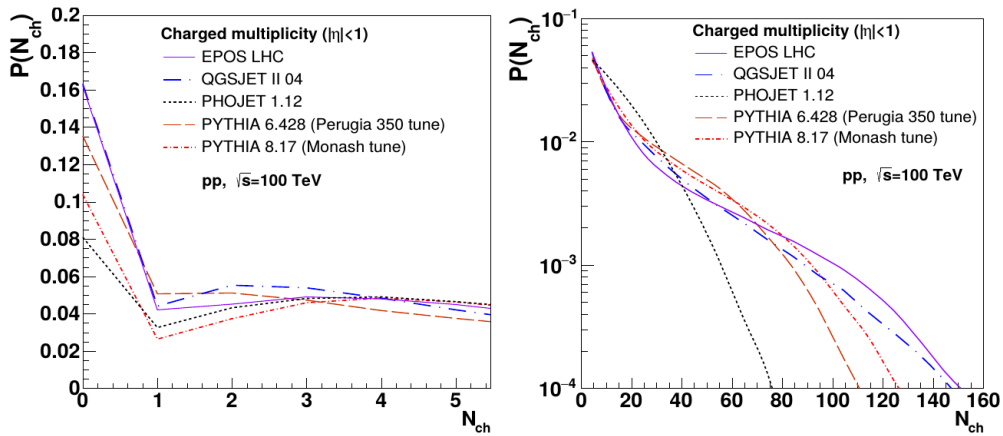


Figure 2.12 – Per event charged particle probability (within $|\eta| < 1$) in inelastic p-p collisions at $\sqrt{s} = 100$ TeV. Full distribution on the right side and zoom at low multiplicities on the left side. [41]

2.8.1 SIMULATIONS OF EXTENSIVE AIR SHOWERS

In the study of extensive air showers, Monte Carlo simulations are a necessary tool. One example of an air shower simulation program is COsmic Ray SIMulations for KAScade (CORSIKA) [28]. The use of MC simulations comes from the fact that an analytical solution to the development of an extensive air shower is not approachable due to this being a multidimensional problem. MC simulations study/follow the development of the shower from the first interaction in the atmosphere until the particles reach the surface and/or particle detectors, following all their

| | EPOS-LHC | QGSJet II |
|---------------------|----------|-----------|
| $\sigma_{inel}(mb)$ | 105.4 | 104.8 |
| N_{ch} | 161 | 152 |
| $P(N_{ch} < 5)$ | 0.35 | 0.36 |
| $P(N_{ch} > 100)$ | 0.025 | 0.018 |

 Table 2.1 – Basic properties of particle production in p-p collisions at $\sqrt{s} = 100$ TeV. [41]

| | EPOS-LHC | QGSJet-II-04 |
|--|----------|--------------|
| $\sigma_{p-air}(mb)$ ($10^{17.8}$ - 10^{18} eV) | 466.1 | 458.7 |
| $\sigma_{p-air}(mb)$ (10^{18} - $10^{18.5}$ eV) | 494.1 | 487.9 |

 Table 2.2 – Measurement of σ_{p-air} in two energy regions. [42]

interactions and decays. Given input parameters such as the primary particle, its direction and energy, the interaction and decay lengths as well as the energy loss of each particle will be determined in each step and a, for example, longitudinal and lateral profile can be given as output.

In MC programs for EAS, the computation time scales roughly with the energy of the primary particle. Thus, for higher energies, the number of secondary particles is such that it is computationally heavy, both in time and resources, to do a full simulation. In order to reduce the computational resources, the thinning method is often used. In the thinning method, all particles with an energy bigger than a demarcation energy are followed but only a fraction of particles with an energy below the demarcation energy. [43] CORSIKA uses this method [44].

The thinning level (or demarcation energy) is an input function defined as a fraction of the primary energy $\epsilon_{th} = E/E_0$. All secondary particles with energy below the demarcation energy are exposed to the thinning procedure. If the energy of all secondary particles falls below the thinning energy:

$$\epsilon_{th} E_0 > \sum_j E_j \quad (2.8.1)$$

only one of the secondary particles will be followed, selected at random as a function of its energy with a probability given by:

$$p_i = \frac{E_i}{\sum_j E_j} \quad (2.8.2)$$

All other secondary particles are discarded. The surviving particle is weighted as $\omega_i = 1/p_i$, in order to not violate energy conservation. In table 2.3, the computational time for different thinning levels for a proton primary with energy $E_0 = 10^{15}$ eV at vertical incident using QGSJet is shown.

| ϵ_{th} | none | 10^{-6} | 10^{-5} | 10^{-4} | 10^{-3} |
|-----------------|------|-----------|-----------|-----------|-----------|
| Time (min) | 98 | 51 | 7.2 | 1.2 | 0.16 |

Table 2.3 – Computing time for different thinning levels using CORSIKA. [44]

3 PIERRE AUGER OBSERVATORY

The Pierre Auger Observatory (PAO) is a cosmic ray observatory located in Argentina, in the province of Mendoza, initially proposed to study the sources of high energy cosmic rays. It was conceived in Dublin in 1991 during the ICRC¹ by Jim Cronin and Alan Watson. A design report with a discussion of the science, design and cost estimate was created in 1995 and, after validating the design with a prototype of 32 surface array detectors and 2 fluorescence detectors, the observatory began production in 2002. In 2004 the Pierre Auger Observatory started obtaining data with 154 active detector stations and the first results were presented in 2005. The observatory was completed in 2008.

The Pierre Auger Observatory is based on an hybrid design. Cosmic rays are detected both by fluorescence telescopes and by a surface array, in complementary ways in order to provide cross-checks and redundancy of measurements. The observatory is located at a mean altitude of approximately 1400 m which corresponds to an atmospheric depth of 875 g cm^{-2} . [45]

This chapter will focus on a brief introduction to the Observatory of Pierre Auger, namely to its hybrid design, trigger system and some of its enhancements.

3.1 FLUORESCENCE DETECTORS

The observatory has 4 fluorescence detector stations, each with 6 fluorescence telescopes, totaling 24 telescopes overlooking the SD array, as can be seen in figure 3.1. The 24 telescopes operate only in dark-moonless nights with favorable weather conditions and each FD is independent of the others, in terms of weather conditions, software and hardware. The on-time of these detectors is about 15%.

The fluorescence telescopes detect fluorescence light by the excitation of N_2 , emitted isotropically by the interaction of nitrogen with a particle of the extensive air shower. Figure 3.2 shows the fluorescence spectrum of nitrogen. It can be seen that most of the photons come from the transition of the 2P band and that when nitrogen relaxes to the ground state, it emits photons mostly in the range 300-400 nm.

A fluorescence telescope has a field of view of $30^\circ \times 30^\circ$, in azimuth and elevation. All 6 telescopes point towards the array in order to provide a coverage of 180° in azimuth. As can be seen in figure 3.3b, a telescope has the following components:

- Shutter;
- Aperture System;
- UV Filter;
- Camera;

1. International Cosmic Ray Conference

3 Pierre Auger Observatory

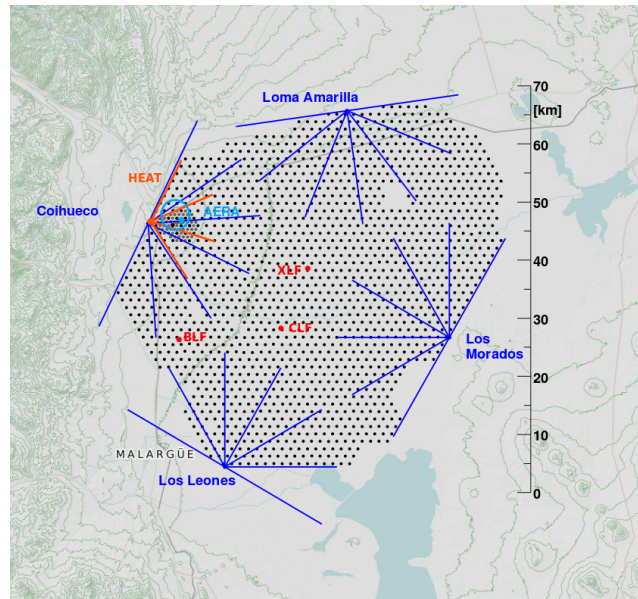


Figure 3.1 – Layout of the Pierre Auger observatory with a representation of the fluorescence detectors and telescopes. [45]

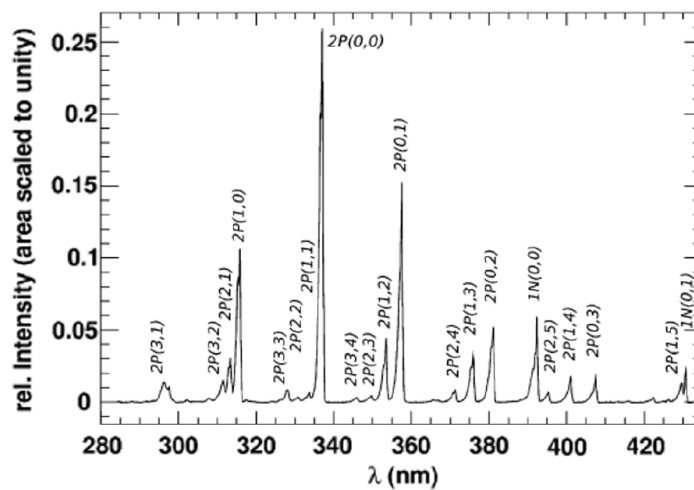


Figure 3.2 – Fluorescence spectrum of nitrogen measured by the AIRFLY collaboration showing the 21 major transitions. [46]

- Electronics;
- Segmented Mirrors;

The shutter is closed during the day-time and is also closed at night in situations when it is raining or there is too much wind. There is also a curtain that acts as a failsafe, in case the shutter malfunctions since the cameras cannot be illuminated by daylight as they are too sensitive. The aperture system has a circular diaphragm of 1.1 m and is covered with a filter.

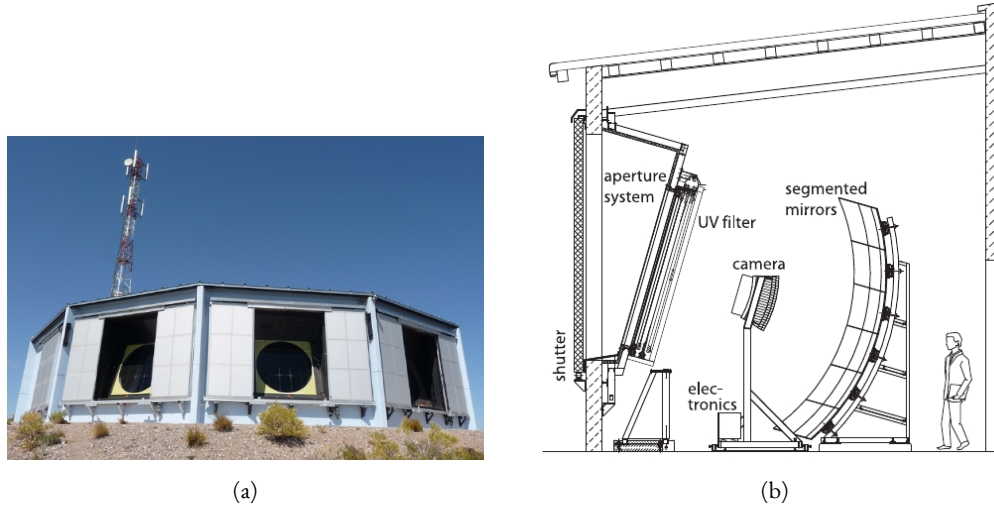


Figure 3.3 – a) Building of a fluorescence detector and its communication tower. b) Scheme of a fluorescence telescope showing its main components. [45]

The objective of the UV filter is to increase the signal-to-noise ratio by filtering the background light flux. Its transmission is above 50% for 310-390 nm and 80% for 330-380 nm. The segmented mirrors form a spherical mirror of 3.4 m radius and focus the light onto the camera, which has 440 pixels in a 22x20 array. Each pixel has a photo-multiplier tube (PMT) with a bialkaline photocathode with a 25% quantum efficiency in the 350-400 nm range.

The electronics of the fluorescence detectors, which are responsible for anti-alias filtering, digitalizing and storing the signals from the PMTs, must have triggers to reject background noise and accept any physically plausible air shower while providing a large dynamic range.

There is one rugged commercial computer (MPC) for each telescope which function is to readout the event data. The computers are connected, per FD site, through an ethernet LAN switch to the site's central computer: EyePC. If a cosmic ray event survives the trigger system, its data is sent from each MPC to the EyePC which then builds an event from the coincident data of all telescopes at a given site.

3.2 SURFACE DETECTORS

The surface detector (SD) array is composed of 1660 water Cherenkov stations placed in a triangular grid with each station separated by 1500 m covering an area of approximately 3000 km². There is also a smaller, denser, SD array in which 61 stations are separated by 750 m, totaling an area of roughly 23.5 km². The goal of this smaller denser array, called Infill array, is to lower the energy range of primary cosmic rays down to 10¹⁷ eV.

A water Cherenkov detector (WCD) can be seen in figure 3.4a. It is a water tank with a diameter of 3.6 m and an height of 1.2 m with its inside surface coated by a reflective sealed liner in order to minimize absorption of photons by the walls of the tank. There are 3 symmetrically distributed PMTs inside the tank, as can be seen in figure 3.4b, to collect and measure the Cherenkov radiation produced by charged particles.

3 Pierre Auger Observatory

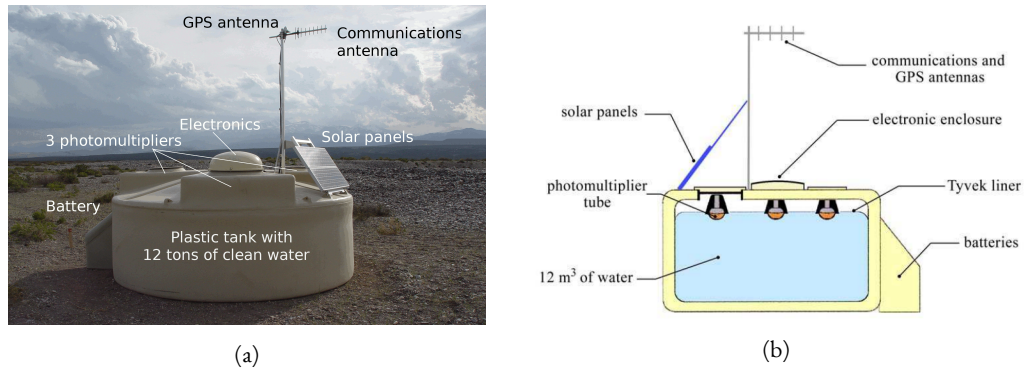


Figure 3.4 – a) Surface detector station. b) Scheme of a surface detector station with a description of its main components. [45]

The solar power, the communications antenna, the battery box and the electronics make each station self-contained. The GPS antenna is for synchronizing and timing events.

3.2.1 CHERENKOV RADIATION

Cherenkov radiation is the name given to the photons emitted by a moving charged particle with velocity higher than that the speed of light in that medium. This radiation has a continuous spectrum. Figure 3.5 shows the emission in a cone of Cherenkov radiation.

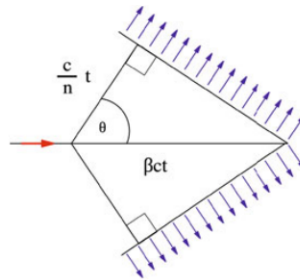


Figure 3.5 – Scheme of the emission of Cherenkov radiation: Cherenkov cone. [1]

Let $\beta = \frac{v_p}{c}$ where v_p is the velocity of the charged particle and c is the speed of light. The distance traveled by the charged particle is given by:

$$d_p = v_p t = \beta ct \quad (3.2.1)$$

while the distance traveled by the Cherenkov photons is given by:

$$x_\gamma = v_\gamma t = \frac{c}{n} t \quad (3.2.2)$$

and thus, the angle of emission from the direction of the moving particle is given by equation 3.2.3.

$$\cos \theta = \frac{1}{n\beta} \quad (3.2.3)$$

The number of photons produced per unit length per unit energy interval of the photons for a particle with charge $z_p e$ and angle θ_c is given by the Frank-Tamm formula, where α is the fine-structure constant. [1]

$$\frac{d^2 N}{dE dx} \approx \frac{\alpha z_p^2}{\hbar c} \sin^2(\theta_c) \quad (3.2.4)$$

3.3 TRIGGERS

Triggers are firmware and software solutions to solve essentially 3 problems:

- Difficulty to save all data;
- Difficulty to analyze all data;
- Difficulty of event detection;

While it may be possible to save and analyze all cosmic ray data and run event detection algorithms on unprofitable data, it's certainly not needed as it is time and resource heavy. By saving only the necessary data, the problem of event analyses becomes much simpler and faster.

3.3.1 TRIGGERING SYSTEM OF THE FLUORESCENCE DETECTORS

Each FD telescopes has 440 first level triggers, one for each PMT, and a single second level trigger. The first level trigger requires that the 10 consecutive signals to be above a threshold, which is determined by the trigger rate itself, ≈ 100 Hz. The second level trigger is purely geometrical. It searches for track segments, within a camera, with a length of at-least 5 pixels. A schematic view of this second level trigger can be seen on figure 3.6.

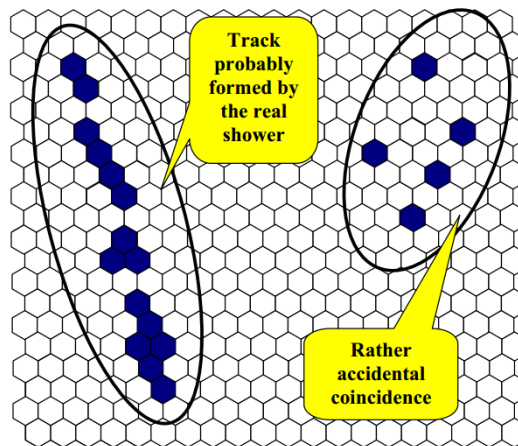


Figure 3.6 – Sample of hits, in a PMT matrix, from a real extensive air shower and from noise. [47]

There is also a third level trigger which selects shower candidates based on track length and space-time requirements and performs a fast reconstruction of the shower geometry. This third level trigger is optimized to filter out noise events such as lightning.

3.3.2 TRIGGERING SYSTEM OF THE SURFACE DETECTORS

The surface detector array has a hierarchical triggering system, as can be seen in figure 3.7. T1 and T2 are single detector triggers. T2 triggers from several detectors are analyzed for possible temporal and spatial correlations and, if positive, the T3 initiates data acquisition and storage.[48]

The common unit for threshold triggers is the $I_{\text{VEM}}^{\text{peak}}$. The Vertical Equivalent Muon (VEM) is a unit that represents the average deposited energy of a muon that crossed the tank from top to bottom going through the center. Such a particle has a characteristic peak in the total charge distribution. The $Q_{\text{VEM}}^{\text{peak}}$ is defined as the bin that contains the peak in a charge histogram of an individual PMT. After converting the charge histogram to a pulse-height histogram in VEM units using a known conversion factor, the $I_{\text{VEM}}^{\text{peak}}$ is defined as the bin containing the peak.[45]

SINGLE DETECTOR TRIGGERS

T1 triggers initiate data acquisition in each WCD. Data is stored (in a local disk) for 10 seconds waiting for a possible T3. There are two T1 triggers, one optimized to detect the electromagnetic component and the other to detect the muonic component of an air shower, complementarily.

The TH-T1, the threshold trigger, requires the coincidence of the 3 PMTs, each above $1.75 I_{\text{VEM}}^{\text{peak}}$ ². This trigger is effective for large signals not necessarily spread in time, for very inclined showers and mostly dominated by the muonic component. TH-T1 reduces the rate to approximately 100 Hz.

The ToT-T1, which stands for time-over-threshold, is for more vertical showers and signals close to the shower axis; the arrival of particles is spread in time. It requires at-least 13 bins in 120 FADC³ bins of a sliding window of $3 \mu\text{s}$ above a threshold of $0.2 I_{\text{VEM}}^{\text{peak}}$ in coincidence of 2/3 PMTs. The average duration of a muonic signal is approximately 150 ns, which makes the ToT of at least 325 ns good at removing the background of random muons. The ToT-T1 rate is smaller than 2 Hz.

The T2 reduces the rate of events per detector to 20 Hz, for bandwidth reasons. In order for a T1-TH to be promoted to a T2, it is required to pass a threshold of $3.2 I_{\text{VEM}}^{\text{peak}}$ in coincidence in the 3 PMTs while a T1-ToT are promoted to T2 without further restrictions.

SURFACE ARRAY TRIGGERS

The T3 begins the central data acquisition from the array. It is done at the CDAS and uses spatial and temporal correlations of T2 triggers. FADC signals from detectors passing the T2 are

2. In a situation where only two (one) PMTs are available, the threshold is 2 (2.8) $I_{\text{VEM}}^{\text{peak}}$

3. FADC stands for Flash Analog to Digital Converters, which are used to digitize the PMT's signals. Each bin of the FADC is 25 ns.

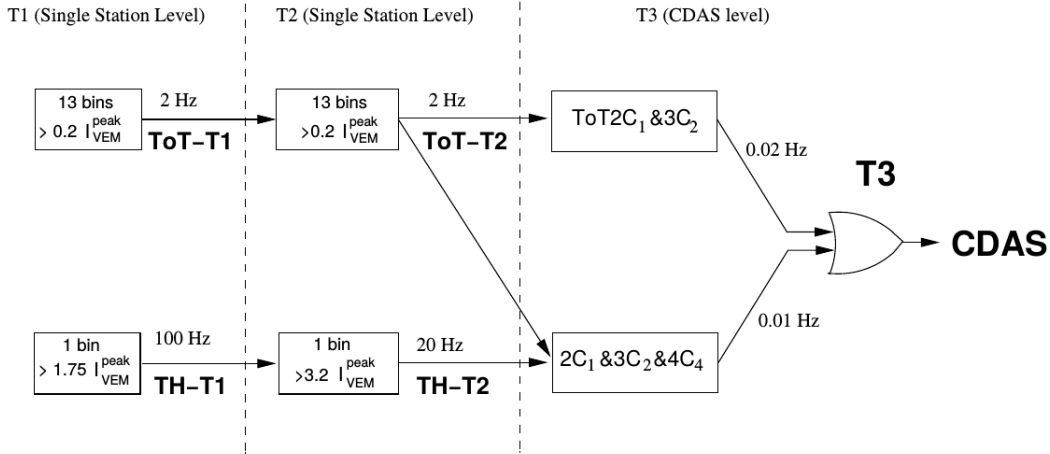


Figure 3.7 – Schematic view of the trigger system of Auger's surface detector array.[48]

sent to the CDAS, along with signals that passed T1 but not T2, as long as they are within $30 \mu\text{s}$ of the T3.

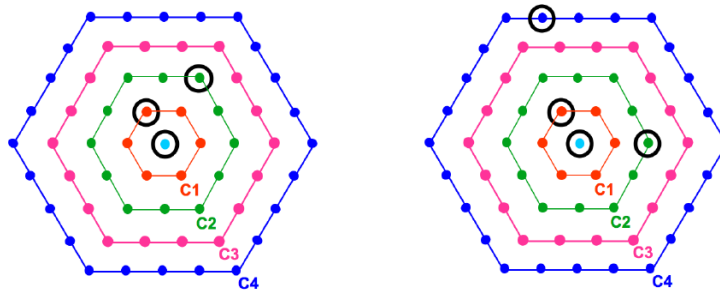


Figure 3.8 – Example of T3 configurations. 3-fold T3 mode ($\text{ToT}2C_1 \& 3C_2$) on the left and 4-fold mode ($2C_1 3C_2 \& 4C_4$) on the right. C_n indicates the n th set of neighbors.[48]

There are 2 types of T3. An example of each type can be seen in figure 3.8:

- 3-fold: $\text{ToT}2C_1 \& 3C_2$;
- 4-fold: $2C_1 3C_2 \& 4C_4$;

These triggers require a spatial and temporal coincidence. 3-fold type requires the coincidence of at least 3 detectors and one of the detectors must have one of its closest neighbors and one of its second closest neighbors triggered. On top of that, each T2 must be within $(6 + 5C_n) \mu\text{s}$ of the first one. The rate of this trigger, with the full array functioning, is 1600 events per day, 90 % of which are real showers.

The 4-fold type requires four-fold coincidence of any T2: one from the first set of neighbors from a selected station, another one in the second set and the last one can be, the farthest, in the 4rd set of neighbors. The rate of this trigger is 1200 events per day, 10% of which are real showers.

There are two additional triggers, the physics trigger, T4, and the fiducial trigger, T5. A scheme of these triggers is shown in figure 3.9.

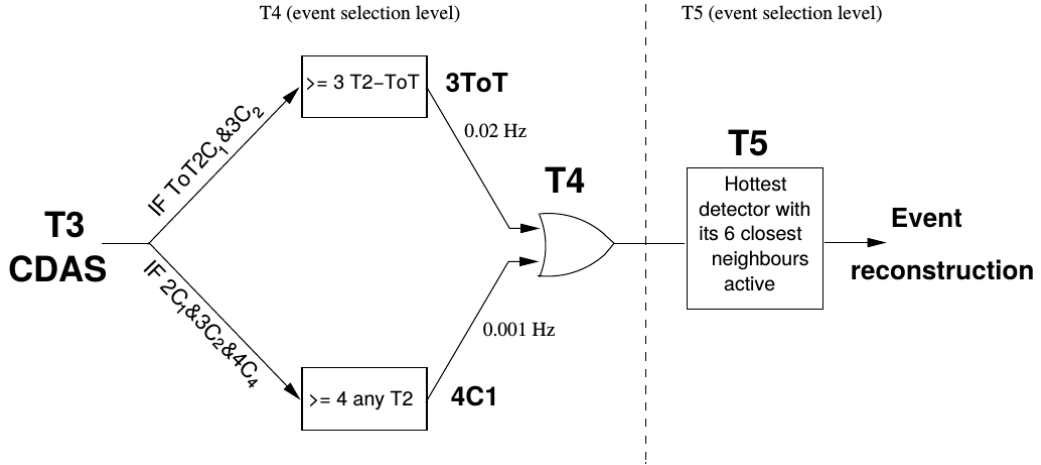


Figure 3.9 – Hierarchy of the T4 and T5 triggers of the Auger surface detector. [48]

The physics trigger, T4, exists to select real showers from the available T3 data. It has two types: 3ToT and 4C1. 3ToT requires that 3 nearby stations pass the T2-ToT in a triangular pattern. It also requires that the 3 stations fit a plane-shower front moving at c . The 4C1 type requires that 4 nearby stations pass any type of T2. It is again required that the 4 stations fit a plane-shower front moving at c .

In order to guarantee the accuracy of the event reconstruction, the fiducial trigger (T5) requires that the shower selected by the T4 is contained within the array boundaries. Namely, it requires that the detector with the highest signal has its closest 6 neighbors active, that is, it must be surrounded by an active hexagon of stations.[48]

3.4 ENHANCEMENTS TO THE PIERRE AUGER OBSERVATORY

3.4.1 AMIGA

The Auger Muons and Infill for the Ground Array, AMIGA, is a project to measure directly the muon component of air showers by using buried scintillator counters. A schematic view of the AMIGA layout is in figure 3.10.

The AMIGA detectors will be located at each of the 61 tanks that comprises the denser 750 m surface detector array. A single SD station will have 3 scintillator modules of 10 m² each. The muon detectors are buried, at a depth of 1.3 m, in order to have the electromagnetic component of an air shower absorbed by the overburden, leaving only the muon component. At that depth, the effective muon energy threshold is 600 MeV/cos θ_μ , where θ_μ is the zenith angle of the muon.

3.4.2 HEAT

In addition to the standard fluorescence telescopes, there are 3 with an elevated field of view, called High Elevation Auger Telescopes, or HEAT. As can be seen in figure 3.11, HEAT can be tilted upward by 29° and were designed to cover an elevation range from 30° to 58°, lowering the

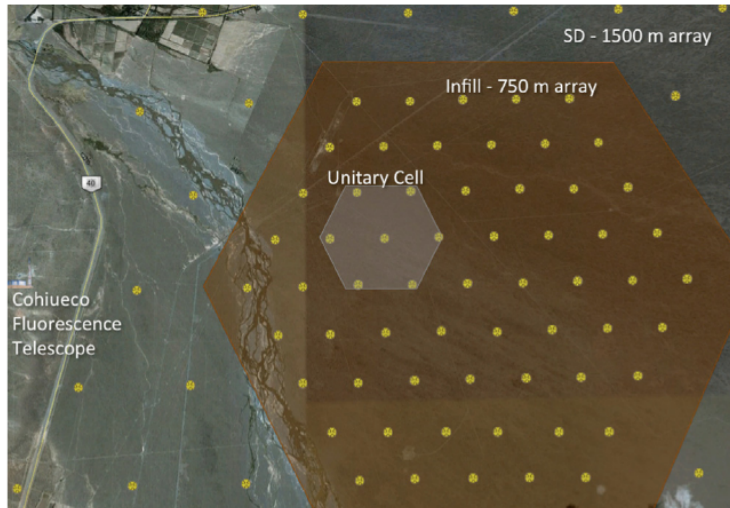


Figure 3.10 – Schematic view of the AMIGA layout. Plastic scintillators of 30 m^2 are buried under $\approx 280 \text{ g/cm}^2$ of vertical mass at each SD tank that make up the infill array, in which surface detectors are distanced by 750 m. The unitary cell indicates a prototype of the muon detectors. [45]

energy range of hybrid air shower measurements to 10^{17} eV when in combination with the SD array.

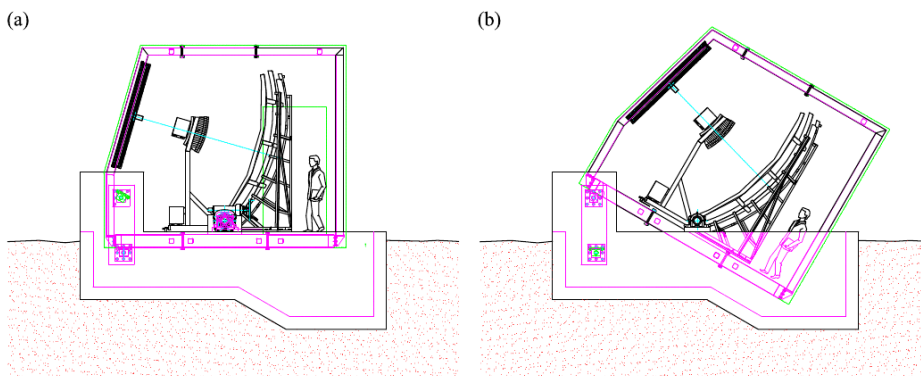


Figure 3.11 – Schematic view of the HEAT telescopes. a) Horizontal mode for calibration and b) Upward mode for shower detection. [45]

3.4.3 RADIO DETECTORS

The Pierre Auger Collaboration has a research program that is trying to understand if radio signals can be used to find the primary energy, mass and arrival direction of cosmic rays with an accuracy at-least as good as other techniques. AERA, Auger Engineering radio array, is comprised of 153 radio detector stations with spacings that range from 150 m to 750 m covering a total area of 17 km^2 . Each radio station has a dual polarization antenna, measuring the electric field in

3 Pierre Auger Observatory

the N/S and E/W directions, an autonomous power system, readout electronics and a fiber optic communication link to a CDAS.

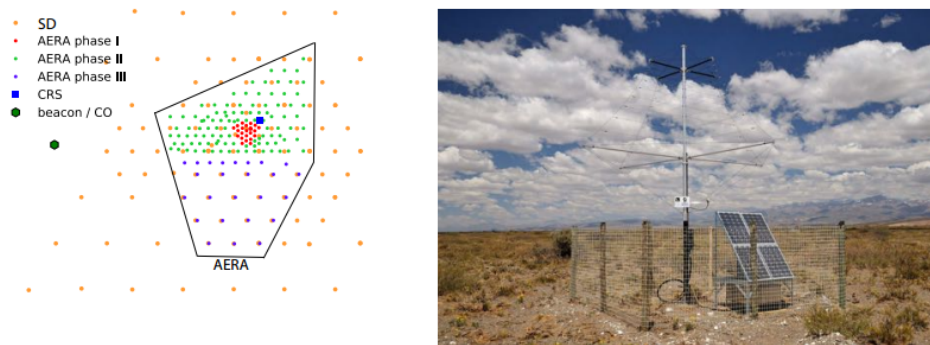


Figure 3.12 – Map of the AERA on the left and a photograph of one radio station on the right. [49]

3.4.4 AUGER PRIME: SURFACE SCINTILLATOR DETECTORS

The main component of the recent Auger upgrade called Auger Prime are the surface scintillator detectors, SSDs. These are 4 m^2 plastic detectors which will be put on top of every water Cherenkov detector. The goal of this upgrade is to measure the muon content of extensive air showers by combining the measurements of both the WCDs and the SSDs, which have different sensitivities to the EM and muonic component of an air shower. The WCDs are dominated by signals from muons and photons and the SSDs are dominated by signals from electrons. Due to this, the time distribution and amplitude of these two types of signals are different, allowing for an indirect analysis with the intent of obtaining a more precise measurement of the muon content of extensive air showers.

The scintillator detectors are based on the scintillation process, which is the emission of luminescence photons by a material after being struck by a particle. The emitted photons will be converted to a signal by the use of read-out wavelength-shifting fibers connected to a single photo-detector. A scheme of an SSD can be seen in figure 3.13b.

The detectors are made of 12 bars of extruded polystyrene scintillator. 1.6 m long, 1 cm thick and 10 cm wide. Each bar has 4 holes in which the fibers can be inserted.

In addition to the SSDs, the SD stations will have upgraded electronics that will increase the data quality, the monitoring and calibration capabilities as well as a better local trigger and processing power (by having an upgraded local station processor). The FD will also receive an upgrade which will allow an increase of $\approx 50\%$ in the duty cycle.

3.5 WEATHER MONITORIZATION

Since the observatory uses the atmosphere as a calorimeter, it is necessary to have ways to monitor it in order to accurately perform reconstruction of air showers. As can be seen in figure 3.14, each FD site has a LIDAR and weather station as well as an Infrared camera. The station

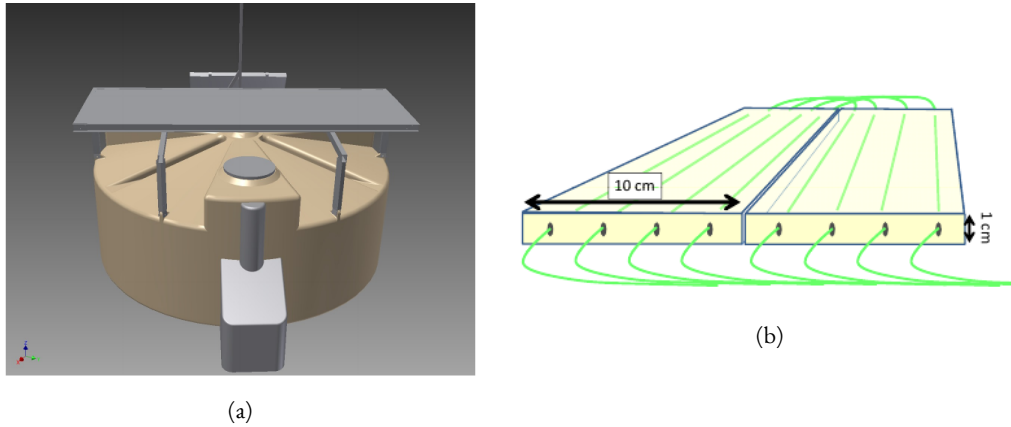


Figure 3.13 – a) Schematic view of a WCD with a scintillator detector on top. b) Schematic view of the scintillator bars. [49]

of Los Morados and Coihueco has an APF (Aerosol Phase Function). There is an Horizontal Attenuation Monitor (HAM) and a ph(F)otometric Robotic Atmospheric Monitor (FRAM) in Los Leones. Additionally, CLF and XLF, Central Laser Facility and eXtreme Laser Facility, respectively, are installed at central positions within the surface array. The variable and frequency that each instrument measures is in table 3.1.

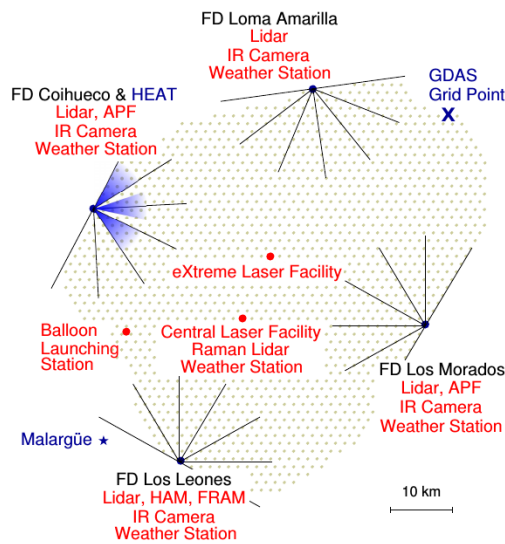


Figure 3.14 – Schematic figure of the atmospheric monitoring devices in the Pierre Auger Observatory. [45]

3 Pierre Auger Observatory

| Category | Variable | Frequency | Instrument(s) |
|----------|--|--------------|------------------|
| State | At ground: pressure, temp., wind, humidity | 5 min | Weather Stations |
| | Profile: pressure, temp., humidity | 3 h | GDAS |
| Aerosols | Vertical optical depth (z) | 1 h | CLF, XLF + FD |
| | Phase function | 1 h | 2 APF units |
| | Angstrom coefficient | 1 h | FRAM (HAM) |
| Clouds | Presence in FD pixels | 15 min | 4 cloud cameras |
| | Behind FD sites | 15 min | 4 lidar stations |
| | Along select tracks | Avg. 1/night | FRAM, lidar |
| | Above CLF/XLF | 1 h | CLF, XLF + FD |

Table 3.1 – Atmospheric measurements in the Pierre Auger Observatory and respective instruments. [45]

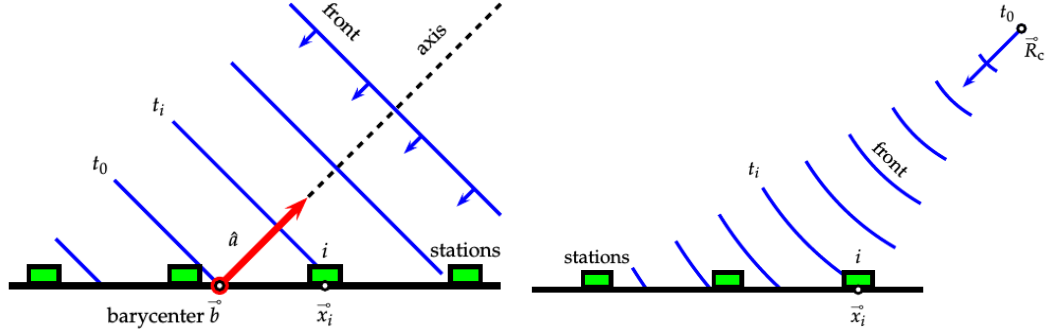


Figure 3.15 – Scheme of a) plane shower front and b) spherical shower front. [50]

3.6 EVENT RECONSTRUCTION

The event reconstruction of the surface detector array uses the times and the size of the signals of individual SD stations. The goal of the SD reconstruction is to obtain the arrival direction and energy of the primary cosmic ray. The main observable obtained from the FD reconstruction is the X_{\max} . For an analysis of the FD reconstruction see [45].

3.6.1 SHOWER GEOMETRY

Using a plane front approximation, one can find the shower axis and the location of the core. The signal-weighted barycenter, \vec{b} , is defined as the spatial origin while the weighted barytime is set as the time origin. A scheme of a plane shower front and a curved shower front is given in figure 3.15.

The evolution of a plane shower front, moving at c , can be written as:

$$-\hat{a}(\vec{x}(t) - \vec{b}) = c(t - t_0) \quad (3.6.1)$$

The shower plane is perpendicular to the shower axis. The time when the shower plane is passing through a point x is given by the projection to the shower axis

$$ct(\vec{x}) = ct_0 - (\vec{x} - \vec{b})\hat{a} \quad (3.6.2)$$

Considering that there is no uncertainty in the station's positions, the only deviation comes from the time uncertainty of the start of the signal, σ_t .

The plane can be fit by minimizing χ^2 using the differences between the measured signal start and the modeled time start. Having the shower axis as $\hat{a} = (u, v, w)$, the station coordinates $\vec{x}_i = (x_i, y_i, z_i)$, $c\sigma_{t_i} = \sigma_i$ and a constraint $u^2 + v^2 + w^2 = 1$, χ^2 is given by equation 3.6.3.

$$\chi^2 = \sum_i \frac{(ct_i - ct_0 + x_i u + y_i v + z_i w)^2}{\sigma_i^2} \quad (3.6.3)$$

A more realistic case is that one of a curved shower front. One can do that by adding a parabolic term, to the previously seen plane fit, that describes the curvature of the shower front near the impact point.

$$ct(\vec{x}) = ct_0 - \hat{a}\vec{x} + \frac{\rho(\vec{x})^2}{2R_c} \quad (3.6.4)$$

where R_c is the curvature radius and $\rho(\vec{x})^2 = (\hat{a} + \vec{x})^2 = x^2 - (\hat{a}\vec{x})^2$ is the perpendicular distance. In this case, the development of the shower front is given by:

$$c(t_i - t_0) = |\vec{R}_c - \vec{x}_i| \quad (3.6.5)$$

where t_0 and \vec{R}_c are the time and spatial origin, respectively, and t_i and \vec{x}_i are the timing and position of the i th station. \vec{R}_c is parametrized as $\vec{R}_c = \vec{c} + R_c \hat{a}$ where R_c is the radius of curvature as measured at the impact point \vec{c} .

To find \hat{a} and R_c , one has to minimize χ^2 which is now given by:

$$\chi^2 = \sum_i \frac{(c(t_i - t_0) - [R_c \hat{a} - \vec{x}_i])^2}{c^2 \sigma_{t_i}^2} \quad (3.6.6)$$

3.6.2 LATERAL DISTRIBUTION FUNCTION (LDF)

Since the surface detector array only detects part of the total shower signal on the ground, one can have the total shower signal on the ground by obtaining an LDF. The LDF relates the signal with the core distance and the most well-known LDF type is the Nishimura-Kamata-Greisen (NKG) function [51] [52], which is of the general form:

$$S(r) = S(r_{opt}) \left(\frac{r}{r_{opt}} \right)^\beta \left(\frac{r + r_1}{r_{opt} + r_1} \right)^{\beta + \gamma} \quad (3.6.7)$$

where β , γ and $S(r_{opt})$ are the fit parameters. $S(r)$ is given in units of VEM⁴, which is the signal that a vertical muon generates. $r_1 = 700$ m and $r_{opt} = 1000$ m for the full array.

4. Vertical Equivalent Muon.

3.6.3 ENERGY RECONSTRUCTION

The energy reconstruction is based on the $S(r_{1000})$. Its value decreases with θ due to the attenuation of the secondary particles in the atmosphere [53]. The $f_{CIC}(\theta)$ is a function that gives the attenuation curve and is given by

$$f_{CIC}(\theta) = 1 + ax + bx^2 + cx^3 \quad (3.6.8)$$

with $a = 0.980 \pm 0.004$, $b = -1.68 \pm 0.1$, $c = -1.30 \pm 0.45$ and $x = \cos^2 \theta - \cos^2 \bar{\theta}$ where $\bar{\theta}$ is the median angle [45]. Now converting S_{1000} to a reference signal size, $S_{38} = S_{1000}/f_{CIC}(\theta)$, one can find the event's energy, for hybrid events, in two complimentary and independent ways:

$$E_{FD} = A(S_{38})^B \quad (3.6.9)$$

where A and B are fit parameters from the data of S_{38} as a function of the E_{FD} , obtained with the maximum-likelihood method, and are $A = (1.90 \pm 0.05) \times 10^{17}$ eV and $B = 1.025 \pm 0.007$. The SD energy estimator is

$$E_{SD} = A \left(\frac{S_{1000}}{f_{CIC}(\theta)} \right)^B \quad (3.6.10)$$

3.7 MARTA

MARTA, which stands for Muon Array with RPCs for Tagging Air showers, is a hybrid detector implemented by LIP in some stations from the surface array. It consists in the addition of resistive plate chambers (RPCs) under the water Cherenkov detectors. The WCDs will act as a shield to the RPCs, absorbing most of the electromagnetic component of an air shower, leaving the muonic component to be assessed by the RPCs. [54]

A more detailed description of the experimental setup used in this thesis, in a tank called *Tierra Del Fuego*, will be given in chapter 6.1.

3.7.1 RESISTIVE PLATE CHAMBERS (RPCs)

In the framework of the Pierre Auger Observatory, resistive plate chambers (RPCs) have been proposed as a muon detector, to better understand the muonic component of extensive air showers.

An RPC is a particle detector made of at-least two high-resistivity and parallel electrode plates which produce a constant and uniform electrical field. The space between the two electrodes is filled with a gas and an avalanche of electrons will be created after a charged particle ionizes the atoms of the gas, creating a signal that will be measured by the read-out pads. The gas has a high absorption coefficient in order to avoid the propagation of photons created in a discharge thus avoiding secondary discharges in other points of the detector. [55]

More information regarding the RPCs used in the experimental setup will be given in chapter 6.1.

4 MUONS IN EXTENSIVE AIR SHOWERS

This chapter will focus on the importance of muons in cosmic ray physics, namely in the mass composition, and will present some recent results in regards to their measurements.

First, a general summary of a possible muon excess of data over simulations will be presented and then three measurements done by the Pierre Auger Collaboration, two by the IceCube observatory, one by Telescope Array and one by EAS-MSU will be shown.

4.1 GENERAL SUMMARY OF MUON STUDIES

High-energy cosmic rays provide us with the ability to study hadronic interactions at energies which are not yet available in man-made colliders; hadronic interaction models are thus based on extrapolations. As such, models of hadronic interactions are often not in accordance with the measured showers' observables. One such case is the number of muons. The expected number of muons based on simulations is lower than the number of muons actually measured.

This phenomena of muon excess is seen not only by the Auger Collaboration but also by other experiments, as can be seen in table 4.1.

| Experiment | Altitude (m) | E (eV) | E_μ (GeV) | r/R_0 | Muon excess |
|--------------------|--------------|------------------------|----------------|--------------|-------------|
| HiRes-MIA [56] | 1500 | 10^{17} to 10^{18} | $\gtrsim 0.85$ | $\gtrsim 1$ | yes |
| PAO [57] [22] [58] | 1450 | $\gtrsim 10^{19}$ | $\gtrsim 1$ | $\gtrsim 10$ | yes |
| Yakutsk [59] | 100 | $\gtrsim 10^{19}$ | $\gtrsim 1$ | $\gtrsim 10$ | yes |
| IceTop [60] | 2835 | 10^{15} to 10^{17} | $\gtrsim 0.2$ | $\gtrsim 3$ | no |
| EAS-MSU [61] | 190 | 10^{17} to 10^{18} | $\gtrsim 10$ | $\gtrsim 3$ | no |
| IceTop [62] | 2835 | $\approx 10^{17}$ | $\gtrsim 0.2$ | $\gtrsim 3$ | yes |
| TA [63] | 1400 | $\gtrsim 10^{19}$ | $\gtrsim 0.01$ | $\gtrsim 20$ | yes |

Table 4.1 – Comparison of several studies on the muon excess (data over MC). r is the distance to the shower axis and R_0 is 80 m. The difference between the two lines for IceTop are mainly the distance from the shower axis and primary energy. Please see the text below and section 4.3 for the relevant discussion. [61]

Table 4.1 shows that there seems to exist a muon excess (of data over simulations) in extensive air showers for primaries of higher energy, namely $E \geq 10^{19}$ eV. For primary energies in the range $10^{17} - 10^{18}$ eV HiRes-MIA measured an excess of muons while EAS-MSU did not. The differences between these two experiments is that the former is at an higher altitude (1500 m above sea level), the energy per muon is $E_\mu \geq 0.85$ GeV and it was the outer part of the shower that was studied. The later has $E_\mu \geq 10$ GeV, it is at a lower altitude (190 m above sea level) and studied the inner parts of the extensive air showers. IceTop did not measure an excess of muons in the energy range of $[10^{15}, 10^{17}]$ eV at 600 m from the shower axis [60]. It did however measure an excess of muons at 800 m from the shower axis for primary energies of $\approx 10^2$ PeV [62].

4.2 STUDY OF MUONS WITH THE PIERRE AUGER OBSERVATORY

4.2.1 MEAN NUMBER OF MUONS IN HIGHLY INCLINED EVENTS

The mass composition of high energy cosmic rays is an important parameter to better understand, not only their nature, but also the anisotropies in the arrival directions as well as their acceleration mechanisms and spectrum features.

Since it is not possible to study cosmic rays directly, there needs to be an observable related to the secondary particles from which the type of primary cosmic ray can be derived. There are two such parameters, the X_{\max} and the number of muons. Having two complementary observables reduces the systematic uncertainty in the inference of the mass composition.

As already seen, the number of muons increases almost linearly with the energy of the primary particle and with a small power of the primary mass, A .

$$N_{\mu} = A \left(\frac{E/A}{\epsilon_c} \right)^{\beta} \quad (4.2.1)$$

where ϵ_c is the critical energy at which charged pions decay into muons and $\beta \approx 0.9$ [64]. The N_{μ} has however other dependencies of hadronic interaction properties, as shown by simulations, such as the multiplicity, charge ratio and baryon pair production.

In order to accurately use N_{μ} as a way to infer on the mass of the primary particle, the energy needs to be measured independently.

The logarithmic gain of muons with energy is given by equation 4.2.2.

$$\frac{d \ln N_{\mu}}{d \ln E} = \beta + (1 - \beta) \frac{d \ln A}{d \ln E} \quad (4.2.2)$$

Auger studied [58] the average number of muons in showers with $E > 4 \times 10^{18}$ eV and zenith angles between 62° and 80° , that is, inclined events.

Since the EM component of an air shower is dominant, in order to measure muons, a way to eliminate the EM component has to be used. Given that the γ and e^{\pm} are easily absorbed by the atmosphere and muons are not, the studied data is comprised of either highly inclined events or signals far from the shower core, so that the secondary particles cross a large atmospheric depth.

The muon number is measured by using the relative scale factor N_{19} , which relates the observed muon densities at the ground to the average muon density profile of simulated air showers initiated with a proton with a primary energy of 10^{19} eV. This scale factor is independent of the zenith angle.

The muon density is given by:

$$\rho_{\mu}(\vec{r}) = N_{19} \rho_{\mu,19}(\vec{r}, \theta, \phi) \quad (4.2.3)$$

and so, in order to find the muon number, the direction of the shower (θ, ϕ) needs to be reconstructed. $\rho_{\mu,19}$ is a parametrization of the ground density for QGSJet-II-04 simulation of a proton with an energy of 10^{19} eV.

Figure 4.1 shows an example of $\rho_{\mu,19}$. Its shape and attenuation depends very weakly on energy and mass for showers with $\theta > 60^{\circ}$. The lateral shape of $\rho_{\mu,19}$ is also consistent across different hadronic interaction models and air shower simulation codes.

4.2 Study of muons with the Pierre Auger Observatory

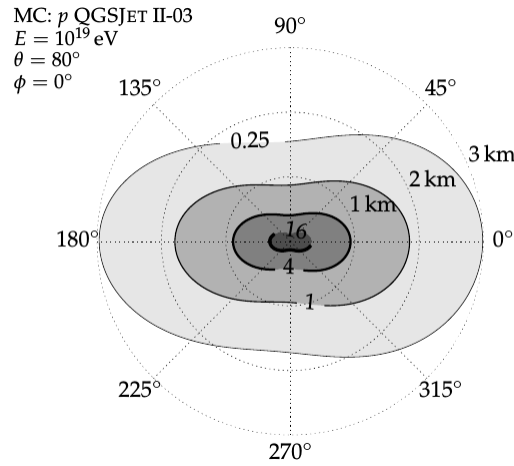


Figure 4.1 – Expected number of muon hits per SD station as predicted by a reference profile $\rho_{\mu,19}$, for $\theta = 80^\circ$ and $\phi = 0^\circ$, in cylindrical coordinates around the shower axis. [58]

The muon content, R_μ of individual air showers with the same energy and direction is not always the same as it suffers from statistical fluctuations in the development of the hadronic cascade and also from possible different primary types from a mixed mass composition. These are intrinsic fluctuations. There are also detector uncertainties. R_μ is given by $R_\mu^{MC} = N_\mu / N_{\mu,19}$ where N_μ is the total number of muons at the ground for each MC event and $N_{\mu,19} = \int dy \int \rho_{\mu,19} dx$. Comparing this ratio to the value of N_{19} obtained from the fit of equation 4.2.3 adjusted to a bias from the model dependence of $\rho_{\mu,19}$ gives deviations smaller than 3%. R_μ^{MC} is thus abbreviated to R_μ .

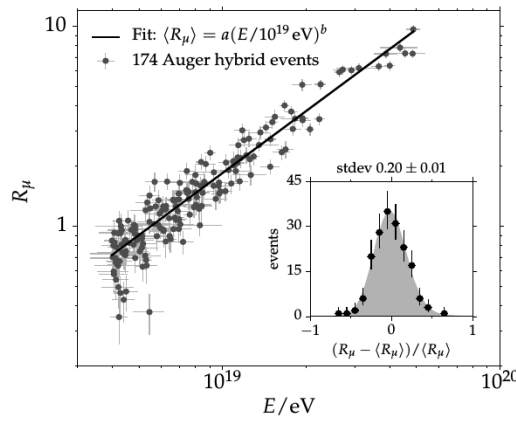


Figure 4.2 – Hybrid events above 4×10^{18} eV and a fit of the power law $\langle R_\mu \rangle = a \langle E / 10^{19} \text{ eV} \rangle^b$. The error bars are statistical detection uncertainties. The inset is an histogram of the residuals around the fitted curve (black dots). [58]

Figure 4.2 shows data points for R_μ as a function of the energy and their respective fit to a power function given by:

$$\langle R_\mu \rangle = a \left(\frac{E}{10^{19} \text{eV}} \right)^b \quad (4.2.4)$$

where a represents the average muon content $\langle R_\mu \rangle (10^{19})$ eV and b the logarithmic gain of muons with energy $\frac{d\langle \ln R_\mu \rangle}{d \ln E} \approx \frac{d \ln N_\mu}{d \ln E}$. The fit parameters are as follows:

$$a = 1.841 \pm 0.029 \pm 0.324(\text{sys.}) \quad (4.2.5)$$

$$b = 1.029 \pm 0.024 \pm 0.030(\text{sys.}) \quad (4.2.6)$$

$$\sigma[R_\mu]/R_\mu = 0.136 \pm 0.015 \pm 0.033(\text{sys.}) \quad (4.2.7)$$

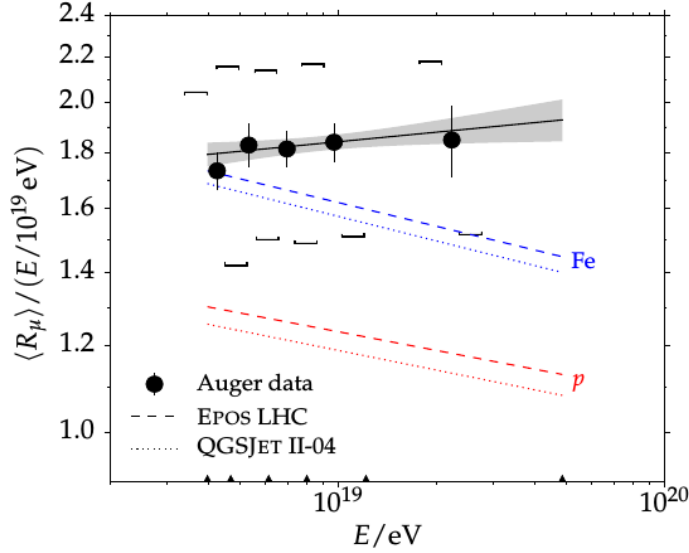


Figure 4.3 – Average muon content per shower energy as a function of the shower energy. The circles are data and the black line represents the fit to equation 4.2.4. Square brackets are the systematic uncertainty of the measurement and the diagonal offsets represent the correlated effect of systematic shifts in the energy scale. The grey band is the statistical uncertainty of the fit. The simulated curves are for $\theta = 67^\circ$ for proton and iron primaries. Black triangles at the bottom show the energy bin edges. Different bins have the same number of events.[58]

Figure 4.3 is the average muon content per shower energy as a function of the shower energy for data and simulations with EPOS-LHC and QGSJet-II-04. The ratio $\langle R_\mu \rangle / (E/10^{19})$ eV emphasizes the effect of the cosmic ray mass, A , on the muon number. The separation of the proton and iron showers, in figure 4.3, shows the power of $\langle R_\mu \rangle$ as a composition estimator. The measured muon number is higher than in pure iron simulations, thus suggesting contributions from heavier elements, which is astrophysically unlikely.

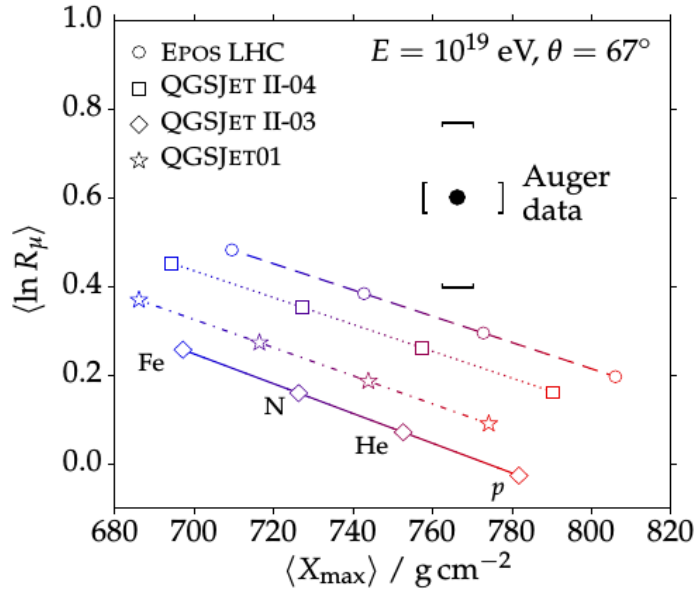


Figure 4.4 – Average logarithmic muon content $\langle \ln R_\mu \rangle$ as a function of the average shower depth $\langle X_{\max} \rangle$ at 10^{19} eV. Model predictions are obtained from showers simulated at $\theta = 67^\circ$. [58]

Figure 4.4 shows the average logarithmic muon content $\langle \ln R_\mu \rangle$ as a function of the average shower depth $\langle X_{\max} \rangle$ at 10^{19} eV. Comparing it to figure 4.3 shows a disagreement in the mass composition as the $\langle X_{\max} \rangle$ information from figure 4.4 points to a composition lighter than iron while figure 4.3 suggests a composition heavier than iron. Data and simulations are also not in agreement as there is a lack of overlap in of the data point with any of the lines representing the simulations by the different hadronic interaction models.

Figures 4.5a and 4.5b summarize and compare the measured data with model predictions. All 4 hadronic interaction models fail to match the data of the mean logarithmic muon content, $\langle R_\mu \rangle$, even though the models updated with LHC data have results slightly closer to the observed. For the models to be consistent with the measurement of $\langle \ln R_\mu \rangle$, the mean muon number in simulations initiated by an energy of around 10^{19} eV would have to be increased by 30% to 80% $^{+17\%}_{-20\%}$ (sys.). If one were to consider the model predictions the true value, than Auger's energy scale would have to be increased by a similar factor.

For the logarithmic gain of muons with energy, $\frac{d\langle \ln R_\mu \rangle}{d \ln E}$, the discrepancy between the measured value and predictions of the different models is smaller. By adding the statistical and systematic uncertainties in quadrature, deviations from pure proton are of 2.2σ and from pure iron of 2.6σ , suggesting a mixed mass composition. The high gain of muons with energy favors a transition from lighter to heavier elements in the considered energy range.

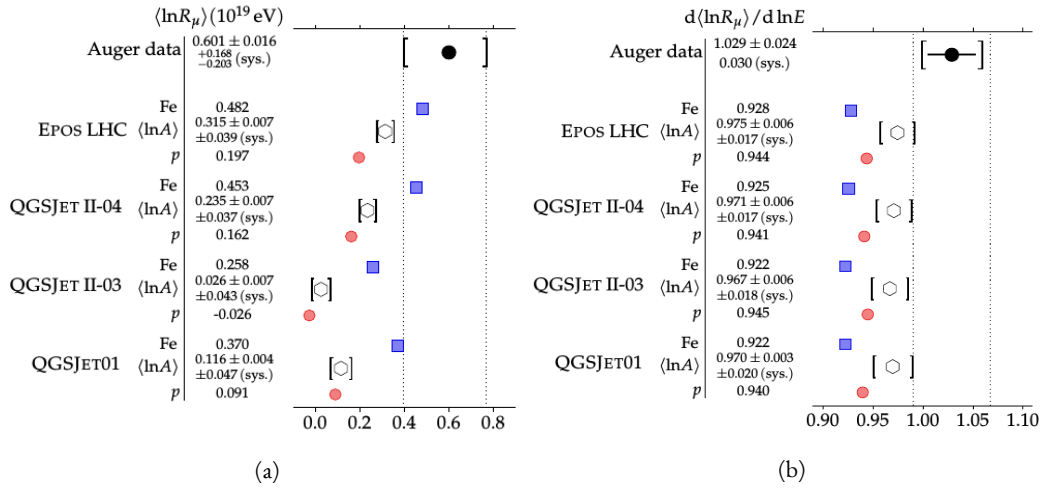


Figure 4.5 – (Left) Comparison of the mean logarithmic muon content $\langle \ln R_\mu \rangle$ at 10^{19} eV obtained from Auger data with model predictions for proton and iron showers simulated at $\theta = 67^\circ$, and for such mixed showers with a mean logarithmic mass that matches the measured $\langle X_{max} \rangle$. The dotted lines represent the interval obtained by adding systematic and statistical uncertainties in quadrature. Brackets indicate systematic uncertainties. (Right) Comparison of the logarithmic gain $d\langle \ln R_\mu \rangle / d \ln E$ between 4×10^{18} eV and 5×10^{19} eV with model predictions, similar as to the graphic on the left.[58]

4.2.2 MUON PRODUCTION DEPTH

Considering that the X_{max} is measured by the FDs, which only have about 15 % duty cycle, it suffers from low statistics. The Muon Production Depth (MPD) can be constructed based on arrival times of the muons on the ground, measured with the SD array, and, knowing that muons decay from pions and kaons and that different primary types have different hadronic properties that will translate into different longitudinal profiles, the MPD distribution is a good observable for the study of the mass composition, as it is sensitive to the primary mass.

Auger recently explored the possibility of using MPD distributions to infer the mass composition of UHECRs and to constrain hadronic interaction models.[22]

Since the Bremsstrahlung and multiple scattering effects are not as important for muons as for the EM component, muons point directly to their production depth. Their production point is given by:

$$z \approx \frac{1}{2} \left(\frac{r^2}{c(t - \langle t_\epsilon \rangle)} - c(t - \langle t_\epsilon \rangle) \right) + \Delta - \langle z_\pi \rangle \quad (4.2.8)$$

The geometric parameters of equation 4.2.8 are defined in figure 4.6. t_g is the geometric delay, a time delay due to a deviation of the muon's trajectories with respect to the direction of the shower axis. $\langle t_\epsilon \rangle$ is a mean kinematic delay caused by the muons not travelling at c (which is one of the assumptions of a first approximation) and by suffering inelastic collisions with air molecules. t_g has been approximated by $t_g \approx t - \langle t_\epsilon \rangle$.

Equation 4.2.8 translates a point in the ground and an arrival time of a muon onto its production point. The production depth X^μ is found by integrating the atmospheric density, ρ :

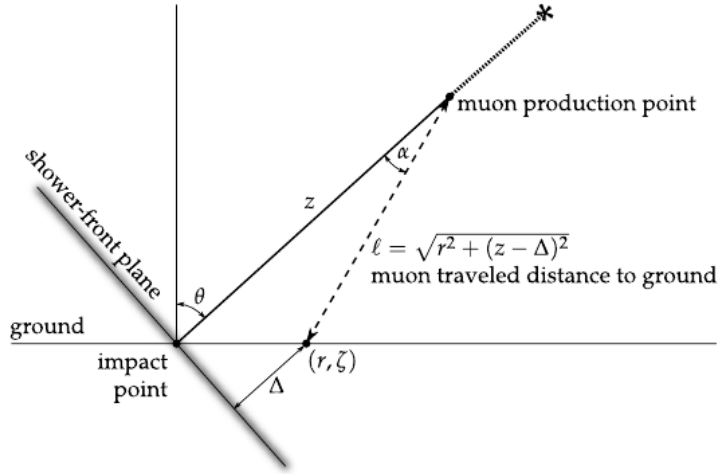
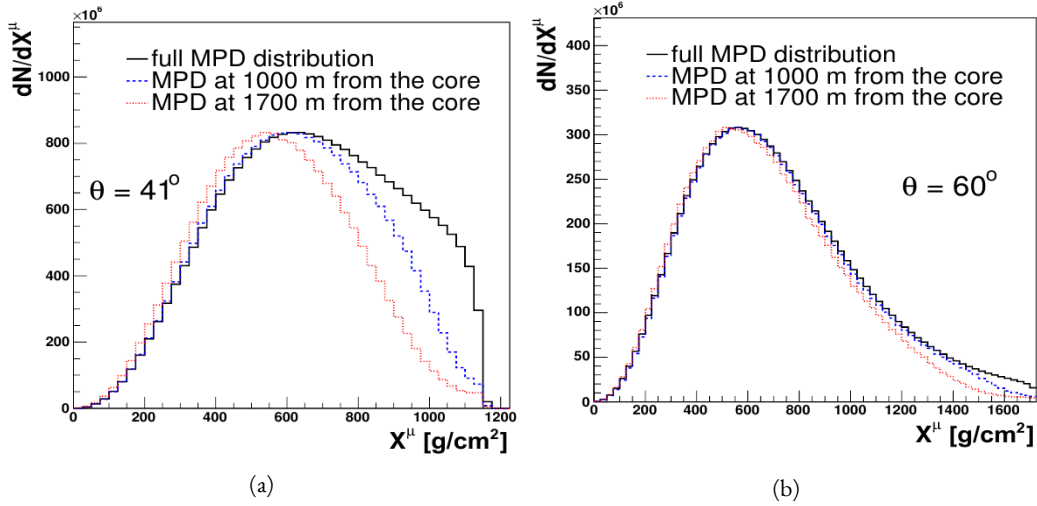


Figure 4.6 – Geometry used to obtain the traveled distance by a muon and its time delay. [22]

$$X^\mu = \int_z^\infty \rho(z') dz' \quad (4.2.9)$$


 Figure 4.7 – MPD distributions produced by an iron shower with an energy of 10^{19} eV with two different zenith angles, 41° (left) and 60° (right) using EPOS-LHC. The histograms are normalized to have the same maximal height. [22]

As can be seen in figure 4.7, the MPD at ground is a function of the zenith angle. For $\theta \approx 41^\circ$ and lower, the shape and the position of the maximum is also a function of the distance from the core, r . At zenith angles of roughly 60° , the differences between MPDs at different distances from the core is small. This is due to large values of z dominating at higher zenith angles and so the dependence of the distance the muon traveled, l , on r is smaller.

For each event, a Gaisser-Hillas function is fitted to the muon longitudinal development profile:

$$\frac{dN}{dX} = \frac{dN_{max}}{dX} \left(\frac{X - X_0}{X_{max}^\mu - X_0} \right)^{\frac{X_{max}^\mu - X_0}{\lambda}} e^{-\frac{X_{max}^\mu - X_0}{\lambda}} \quad (4.2.10)$$

X_{max}^μ is the point in the shower axis where the muon production reaches its maximum. This is the main observable for the studies of mass composition in [22]. The analyzed data has zenith angles in the interval $[55^\circ, 65^\circ]$.

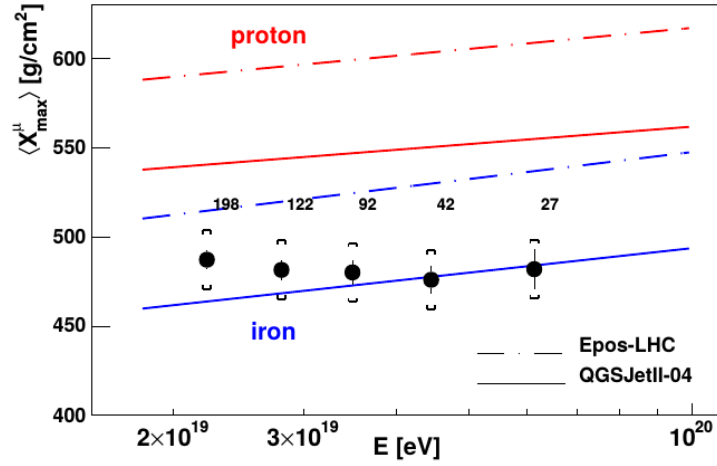


Figure 4.8 – $\langle X_{max}^\mu \rangle$ as a function of energy for data (black circles) and simulations by Epos-LHC and QGSJet-II-04 initiated by a proton (red) and an iron (blue). Brackets represent the systematic uncertainty.[22]

Figure 4.8 shows $\langle X_{max}^\mu \rangle$ as a function of the energy for a total of 481 events. It suggests a change in composition with increasing energy. The measured data is compatible, within errors, with simulations using QGSJet-II-04 initiated by an iron nuclei. The muonic elongation rate, evolution of X_{max}^μ with energy, is similar for both models, differing only in the absolute value of X_{max}^μ .

Since X_{max}^μ and X_{max} are strongly correlated, by a correlation factor of ≥ 0.8 , according to simulations, it is possible to convert both into $\langle \ln A \rangle$. Figure 4.9 shows this conversion using QGSJet-II-04 and EPOS-LHC as reference models¹.

It is seen that for EPOS-LHC, the composition seems to be heavier than iron for higher energies, using X_{max}^μ . X_{max} and X_{max}^μ are clearly incompatible with each other, by at-least 6σ .

For QGSJet-II-04, X_{max}^μ and X_{max} differ by a lesser amount: 1.5σ . Thus, neither model describes the EM and muonic component of air showers in a compatible way.

1. In order to convert X_{max} and X_{max}^μ into $\ln A$, one needs to compare measurements with simulation data, in order to give a mass number to a given observable.

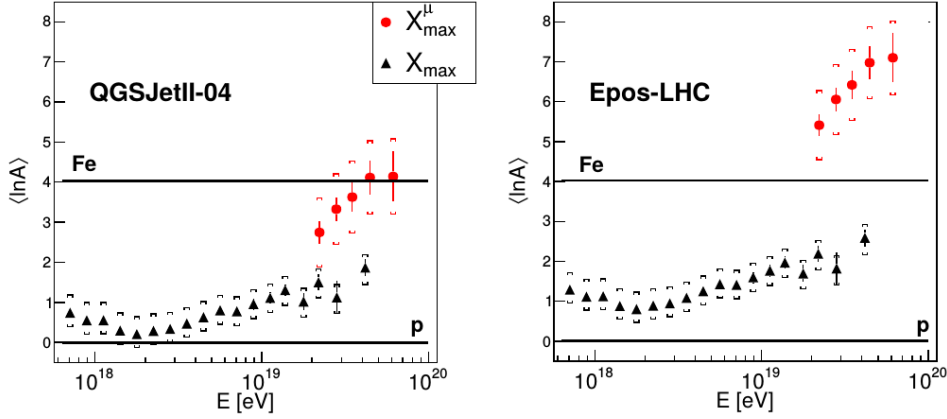


Figure 4.9 – Conversion of $\langle X_{max}^\mu \rangle$ and $\langle X_{max} \rangle$ to $\langle \ln A \rangle$ as a function of energy for two reference hadronic models, QGSJet-II-04 (left) and EPOS-LHC (right). Brackets represent systematic uncertainties.[22]

4.2.3 TESTING HADRONIC INTERACTIONS

In [65], hadronic interaction models were tested in 411 hybrid events with a primary energy of $10^{18.8} - 10^{19.2}$ eV and $\theta < 60^\circ$ whose longitudinal and lateral development were measured, simultaneously, by the Pierre Auger Observatory. The small energy range is chosen so that the mass composition is not changed much while also having enough statistics.

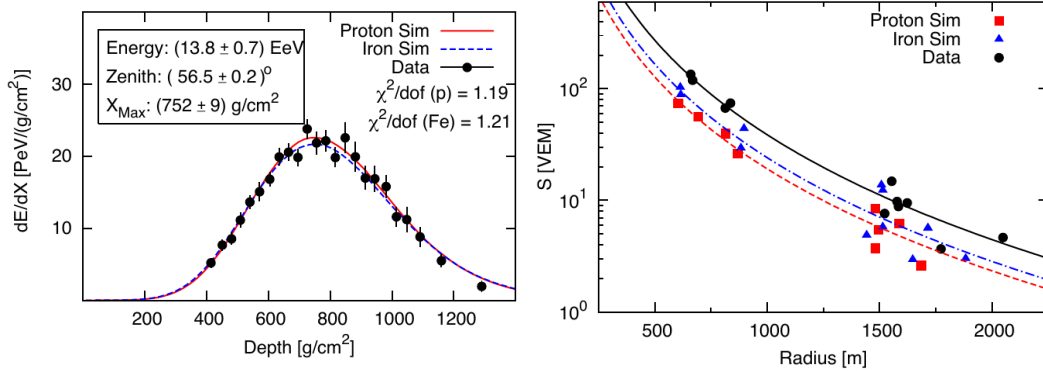


Figure 4.10 – Left: Illustrative measurement of a longitudinal profile with its matching simulated showers, using QGSJet-II-04. Right: Observed and simulated ground signal for the same event. The curves are an LDF fit to the signal.[65]

Figure 4.10 shows that the measured longitudinal profile matches the simulation curves. The observed ground signal is, however, systematically bigger than the simulated signal, as can be seen in the right figure. This disparity between the observed signal and the simulated signal is one of the current problems in the physics of cosmic rays.

This analysis used the $S(1000)$, ground signal at a distance of 1000 m from the core for measured data and a re-scaling of that ground signal for simulated events. For a shower i with an assumed primary mass j , S_{EM} and S_{had} are the electromagnetic and hadronic signal, respectively. The $S(1000)$ is re-scaled by using:

$$S_{resc}(R_E, R_{had})_{i,j} = R_E S_{EM,i,j} + R_{had} R_E^\alpha S_{had,i,j} \quad (4.2.11)$$

where R_E is an energy re-scaling parameter and R_{had} is a re-scaling of the hadronic component of the shower. The first re-scales the total ground signal of the event while the later, R_{had} , only the signal from hadronic origin. R_E^α is due to the hadronic signal increasing slower than linearly with energy. α was found to be ≈ 0.9 by simulations using EPOS and QGSJet-II.

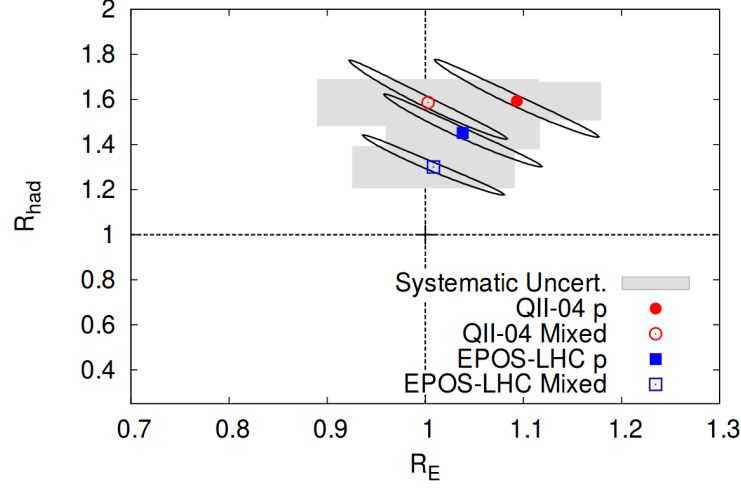


Figure 4.11 – Best fit values of R_E and R_{had} . The ellipses and gray boxes show the 1σ statistical and systematic uncertainties. R_{had} is the scaling of the hadronic component of the extensive air shower and R_E is the scaling of the EM component. [65]

Figure 4.11 shows the values of R_E and R_{had} for EPOS-LHC and QGSJet-II-04 for proton and mixed compositions which were obtained by maximizing a likelihood function which is a function of S_{resc} and S_{1000} from simulations and data, respectively. It shows that there is no need for a re-scaling of the energy but the hadronic signal is, in the studied data, significantly larger than predicted by both EPOS-LHC and QGSJet-II-04. The difference in R_{had} between these two models could be due to some incorrectly modeled features of hadronic collisions or it could be an indication of new physics in hadronic interactions at ultra-high energies. [65]

4.3 STUDY OF MUONS WITH THE ICECUBE/ICE TOP OBSERVATORY

The IceCube is an important observatory to study the discrepancy between the number of muons detected and the number of muons simulated in EAS at the highest energies. This is due to the ability of separating the GeV and TeV muon component in air showers. Figure 4.12 shows a sketch of an air shower developing over the IceCube observatory. The GeV muons are detected by the surface component of IceCube called IceTop while detectors buried in the ice measure only the TeV muons since the lower energy muons were absorbed by the 1.5 km thick ice. The energy threshold for vertical particles is 0.3 TeV.

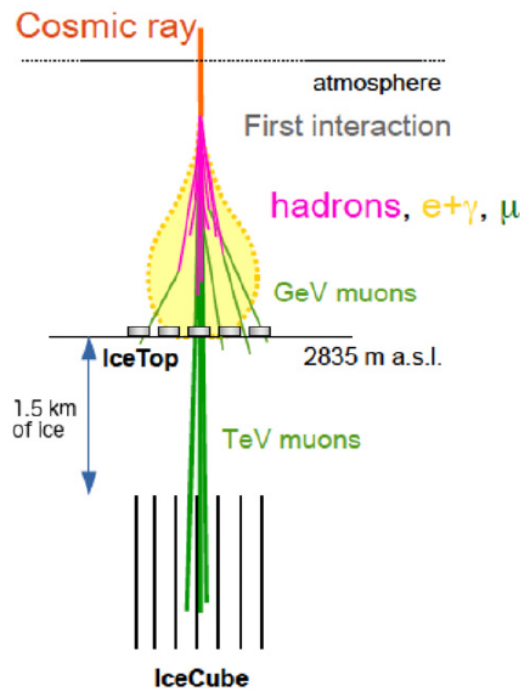


Figure 4.12 – Sketch of an air shower over the IceCube Neutrino Observatory. [62]

By using tanks from the Ictop array far from the shower axis, single muon hits can be separated from hits from other particles. In [62], figure 4.13 was obtained and shows the average lateral muon density profiles for showers in which the particle particle has a zenith angle $\approx 13^\circ$.

Using simulations of proton and iron primaries, figure 4.13 was shown to be slightly biased and, taking into account the average effect for these simulations, figure 4.14 was obtained.

Figure 4.14 shows the muon density for a lateral distance of 600 m and 800 m as a function of the primary energy with expected values using CORSIKA and SIBYLL 1.2 represented by full-lines. At 1 PeV the results are compatible with a light composition and as energy rises the composition seems to grow heavier. Around 10^2 PeV and at 800 m from the shower axis the density of muons is larger than predicted for iron primaries which is not plausible from an astrophysical point of view. This discrepancy between the number of muons measured and simulated is likely due to a deficient description of muons by SIBYLL 2.1 as energy increases. The muon density for

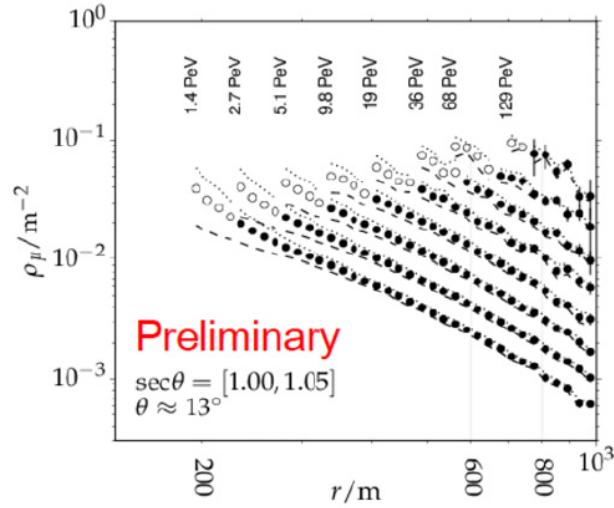


Figure 4.13 – Lateral profiles of muon density as observed in IceTop for near vertical showers (average $\theta \approx 13^\circ$) for several energy bins. The average energy per bin is shown in text. Dotted and dashed lines are estimates based on alternative models used to fit background of non-muon signals. Open dots represent discarded results due to the impact of non-muon background: their systematic uncertainty becomes too large for distances closer to the shower axis. These profiles are results obtained directly from fits of signal distributions without applying any composition-dependent correction. [62]

600 m is between the expected simulated value for iron and proton primaries although, for this distance, the range of primary energy is smaller. [62]

Another Icecube result, [60], measured the muon content of air showers. Figure 4.15 is a distribution of lateral distance and tank signal for air showers with energy $4 \text{ PeV} < E < 5 \text{ PeV}$ and a zenith angle $28^\circ < \theta < 32^\circ$. It can be seen that at large distances there are two separable and different populations: one follows the main distribution and the other, with signals around 1 VEM, is mostly from tanks hit by one or more muons. Figure 4.16 shows these two populations more clearly using two cuts on the lateral distance, at 257 m and 646 m.

The mean number of muons is obtained by fitting the charge distributions at a fixed energy, zenith angle and lateral distance, as shown in figure 4.16. The fit uses 3 different models, each model representing a different signal's population: signals with muons, signals without muons and signals that, while not produced by the air shower, have a time coincidence with it². Dividing the mean number of muons with the cross-sectional area of the tanks gives the muon density at a particular location, which is plotted in figure 4.17. This figure shows that the muon density at 600 m from the shower axis for almost vertical cosmic ray events is, for the range of energies considered, between the simulated density for proton and iron primaries. This result is compatible with the one from figure 4.14 at 600 m from the shower axis.

2. For a description of the models, please see [60]

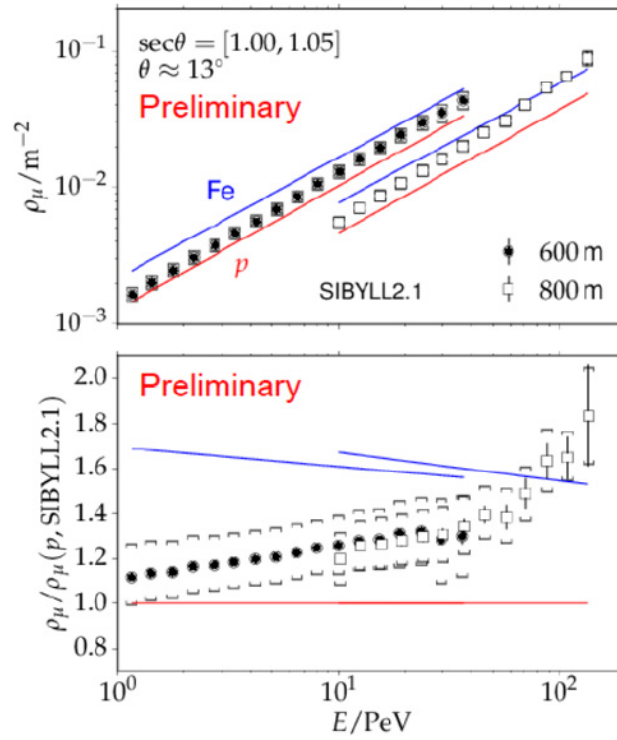


Figure 4.14 – Top: Muon density at 600 m and 800 m as a function of primary energy for near vertical showers. Lines show the expected values for proton (red) and iron (blue) simulated with CORSIKA and SIBYLL 2.1. Bottom: Same as above but with densities normalized to the expected density for proton showers. Brackets represent systematic uncertainties and the muon densities were corrected for a small composition-dependent bias. [62]

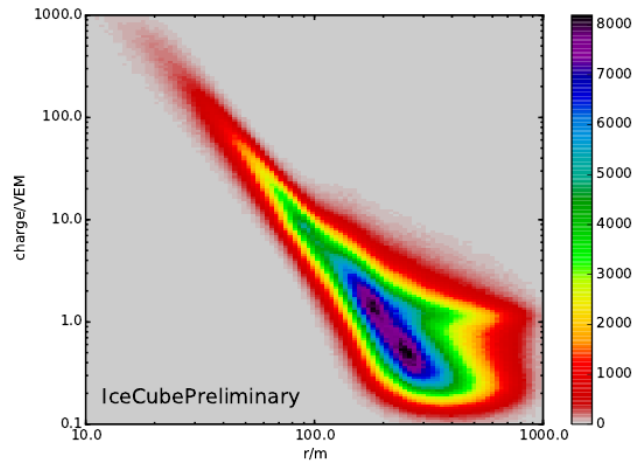


Figure 4.15 – Signal distribution as a function of lateral distance for showers with an energy $4\text{PeV} < E < 5\text{PeV}$ and a zenith angle $28^\circ < \theta < 32^\circ$. [60]

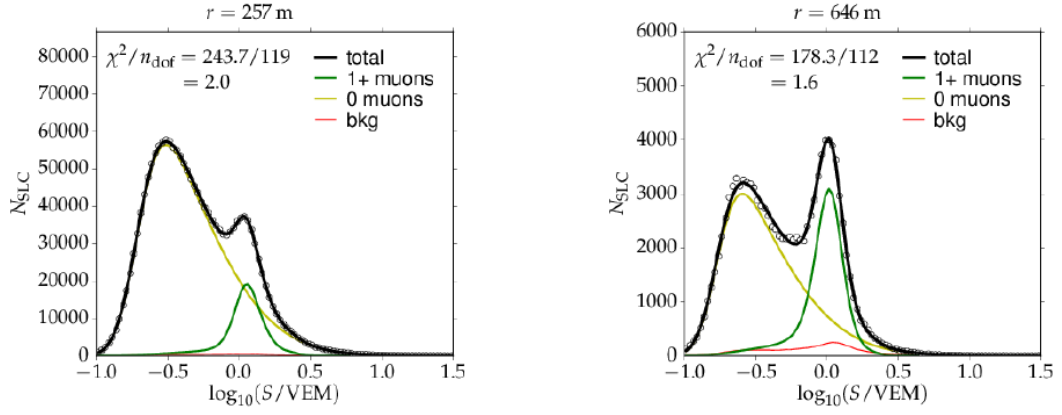


Figure 4.16 – Distribution of signals at two fixed lateral distances, 257 m and 646 m. The energy and zenith angle are the same as figure 4.15. The yellow line corresponds to EM particles and the red line to accidental coincidences. The green line represents 1 or more muons and its model is explained in [60].

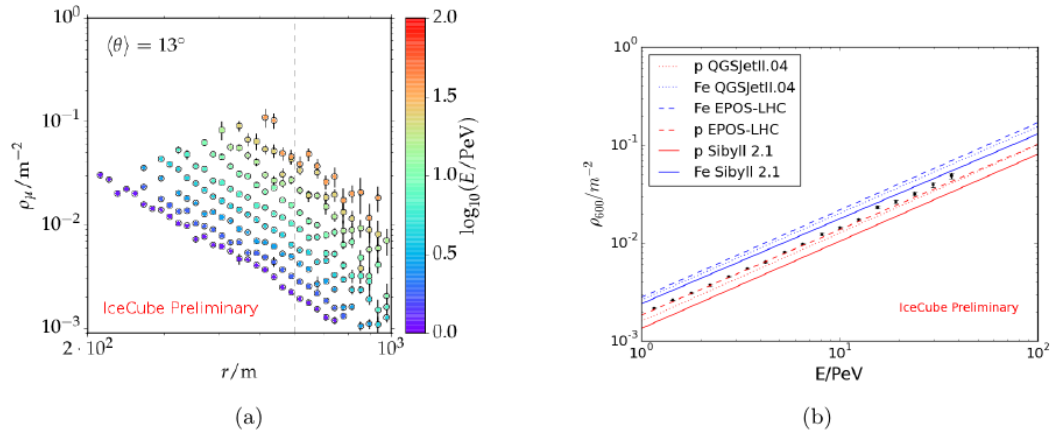


Figure 4.17 – (a): Muon density as a function of lateral distances for showers with a zenith angle $\approx 13^\circ$. (b): Interpolated value for 600 m from the shower axis and comparison to the expected simulated value using QGSJet-II-04, EPOS-LHC and SIBYLL 2.1 for two different primary compositions, proton and iron. [60]

4.4 STUDY OF MUONS WITH THE TELESCOPE ARRAY

The Telescope Array³ (TA) has also studied the muon puzzle. By using data obtained with the SD array during 11 May 2008 and 11 May 2015 (7 years) with an energy ranging from $10^{18.8}$ eV and $10^{19.22}$ eV, TA compared the detected number of muons with the number of muons expected from simulations. According to data taken by TA's FDs, in the considered energy range the X_{\max} is compatible with a light composition, hence the simulations are done for proton primaries unless stated otherwise. The simulated energies range from $10^{16.55}$ eV to $10^{20.55}$ eV and the zenith angle is isotropic between 0° and 60° . For the experimental data, the energy scale is corrected with the FD. This is so a difference in the number of muons is not due to a different energy scale.

Figure 4.18 shows the lateral distribution of the signal for data and for proton simulations as well as the ratio of the data to the MC. The signal size for that is consistently larger than for simulations. It can also be seen that the distribution for the data decreases slower than for MC. For $R > 4000$, the two distributions are closer again due to the atmospheric muons dominating the signals from the SD. The comparison between data and simulations for other hadronic interaction models are done in figure 4.19 and in figure 4.20 the ratio of the signal size of data to the MC for two primary types, proton and iron. Figure 4.20 shows that the average signal of the data is different than the MC, for iron, considering errors, for $R \gtrsim 2500$ m. Table 4.2 summarizes the results for each bin of distance for the 2 primaries using QGSJet-II-03.

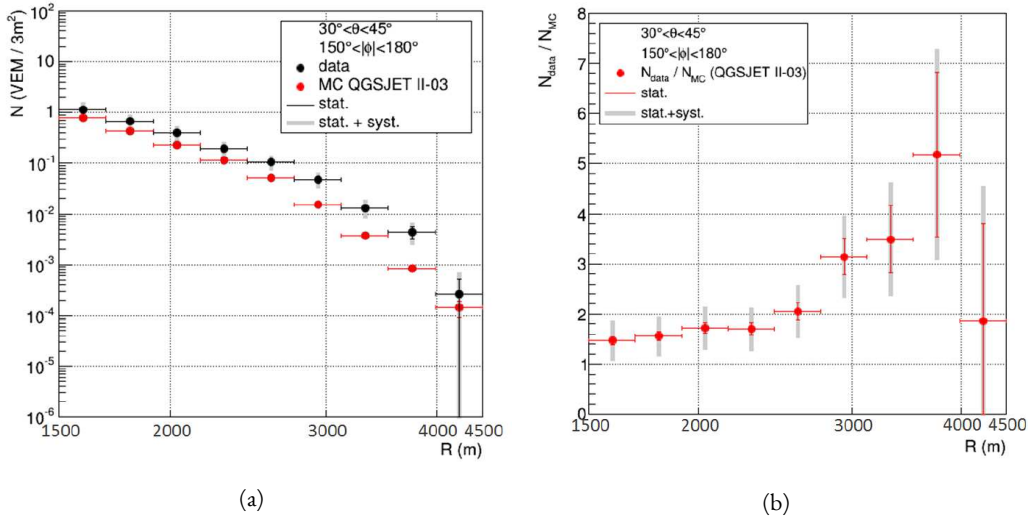


Figure 4.18 – Lateral distributions for data and simulations for $30^\circ < \theta < 45^\circ$ and $150^\circ < \phi < 180^\circ$ as a function of distance to the shower axis. The thin vertical error bars are statistical errors while the grey thick error bars represent quadratic sums of statistical and systematic errors. (a) Average signal assuming a Poisson distribution and (b) average ratio of data over simulations. The simulations are for a proton primary. [63]

In the condition of muon purity of $\approx 65\%$ ($30^\circ < \theta < 45^\circ$, $150^\circ < \phi < 180^\circ$ and $2000 \text{ m} < R < 4000 \text{ m}$) for primaries of energy $10^{18.8}$ eV and $10^{19.2}$ eV, the ratio of the signal

3. The Telescope Array is an hybrid observatory with a surface array of 507 scintillation counters covering 700 km^2 and 3 fluorescence detector stations. It is located in Utah, USA.

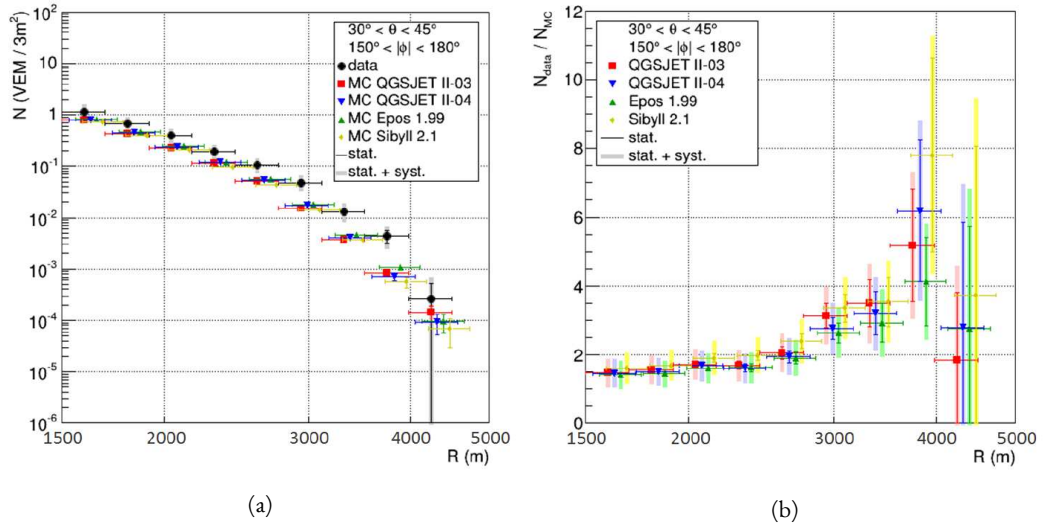


Figure 4.19 – Same as figure 4.18 but with additional simulations using different hadronic interaction models. (a) In order for the error bars to be easily seen, the plot for the 3 last hadronic interaction models are shifted to the right. (b) Average ratio of data over simulations.[63]

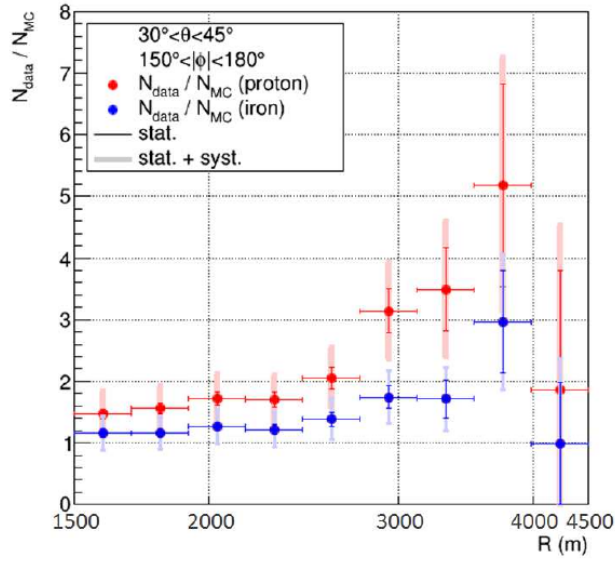


Figure 4.20 – Ratio of signal size of data over simulations for proton and iron primaries using QGSJet-II-03. The vertical thin error bars are statistical errors while the thick shaded bars represent quadratic sums of statistical and systematic errors.[63]

size of data to the simulations using QGSJet-II-03 is $1.72 \pm 0.10 \pm 0.37$ at $1910 \text{ m} < R < 2160 \text{ m}$ and $3.14 \pm 0.36 \pm 0.69$ at $2760 \text{ m} < R < 3120 \text{ m}$. Using instead the model QGSJet-II-04, the ratios are smaller, namely, $1.67 \pm 0.10 \pm 0.36$ and $2.75 \pm 0.32 \pm 0.60$ for the same bins of distance.

| R [m] | Ratio $\pm \sigma_{\text{stat.}} \pm \sigma_{\text{syst.}}$ | |
|--------------|---|---------------------------------|
| | Proton | Iron |
| [1500, 1695] | $1.47^{+0.09}_{-0.08} \pm 0.35$ | $1.72^{+0.07}_{-0.06} \pm 0.28$ |
| [1695, 2160] | $1.56^{+0.09}_{-0.08} \pm 0.35$ | $1.16 \pm 0.06 \pm 0.26$ |
| [1915, 2160] | $1.72 \pm 0.10 \pm 0.37$ | $1.26 \pm 0.07 \pm 0.27$ |
| [2160, 2445] | $1.69 \pm 0.12 \pm 0.37$ | $1.22 \pm 0.08 \pm 0.27$ |
| [2445, 2760] | $2.05 \pm 0.18 \pm 0.46$ | $1.38 \pm 0.11 \pm 0.31$ |
| [2760, 3120] | $3.14 \pm 0.36 \pm 0.69$ | $1.74 \pm 0.19 \pm 0.38$ |
| [3120, 3525] | $3.49 \pm 0.68 \pm 0.86$ | $1.71 \pm 0.30 \pm 0.42$ |
| [3525, 4180] | $5.18 \pm 1.64 \pm 1.27$ | $2.96 \pm 0.83 \pm 0.72$ |
| [4180, 4500] | $1.85 \pm 1.95 \pm 1.81$ | $0.99 \pm 0.99 \pm 0.99$ |

Table 4.2 – Ratio of the observed signal size by the SD to the expected value using simulations with QGSJet-II-03 as a function of the distance to the shower axis, R. Statistical and systematic errors are also shown. [63]

Figure 4.21 shows the relationship between the purity of muons expected from simulations and the ratio of signal size of data over MC. It can be seen that for a higher purity of muons, the difference in signal size between the two types of data is larger which suggests that the discrepancy, or muon puzzle, is because of an excess of muons in the data.

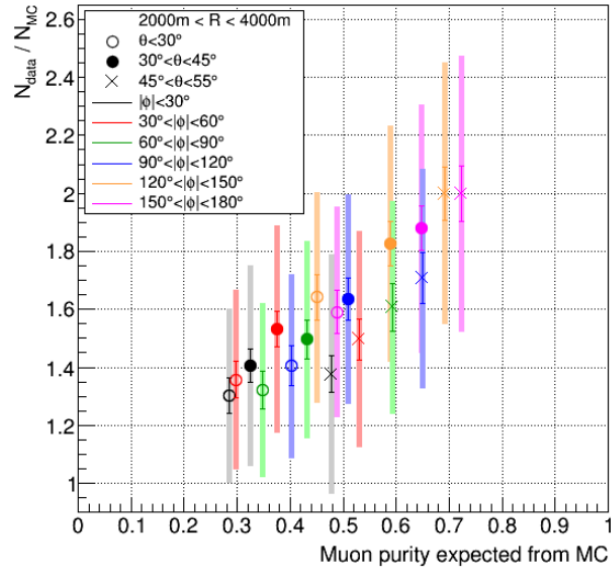


Figure 4.21 – Ratio of the signal size of data over simulations as a function of muon purity for several conditions of the zenith and azimuth angle. The hadronic interaction model used is QGSJet-II-03. The vertical thin error bars are statistical errors while the thick shaded bars represent quadratic sums of statistical and systematic errors. [63]

This TA result is consistent with the results from the Pierre Auger Observatory.

4.5 STUDY OF MUONS WITH THE EAS-MSU OBSERVATORY

The EAS-MSU observatory has also studied the muon puzzle, in [61]. The EAS-MSU array is located in Moscow at an altitude of 190 m above sea level. The array occupies an area of 0.5 km² with 76 stations to detect charged particles, each consisting of multiple Geiger-Mueller counters. The center of the array is where the main muon detector is located and consists of 1104 Geiger-Mueller counters occupying an area of 36.4 m². The counters are at a depth of 40 meters of water equivalent underground. [61]

This experiment focused on cosmic rays with $\theta < 30^\circ$, a primary energy of $E \gtrsim 10^{17}$ eV and a distance of less than 240 m from the shower axis to the center of the array. The data comprised 1204 days and consists of 809 cosmic ray events.

The primary composition for use in the simulations were determined by data taken by EAS-MSU itself. It was found that a mixture of 43% protons and 57% iron described best the data obtained with the surface array. This is the mass composition mixture used for event generation in the simulations.

To quantify a possible muon excess a parameter k was introduced in order to scale the muon number in simulated showers. $k = 1$ corresponds to the muon number predicted by simulations using QGSJet-II-04. This k parameter was implemented only for the muon density measured by the underground detectors, surface-detector observables remain unchanged. A binned chi-square method was used to test for a muon excess of data over simulations.

Figure 4.22 shows the distributions in ρ_μ at 100 m from the shower axis for data and simulations where ρ_μ was obtained by fitting the data/simulations to equation 4.5.1.

$$\rho_\mu(r) = N_\mu \left(\frac{r}{R_0} \right)^{-\alpha_\mu} \exp(-r/R_0) \quad (4.5.1)$$

with $R_0 = 0.80$ m and $\alpha_\mu = 0.64 \pm 0.08$ for the best fit mixture and $\alpha_\mu = 0.88 \pm 0.18$ for the data.

It can be seen in figure 4.22 that the distributions are in good agreement. The mixture that best describes the $\rho_\mu(100)$ distribution is $(54 \pm 6)\%$ iron. Figure 4.23 shows how a change of the k coefficient affects the agreement between data and simulations for $\rho_\mu(100)$. It plots χ^2/dof as a function of k and it can be seen that, for the blue line, $k = 0.92 \pm 0.06$. Thus, the muon excess is not observed and $k > 1$ is excluded by the data at the 92% confidence level. This result is true for QGSJet-II-04. Other hadronic interaction models, namely EPOS-LHC, SIBYLL 2.1 and QGSJet-01, were also tested and in all cases the muon excess was not seen.

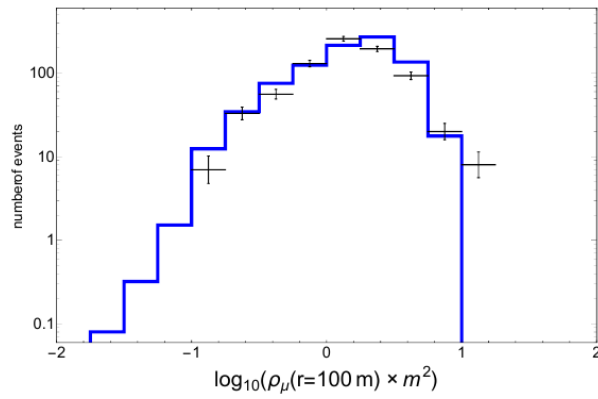


Figure 4.22 – Distribution of $\rho_\mu(100)$. Points with error bars are data and the blue histogram are MC simulations using QGSJet-II-04 based on a primary composition inferred from surface-detector data (43% protons and 57% iron).[61]

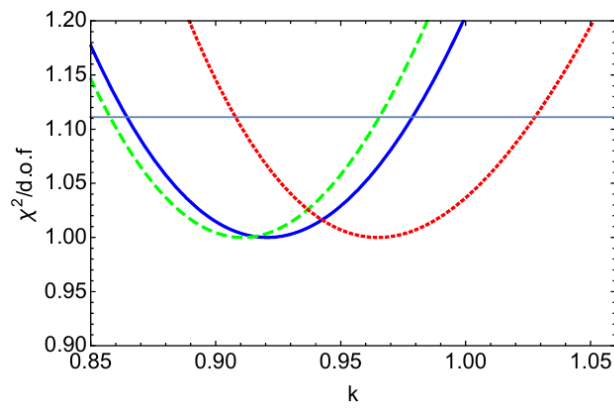


Figure 4.23 – χ^2 per degree of freedom for the muon scaler coefficient, k . Blue line assumes the EAS-MSU surface-detector composition, the green dashed line assumes the KASCADE-Grande composition and the red dotted line the Tunka-133 composition. The horizontal line represents 68% confidence level.[61]

5 TOWARDS AN MLDF AT TdF

The objective of this thesis is to find a mean muon LDF in 10^{17} eV air showers. For practical reasons, the work will be done using only one MARTA station. There is only one MARTA station setup in Auger's SD array and in the time period of this work it is not viable to increase the number of WCDs instrumented with RPCs. The MARTA station consists of two RPCs below the tank, one on top of the other. In this section only one RPC will be considered.

The measurement of this muon LDF has one main requirement: enough statistics for a successful reconstruction of a muon LDF at TdF using muons detected by only one station. In order to do this, an energy cut is done. The energy range studied in this work is $[10^{17}, 10^{17.5}]$ eV. In this energy range, the flux of cosmic rays is sufficiently large and Auger's trigger system has a high probability of detecting and saving events, thus making them useful data. Since the flux decreases as roughly $E^{-3.29}$ in this energy range, decreasing the overall energy increases the flux. A high cosmic ray flux guarantees that there are enough events whose core is near the TdF station so that there is a large number of muons detected. At this energy range, there are, if any, minimal changes in the mass composition which reduces final uncertainties. Another parameter that can be changed to increase the feasibility of this measurement is the detection time. By increasing the acquisition time we are increasing the number of events detected and consequently the number of muons. Changing the active area of the RPC, by increasing the number of pads, is also something that can be considered. The viability of making an actual reconstruction of a muon LDF using real data obtained by two RPCs below a WCD needs first to be studied. This can be done by using Monte-Carlo simulations.

Toy-MC simulations have obvious drawbacks when compared to full Monte-Carlo simulations, done with, for example, CORSIKA. The Toy-MC is based on the Heitler model, which is a simplified version of the interaction and collision of particles in atmospheric cascades, and several assumptions were made. The conclusions are, however, representative of what is to be expected when acquiring real data and the advantages of using a self-made Toy-MC are obvious: it is fast, light on resources and easily tuned.

This section will provide answers to the aforementioned idea by analyzing results obtained by a self-made Toy-Monte-Carlo algorithm fine tuned with full CORSIKA simulations in order to reduce uncertainties and guarantee an accurate analysis.

5.1 ALGORITHM

The algorithm for the Toy-MC can be succinctly explained. First, a core position for the event is generated randomly in an area equal to the one of the Infill array. An azimuth and a zenith angle are generated, the first following a random distribution between 0 and 360° and the second following $\sin \theta$, for $0 \leq \theta \leq 90^\circ$. The distance to the shower axis is found using the

previously generated core position (x, y) . The cosmic ray is either a proton or an iron nuclei, with 50/50 probability, and an energy that follows a distribution of approximately $E^{-3.29}$ and $10^{17} \leq E \leq 10^{17.5}$ eV.

Given the zenith angle, the type of primary cosmic ray and its energy, a lateral trigger probability function (LTP) will decide if the event triggers the T4 condition, hence if it is saved. Non saved events are discarded and do not affect the final LDF reconstruction. The average number of muons is found using a parametrized LDF, the core distance calculated previously and the projected area of the RPC. The number of muons detected at the RPC is then calculated using a Poisson distribution centered around the average number of muons. A more detailed explanation of the algorithm is in section 5.3.

The next section will describe the parametrization of a muon LDF which will serve as an input function in the Toy-MC algorithm.

5.2 PARAMETRIZATION OF A MUONIC LDF

In order to compute the number of muons, detected at the TdF station, one has to have an LDF parametrized in order to serve as an input function that translates distance from the shower axis to the detector to number of particles. Knowing that the Toy-MC is a general algorithm used for different primary types energies and angles, it is necessary to find a parametrization for an MLDF in energy, zenith angle and mass composition.

This parametrization of a muonic LDF was done using CORSIKA data created in the framework of the AugerPrime upgrade studies. There are 4 sets of data that can be seen in table 5.1. This analysis was done using the Offline software framework of the Pierre Auger Observatory [66].

| Primary Particle | Primary Energy [eV] | Primary Zenith angle [°] |
|------------------|---------------------|--------------------------|
| Proton | 10^{17} | 38 |
| Proton | $10^{17.5}$ | 38 |
| Iron | 10^{17} | 40 |
| Iron | $10^{17.5}$ | 40 |

Table 5.1 – Data sets of CORSIKA used to find a parametrization of a muonic lateral distribution function. The azimuth angle of the primary particle was random in -180° to 180° and the observation level was 1400 m (Auger’s altitude) for all sets. There are 100 events for each set. All simulations were done using QGSJet-II-04.

For each data set, the following was done:

1. Search all ground particles;
2. Verify if it is a muon or an anti-muon;
3. Calculate the core distance of each muon/anti-muon;
4. Divide the range of distance in bins;
5. Calculate the area of each distance ring;
6. Calculate the density of muons per ring-distance bin;

7. Find the average density of muons by dividing the total number of muons per distance bin by the total number of events for a given data set;
8. Plot the average density of muons as a function of the center of the ring-distance bin;
9. Do an iterative fit of the plotted function;

5.2.1 FIT TO THE CORSIKA SIMULATIONS

The plotted functions of density of muons at ground as a function of their core distance were fitted using a KASCADE-Grande¹ like MLDF, given by equation 5.2.1, where the values of α , γ and r_0 are 0.75, 3 and 320 m, respectively [68]. The free parameters are β and N_μ and the fit used a chi-square method. The fit was iterative, first fitting N_μ and then β , several times while both the conditions $|\beta_{current} - \beta_{prior}| \geq 0.0001$ and $|N_{\mu_{current}} - N_{\mu_{prior}}| \geq 0.0001$ were true. *prior* refers to the value before the *current* iterative run. The fit was initiated with $N_\mu = 12$ and $\beta = 2.44 \pm 0.38$ as that were the approximate results for a muon LDF found in [68] for a vertical proton of $10^{17.75}$ eV for muons at ground level. The fit starts at a distance of 110 m as the average χ^2 across all data sets was a minimum for that distance.

$$\rho_\mu(r) = N_\mu \left(\frac{r}{r_0}\right)^{-\alpha} \left(1 + \frac{r}{r_0}\right)^{-\beta} \left(1 + \left(\frac{r}{10r_0}\right)^2\right)^{-\gamma} \quad (5.2.1)$$

Figures 5.1, 5.2, 5.3 and 5.4 show the obtained muon LDFs for each data set. The fit parameters, β and N_μ are in table 5.2.

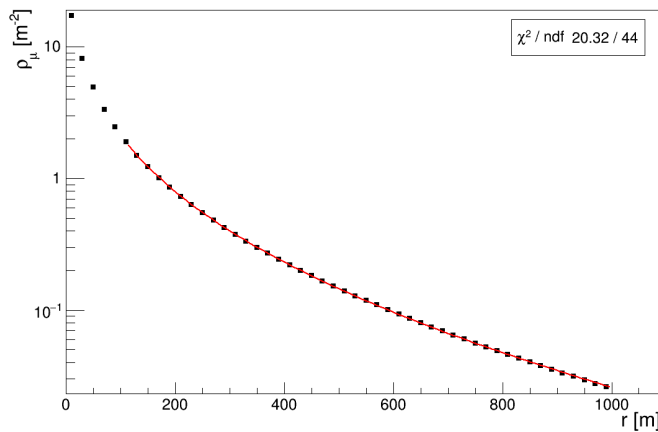


Figure 5.1 – Fit of CORSIKA data set for a proton primary with energy 10^{17} eV. The fit was done using an KASCADE-Grande like function given by equation 5.2.1. The fit parameters can be seen in table 5.2.

1. KASCADE-Grande is an extension of the original Kascade experiment. It was designed to study extensive air showers generated by primary cosmic rays in an energy range of 10^{14} to 10^{18} eV. It is located in Karlsruhe Institut für Technologie, Germany, and consists of an array of 37 scintillation detectors at an average spacing of 137 m [67]

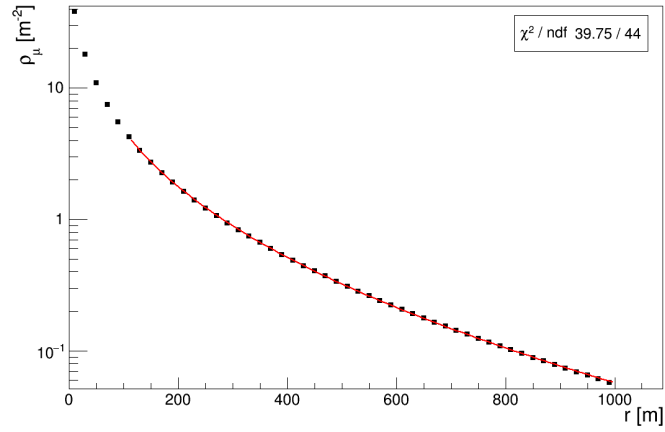


Figure 5.2 – Fit of CORSIKA data set for a proton primary with energy $10^{17.5}$ eV. The fit was done using an KASCADE-Grande like function given by equation 5.2.1. The fit parameters can be seen in table 5.2.

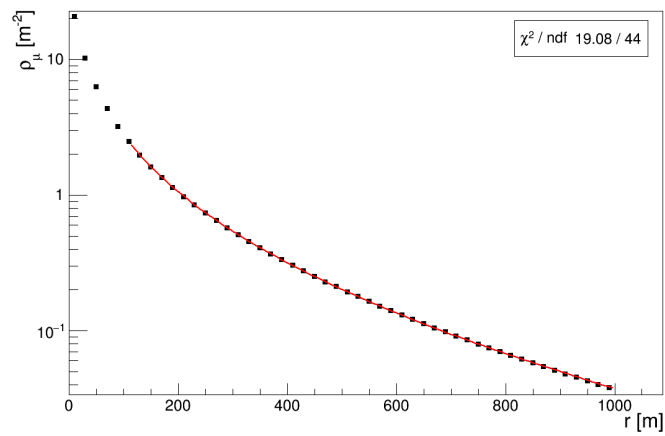


Figure 5.3 – Fit of CORSIKA data set for an iron primary with energy 10^{17} eV. The fit was done using an KASCADE-Grande like function given by equation 5.2.1. The fit parameters can be seen in table 5.2.

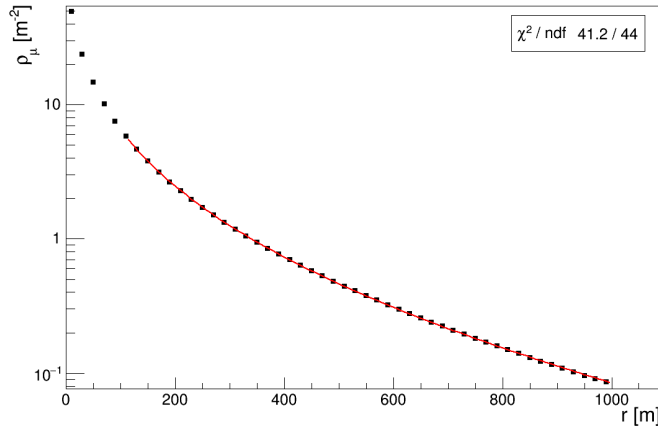


Figure 5.4 – Fit of CORSIKA data set for an iron primary with energy $10^{17.5}$ eV. The fit was done using an KASCADE-Grande like function given by equation 5.2.1. The fit parameters can be seen in table 5.2.

The uncertainty of each point (which, despite not being visible, is there) was calculated bin by bin using equation 5.2.2 where N_μ is the total number of particles per distance-bin, N is the total number of events for a given set (100 in this case) and A is the area of the ring-distance-bin.

$$\delta\rho_\mu = \sqrt{\frac{N_\mu}{N}} \frac{1}{A} \quad (5.2.2)$$

| Parameter | proton, e17 | proton, e17.5 | Iron, 17 | Iron, 17.5 |
|------------------------|-------------------|-------------------|-------------------|-------------------|
| β | 2.096 ± 0.002 | 2.107 ± 0.001 | 2.007 ± 0.002 | 2.044 ± 0.001 |
| $N_\mu [m^{-2}]$ | 1.563 ± 0.002 | 3.509 ± 0.003 | 1.993 ± 0.003 | 4.740 ± 0.004 |
| N. of iterative cycles | 41 | 46 | 45 | 49 |

Table 5.2 – Fit values of the free parameters of the muon LDF function, β and N_μ , and respective uncertainties for each CORSIKA data-set. The number of iterative cycles is the number until convergence was achieved.

Table 5.2 shows the parameters of the fit to the CORSIKA data. While β is approximately constant with a changing primary type and energy it is slightly bigger for proton. N_μ increases both with energy and with mass being a maximum for the data set of an iron primary with $10^{17.5}$ eV. The difference in N_μ is larger when changing from a primary with 10^{17} eV to $10^{17.5}$ eV, with fixed mass, than when changing the primary type from proton to iron, with fixed energy, that is, N_μ changes more with energy than with mass for the ranges considered here. Considering the relation for the number of muons from the Heitler model, equation 4.2.1, this is expected due to the number of muons increasing with the energy with a bigger power than with primary mass.

5.2.2 PARAMETRIZATION OF $\beta(E)$ AND $N_\mu(E)$

A parametrization is now possible with the values of β and N_μ for the two energies, 10^{17} eV and $10^{17.5}$ eV. According to equation 4.2.1, N_μ is approximately linear with energy since it grows as a power of 0.9 over a small range of energy. The changes in β are small enough over the energy range $[10^{17}, 10^{17.5}]$ eV and as such a linear regression is a good approximation. If one were to consider larger energy ranges, a deeper understanding of the behaviour of β with energy would be needed.

Figure 5.5 is a linear fit of N_μ and β for the two considered energies and for a proton primary with a zenith angle of 40° . Changes of the number of muons given by the MLDF to a changing primary type will be parametrized according to the Heitler Model, as seen in section 2.7. The parametrization of β and N_μ as a function of the energy of the primary particle are given by equations 5.2.3 and 5.2.4, respectively.

$$\beta(E) = 2.091 + 5.087 \times 10^{-20} E \quad (5.2.3)$$

$$N_\mu(E)[m^{-2}] = 0.663 + 9 \times 10^{-18} E \quad (5.2.4)$$

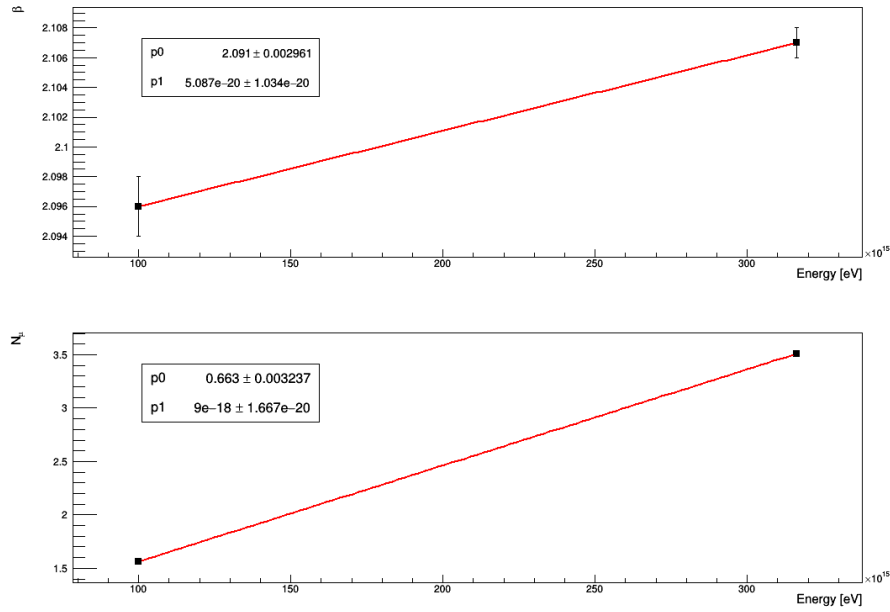


Figure 5.5 – Parametrization of β and N_μ as a function of the primary energy, 10^{17} and $10^{17.5}$ eV. All data points are for a proton primary and a zenith angle of 40° .

It is now possible to generalize the values of β and N_μ , parameters of a muon LDF seen in equation 5.2.1, to the range of energy $10^{17} \leq E \leq 10^{17.5}$ eV.

5.2.3 COMPARISON OF A PARAMETRIZED LDF WITH FULL SIMULATIONS

Since the Toy-MC will use a muon LDF as an input function in order to translate distance into number of particles in the TdF detector, it is important to make sure that the input LDF accurately describes full-simulations.

Equation 5.2.5 represents the final muon LDF parametrization. $A^{1-\beta_H}$ is an Heitler model correction to the mass of the primary particle, as explained in section 2.7, and β_H is 0.90 ± 0.3 [64]. The term $\frac{\cos \theta}{\cos 40^\circ}$ represents an absorption of muons in the atmosphere and from the fact that $N_\mu(E)$ was parametrized using data for $\theta = 40^\circ$.

Figures 5.6, 5.7, 5.8 and 5.9 show that the LDF parametrization is a good fit to the CORSIKA data sets shown in table 5.1.

$$\rho(r) = A^{1-\beta_H} \frac{\cos \theta}{\cos 40^\circ} N_\mu(E) \left(\frac{r}{320}\right)^{-0.75} \left(1 + \frac{r}{320}\right)^{-\beta(E)} \left(1 + \left(\frac{r}{10 \times 320}\right)^2\right)^{-3} \quad (5.2.5)$$

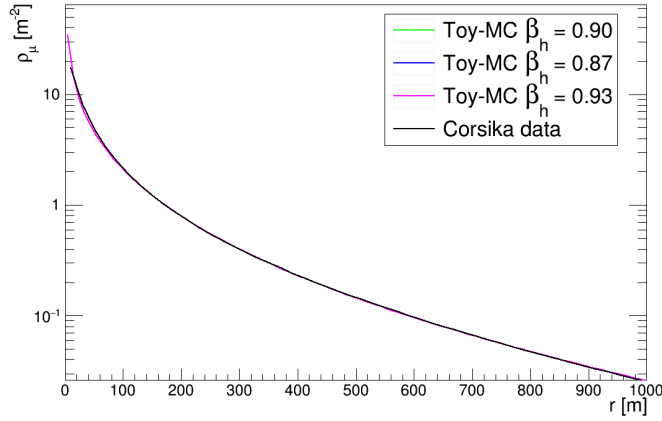


Figure 5.6 – Parametrized LDF given by equation 5.2.5 are in green, blue and purple, and full CORSIKA simulations is in black. Green is with $\beta_H = 0.90$, blue with $\beta_H = 0.87$ and purple $\beta_H = 0.93$. CORSIKA simulations for a proton primary with energy 10^{17} eV and a zenith angle of 40° .

| $\rho_\mu(450)$ [m^{-2}] | p,17,40 | p,17.5,40 | fe,17,38 | fe,17.5,38 |
|-------------------------------------|----------|-----------|----------|------------|
| CORSIKA fit | 0.181138 | 0.402806 | 0.249819 | 0.575187 |
| $\beta_h = 0.87$ | 0.181165 | 0.40282 | 0.314498 | 0.699284 |
| $\beta_h = 0.9$ | 0.181165 | 0.40282 | 0.278723 | 0.619738 |
| $\beta_h = 0.93$ | 0.181165 | 0.40282 | 0.247017 | 0.54924 |
| %diff(%) | 0.015 | 0.004 | 11.570 | 7.745 |

Table 5.3 – Values for $\rho_\mu(450)$ calculated, for each data set, by the functions given by the fits to the CORSIKA data and equation 5.2.5, for different β_h . %diff is given by equation 5.2.6, where $\beta_h = 0.9$.

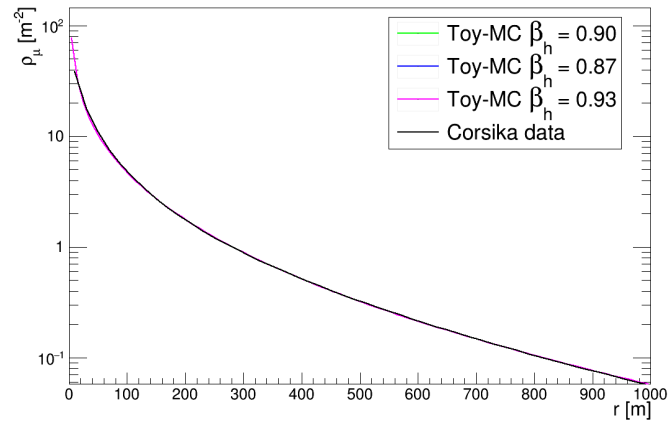


Figure 5.7 – Parametrized LDF given by equation 5.2.5 are in green, blue and purple, and full CORSIKA simulations is in black. Green is with $\beta_H = 0.90$, blue with $\beta_H = 0.87$ and purple $\beta_H = 0.93$. CORSIKA simulations for a proton primary with energy $10^{17.5}$ eV and a zenith angle of 40° .

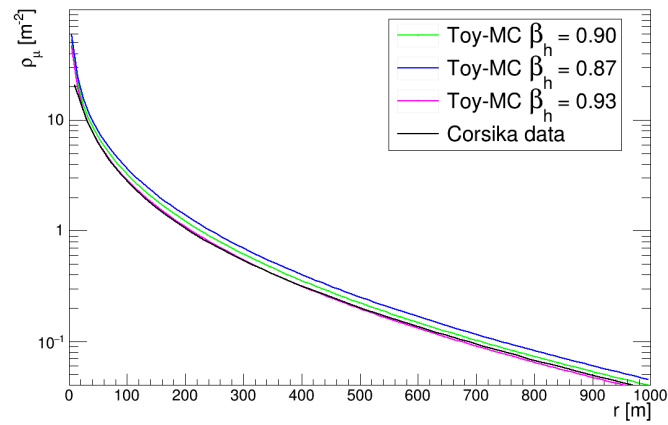


Figure 5.8 – Parametrized LDF given by equation 5.2.5 are in green, blue and purple, and full CORSIKA simulations is in black. Green is with $\beta_H = 0.90$, blue with $\beta_H = 0.87$ and purple $\beta_H = 0.93$. CORSIKA simulations for an iron primary with energy 10^{17} eV and a zenith angle of 38° .

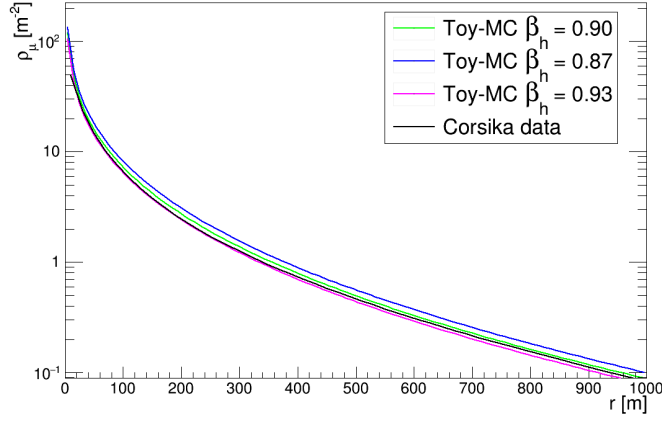


Figure 5.9 – Parametrized LDF given by equation 5.2.5 are in green, blue and purple, and full CORSIKA simulations is in black. Green is with $\beta_H = 0.90$, blue with $\beta_H = 0.87$ and purple $\beta_H = 0.93$. CORSIKA simulations for an iron primary with energy $10^{17.5}$ eV and a zenith angle of 38° .

$$\%_{\text{diff}} = \frac{|\rho_\mu(450, \text{corsika}) - \rho_\mu(450, \beta_h = 0.90)|}{\rho_\mu(450, \text{corsika})} \times 100 \quad (5.2.6)$$

Table 5.3 shows the values of $\rho_\mu(r)$ calculated at $r = 450$ m for the curves given by the fit to the CORSIKA data and equation 5.2.5 for all the sets of data. The $\%_{\text{diff}}$ is roughly 0% when the primary is a proton and 8% to 12% when the primary is iron. While those differences could be smaller, they are still in the range of acceptable results since the goal of the MC is to evaluate if there is enough statistics to do an MLDF measurement.

5.3 MONTE-CARLO SIMULATION STUDIES

Now that a parametrization of a muon lateral distribution function (MLDF) has been found we can proceed with the studies of the feasibility of a reconstruction of an MLDF with our setup using our Monte-Carlo simulation tool. The algorithm for the Toy-MC was succinctly explained in section 5.1. In order to reconstruct the MLDF at TdF, cosmic ray events need to be generated with some input parameters, namely, the primary energy, the primary type and its zenith and azimuth angles. The ground position $((x, y))$ is also generated, uniformly, in an area equal to the Infill area. The distributions for these variables are chosen so that the MC reproduces a flux of cosmic rays that represents the true measured flux, namely the energy, the mass and the arrival distributions. Only with appropriate input variables can the number of muons which will arrive to TdF's detector be found. In section 5.3.2 the distributions of the input parameters are shown.

Knowing the event's ground position $((x, y)$ point) and its zenith and azimuth angle, the minimum distance from the TdF's detector to the shower's axis is computed by using equation 5.3.1. This distance is known as the distance to the shower axis and/or 3D distance, as opposed to the surface distance and/or 2D distance, which is the distance on the ground plane, that is,

$d_{2D} = \sqrt{x^2 + y^2}$. The 3D distance calculation is in appendix A and is found by using equation 5.3.1.

$$d = \left((x^2 + y^2) \cos^2 \theta + \sin^2 \theta (x^2 \sin^2 \phi + y^2 \cos^2 \phi) - 2xy \sin^2 \theta \cos \phi \sin \phi \right)^{1/2} \quad (5.3.1)$$

The zenith angle, the type of cosmic ray (a proton or an iron nuclei) and its energy are used as variables in a lateral trigger probability (LTP) function, which tells if the event is likely to be detected by the T4 trigger condition of Auger's SD array. Essentially, the LTP decides if the event is deleted or saved for posterior analysis.

To normalize the density of muons to a number of muons we use the projected area of the RPC in the shower plane, $A_{\text{proj.}} = A_{\text{effect.}} \cos \theta$, where $A_{\text{effect.}}$ is the effective area of the RPC and it is equal to the area per pad ($0.14 \times 0.18 \text{ m}^2$) times the number of pads in the RPC, 48. Since the density of muons is given as a function of the 3D distance, it is necessary to use the projected area since that is the area of the RPC in the shower plane. Knowing the distance to the shower axis and the projected area for the saved events, the number of muons detected at TdF is finally generated by using a Poisson distribution centered in the average number of muons, which is the output of the input LDF. A 3D histogram is then built using the number of muons at TdF and the 3D distance of the event that generated them. Finally, an MLDF is reconstructed by using the information on the previously drawn 3D histogram.

The number of events generated is given by the integration of the flux of cosmic rays and will be calculated in the next section. Table 5.4 summarizes the initial conditions for the Toy-MC algorithm.

| N. of events | Area [km ²] | CR Type | CR Energy [eV] | CR angle [rad] | N. of pads | Pad area [m ²] |
|--------------|-------------------------|------------------------|---------------------------------|---|------------|----------------------------|
| 67173 | 23.5 | 50% proton 50% iron | $10^{17} \leq E \leq 10^{17.5}$ | $0 \leq \theta \leq \pi/2$ $0 \leq \phi \leq 2\pi$ | 48 | 0.14×0.18 |

Table 5.4 – Initial conditions for the Toy-MC algorithm. There are 48 active pads in the RPC below the TdF's tank.

The energy is random in a distribution of $E^{-3.29}$ eV, with 3.29 being the spectral index for energies below that of the ankle, and the zenith angles go with $\sin \theta$. The area 23.5 km^2 corresponds to the area of the Infill array and a mixed composition explains UHECR's data better than pure compositions, as seen in [11].

5.3.1 FLUX OF COSMIC RAYS: NUMBER OF EVENTS

The graphics that follow are drawn for a number of events calculated by using the cosmic ray flux in a 1-month period from the upper hemisphere in a surface area, A . Knowing that the cosmic ray flux is given by:

$$J(E) = J_0 \left(\frac{E}{E_{\text{ankle}}} \right)^{-\gamma_1} \quad (5.3.2)$$

integrating in the energy range of $10^{17} \leq E \leq 10^{17.5}$ eV and in the upper-hemisphere $0 \leq \theta \leq \pi/2$:

$$N = 2\pi \times A \times \frac{N_{days}}{365.25} \frac{J_0}{E_{ankle}^{-\gamma_1}} \int_{10^{17}}^{10^{17.5}} E^{-\gamma_1} dE \int_0^{\pi/2} \sin(\theta) d\theta \quad (5.3.3)$$

with $J_0 = 3.30 \times 10^{-25} \text{ eV}^{-1} \text{ m}^{-2} \text{ sr}^{-1} \text{ yr}^{-1}$ [69], $E_{ankle} = 5.08 \times 10^{18} \text{ eV}$, $\gamma_1 = 3.293$, $N_{days} = 30 \text{ days}$ and $A = (2 \times 2424)^2 \text{ m}^2$. The number of events is thus $67173 \text{ A}^{-1} \text{ } \Omega^{-1} \text{ month}^{-1}$.

5.3.2 INPUT DISTRIBUTIONS

The following histograms are the distributions of the input variables for 67173 events before the LTP was applied to the data. The distributions of the ground positions of the events generated by the Toy-MC can be seen in figure 5.10. The distribution for the primary type is in figure 5.11 and for the primary angles in figure 5.12. Energy distributions are in figure 5.13. These distributions show that the Toy-MC is rightly represented by the conditions in table 5.4.

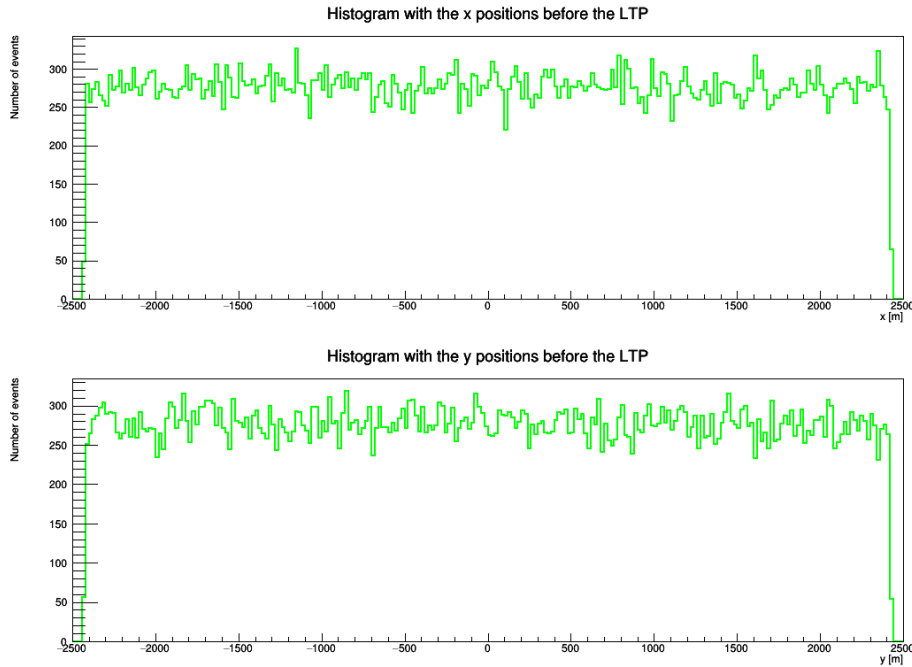


Figure 5.10 – Distribution of the ground positions generated by the Toy-MC algorithm before the LTP was applied. The point (0, 0) is the position of TdF’s detector.

The distribution of the distances, which are shown in figure 5.14 (before the LTP) and 5.20 (after the LTP), show a rapid non-linear decrease of the number of events after the peak which is explained by the *border effect*. Essentially, the number of events increases linearly with the distance because the area of a ring increases linearly with the difference of the radius of the outer and inner circle ($A_{ring} = \pi(r_2^2 - r_1^2)$). The peak is represented by the ring with the bigger area and after the peak, the intersection of a ring with the allowed-area is smaller as the distance increases; this is the *border effect*.

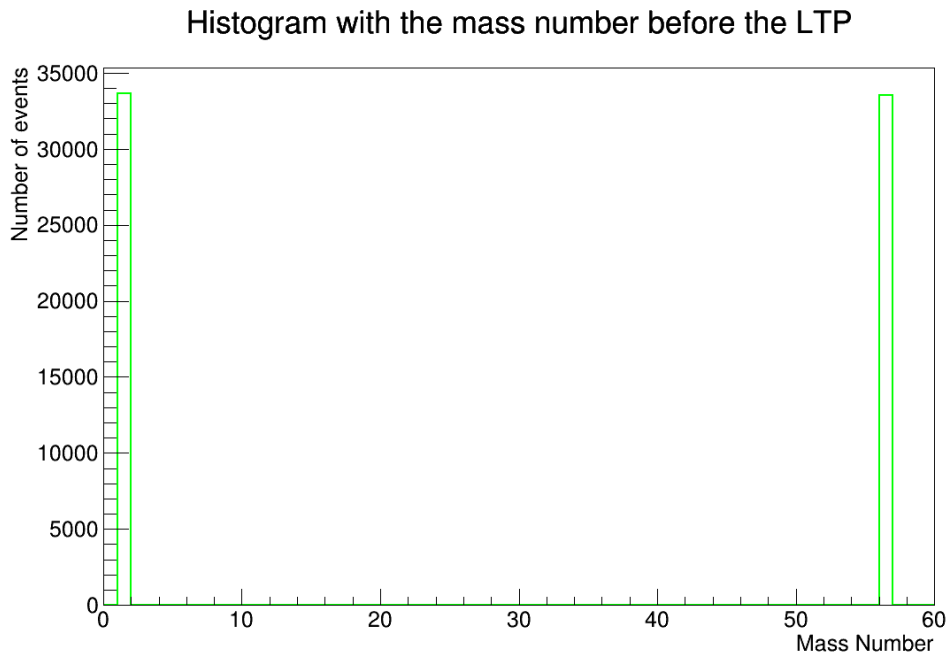


Figure 5.11 – Distribution with the mass of the primary particle generated by the Toy-MC algorithm before the LTP was applied.

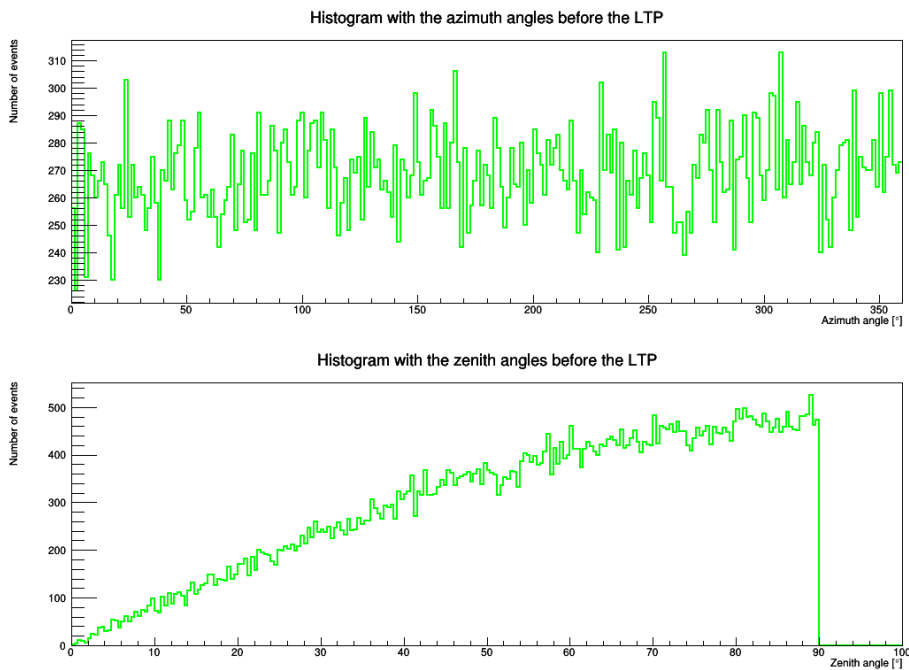


Figure 5.12 – Distribution with the zenith and azimuth angles of the primary particle generated by the Toy-MC algorithm before the LTP was applied.

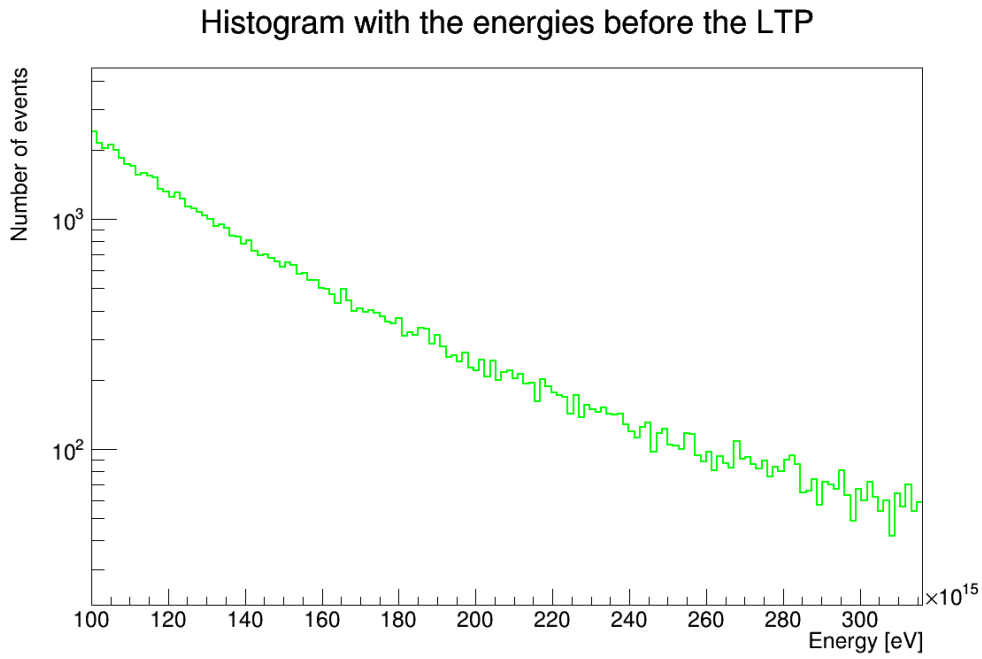


Figure 5.13 – Distribution with the energy of the primary particles generated by the Toy-MC algorithm before the LTP was applied.

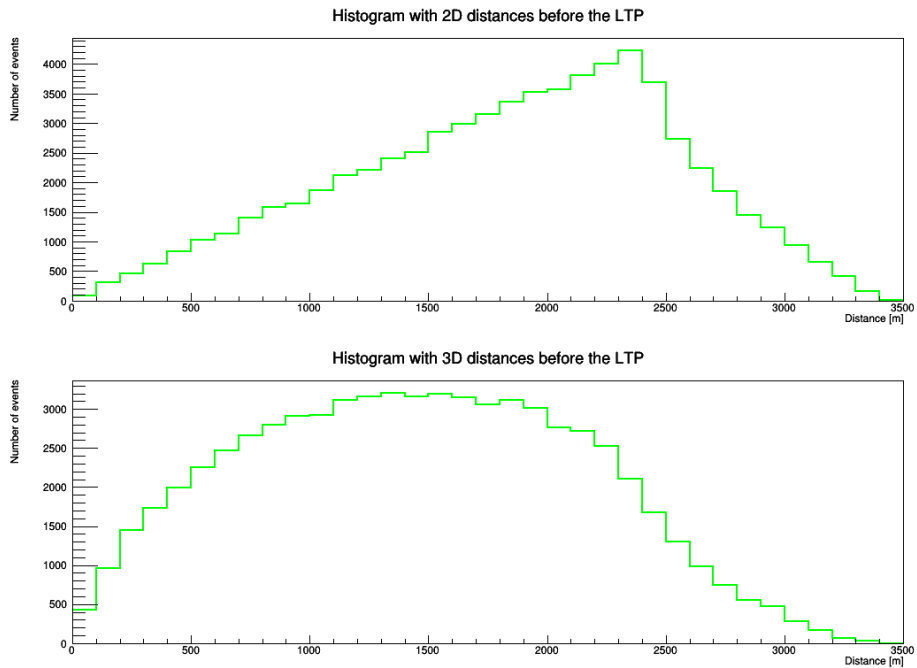


Figure 5.14 – Distribution of the surface-distance and distance to the shower axis (minimum distance) of the events to the surface detector before the LTP was applied.

5.3.3 LATERAL TRIGGER PROBABILITY

The LTP function [70] is given in equation 5.3.4 and table 5.5, where $\text{erf}(x)$ is the error function. Figure 5.15 shows the trigger efficiency as a function of the energy of the primary cosmic ray for two types of primary, proton and iron, and for different zenith angles. It can be seen that the trigger efficiency increases with energy and that, in general, the efficiency reaches its maximum faster for smaller zenith angles.

$$\epsilon(E_{MC}, \theta) = \frac{1}{2} \left(1 + \text{erf} \left(\frac{\log_{10} E_{MC} - a(\theta)}{b} \right) \right) \quad (5.3.4)$$

with E_{MC} being the Monte-Carlo energy of simulations of the T4 trigger and

$$a(\theta) = a_0 + a_1 \cos^2(\theta) + a_2 \cos^4(\theta) + a_3 \cos^6(\theta) \quad (5.3.5)$$

| Parameter | a_0 | a_1 | a_2 | a_3 | b |
|-----------|------------------|------------------|-----------------|------------------|-------------------|
| Proton | 18.65 ± 0.06 | -4.90 ± 0.32 | 4.14 ± 0.57 | -0.98 ± 0.31 | 0.251 ± 0.004 |
| Iron | 18.12 ± 0.05 | -2.52 ± 0.29 | 0.87 ± 0.51 | 0.41 ± 0.28 | 0.220 ± 0.004 |

Table 5.5 – Parameters of the infill T4 trigger efficiency model for proton and iron primaries. [70]

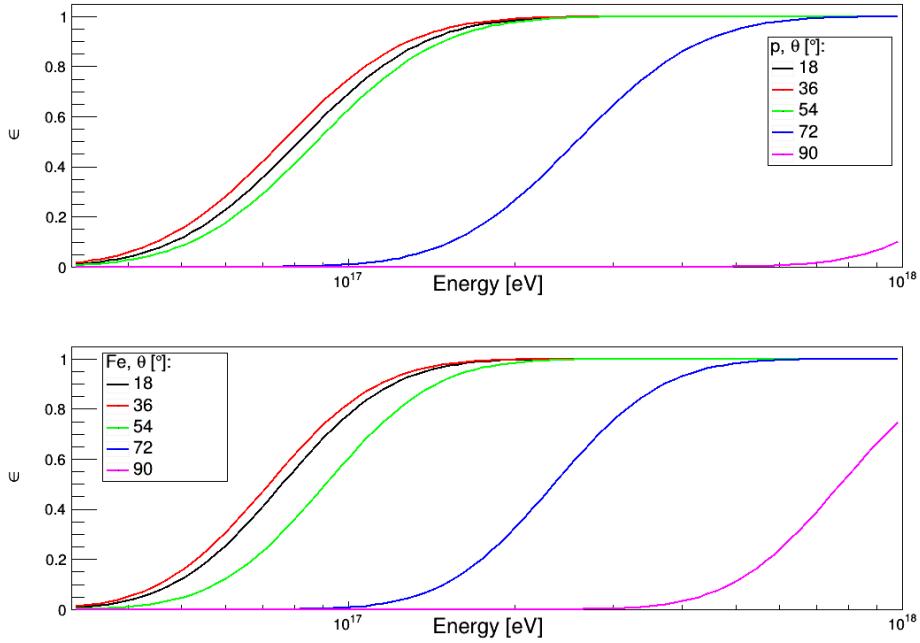


Figure 5.15 – Graphic of equation 5.3.4. Trigger efficiency as a function of energy for proton (upper graphic) and iron (bottom graphic) for different zenith angles.

The error function is given by:

$$\operatorname{erf}(x) = \frac{1}{\sqrt{\pi}} \int_{-x}^x e^{-t^2} dt \quad (5.3.6)$$

5.3.4 OUTPUT DISTRIBUTIONS

The distributions of the input variables after the LTP was applied are shown here. The number of events was reduced from 67173 to 19442 events, a reduction of 71 %. This is mainly due to the LTP being a function of the zenith angle and being less efficient for larger zenith angles, as can be seen in figure 5.15.

Figure 5.16 has the (x, y) positions of the events, figure 5.17 is an histogram of the primary type and figure 5.18 is the distribution for the zenith and azimuth angles. The distribution for the energies and 2D/3D distances are in figures 5.19 and 5.20, respectively.

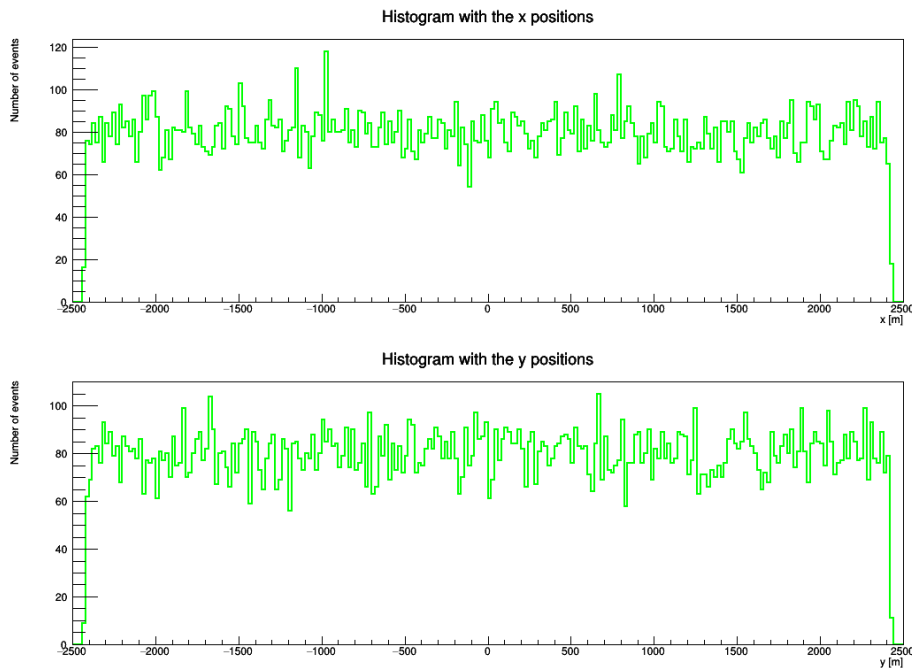


Figure 5.16 – Distribution of the ground positions generated by the Toy-MC algorithm after the LTP was applied. The point $(0, 0)$ is the position of TdF's detector.

Figure 5.21 is an histogram which relates the number of muons with the distance to the detector. This histogram shows the average number of muons expected to be detected by the TdF detector, when the conditions of table 5.4 are met, namely, over a 1-month period and with 48 functioning pads in the RPC. The number of particles detected can be increased by increasing the acquisition time and the effective area of the RPC.

It can be seen that while there are more cosmic ray events for larger 3D distances, most of them generate 0 particles. In contrast, for distances closer to the shower axis, there are not many events but some of them produce many particles: for example, only 9 for distances between 0 m and 50 m but 2 of them generate 37 and 38 muons. This is obviously expected as the density of

Histogram with the mass number

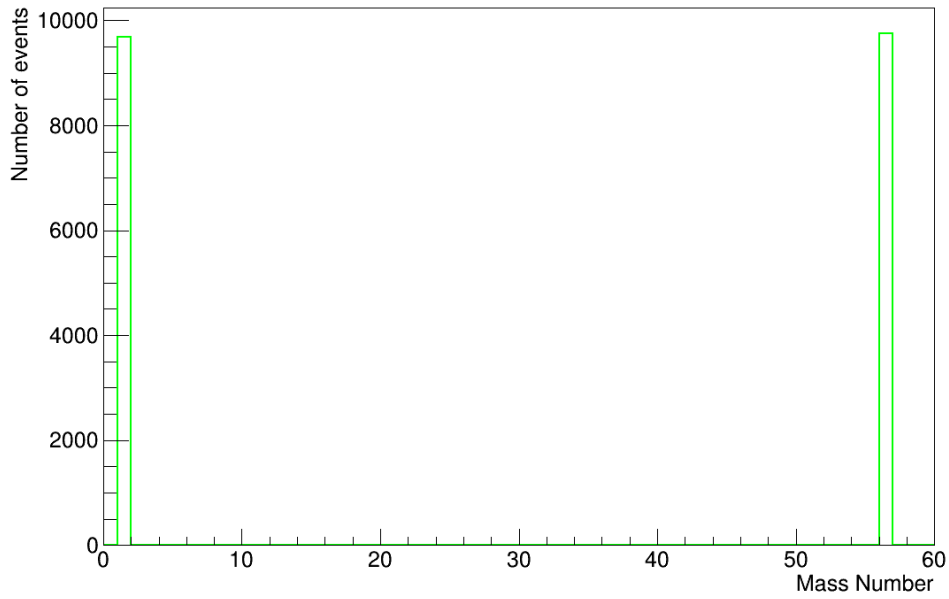


Figure 5.17 – Distribution with the mass of the primary particle generated by the Toy-MC algorithm after the LTP was applied.

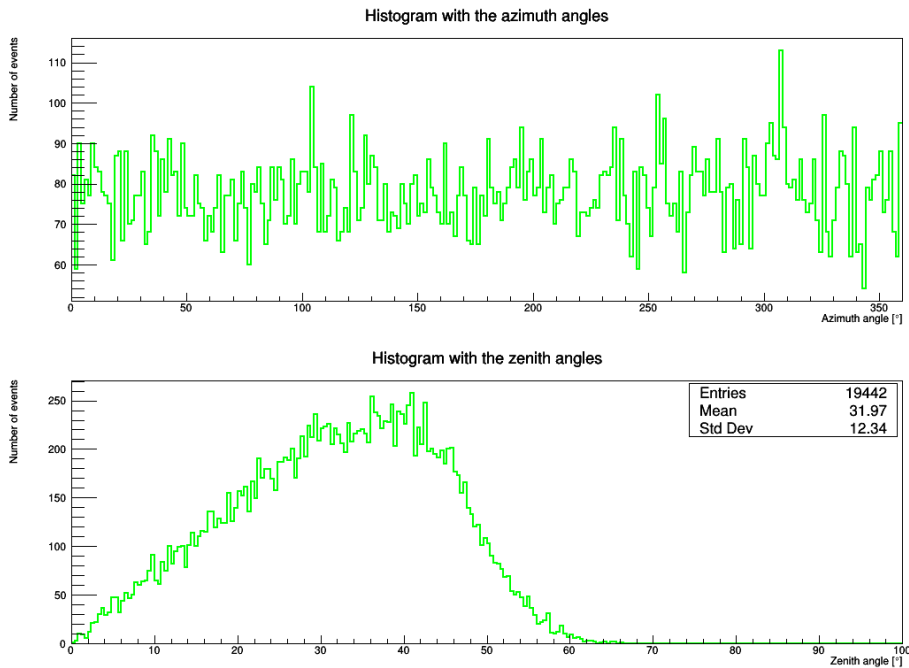


Figure 5.18 – Distribution with the zenith and azimuth angles of the primary particle generated by the Toy-MC algorithm after the LTP was applied.

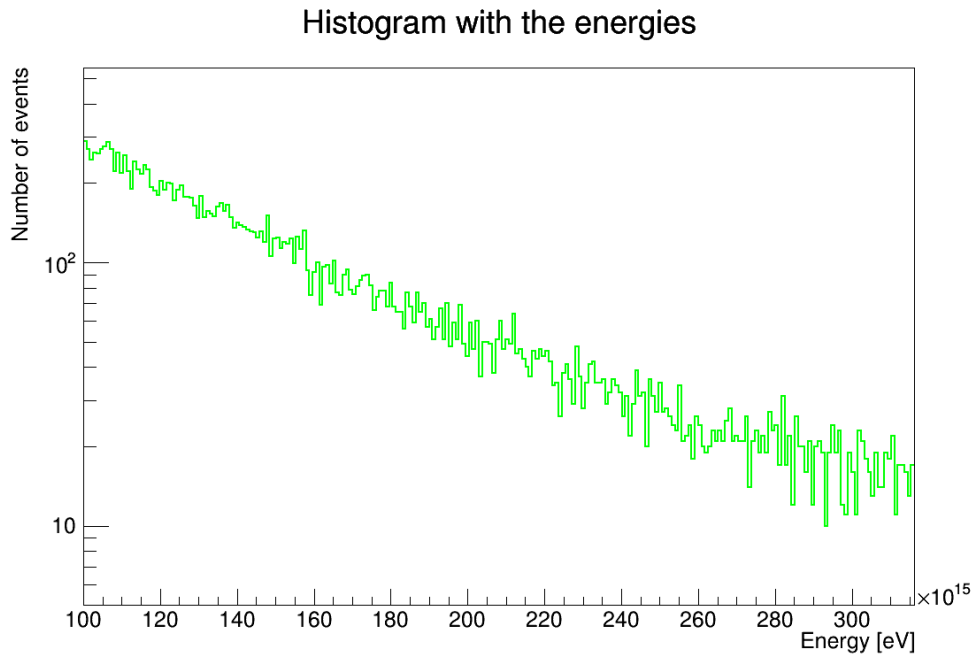


Figure 5.19 – Distribution with the energy of the primary particles generated by the Toy-MC algorithm after the LTP was applied.

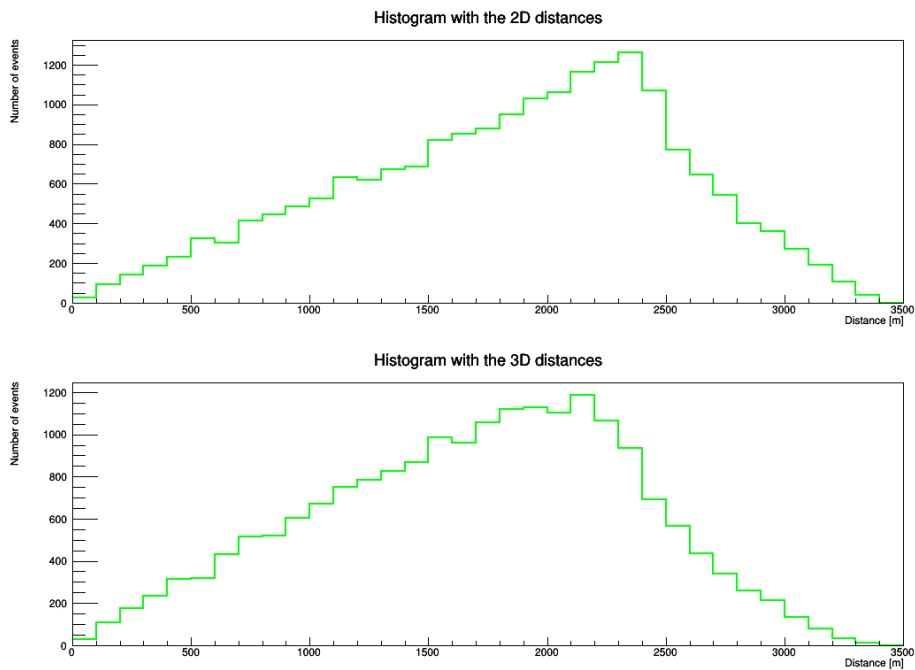


Figure 5.20 – Distribution of the surface-distance and distance to the shower axis (minimum distance) of the events to the surface detector after the LTP was applied.

particles decreases with the distance, as shown by the input LDFs. The reason for having more cosmic ray events for larger distances is because larger distances represent larger areas.

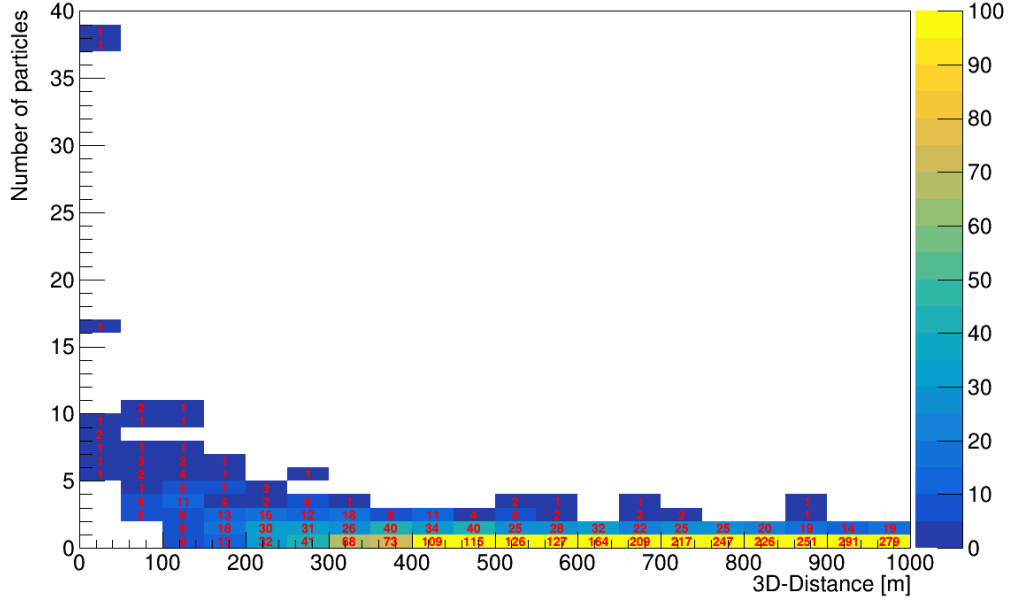


Figure 5.21 – Distribution of the distance to the shower axis and respective number of particles generated by the Toy-MC algorithm.

5.3.5 RECONSTRUCTION OF THE MLDF

A muon LDF is now reconstructed by using figure 5.21. The reconstructed MLDF, figure 5.22, was obtained by the algorithm that follows.

1. Find the mid-point of each distance bin;
2. Find the total number of particles, number of events and projected area of each distance bin;
3. Calculate the average number of particles and the average projected area in each distance bin $\left(\frac{N_{\text{total particles}}}{N_{\text{total events}}} \text{ and } \frac{A_{\text{projected}}}{N_{\text{events}}} \right)$;
4. Find the density of muons in each distance bin, by using $\frac{\langle N_{\text{muons}} \rangle}{\langle A_{\text{projected}} \rangle}$;

The uncertainty in the density of muons in the reconstruction of the LDF is given by the standard deviation as given by equation 5.3.7, where N is the number of events per bin, $\bar{\mu}$ is the average number of muons in each bin and N_{μ_i} is the number of muons for the i th event. The fit follows exactly the same iterative algorithm that was done for the CORSIKA data.

$$\sigma = \left(\frac{1}{N} \sum_{i=1}^N (N_{\mu_i} - \bar{\mu})^2 \right) \quad (5.3.7)$$

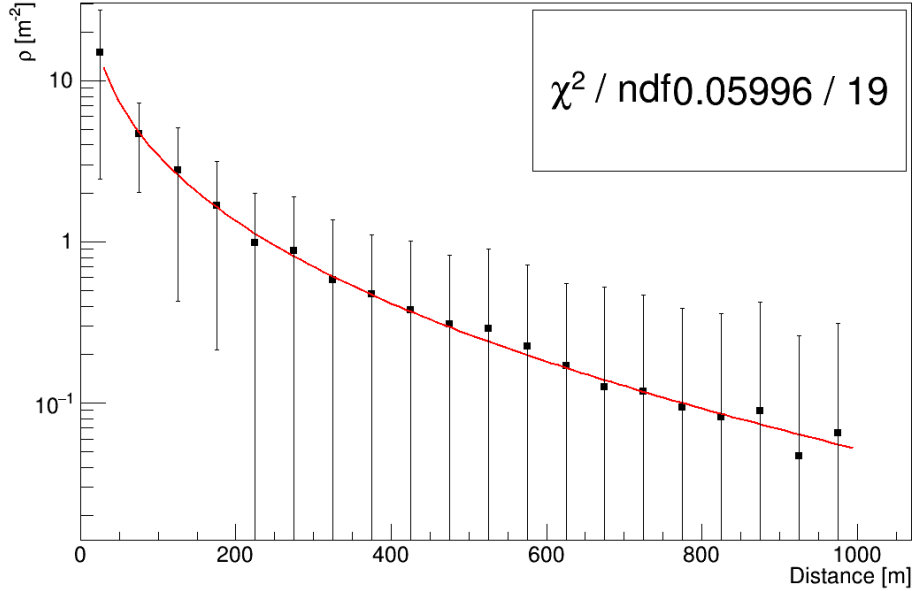


Figure 5.22 – Muon lateral distribution function reconstructed/obtained by the Toy-MC. The fit was done by a χ^2 minimization method and begins at 25 m.

The fit parameters of this reconstructed muon LDF are $N_\mu = 2.4 \pm 0.7$ and $\beta = 1.9 \pm 0.5$.

5.3.6 STABILITY OF FIT PARAMETERS

There are two fit parameters, N_μ and β , and two changeable input variables, the acquisition time and the number of pads. One can improve the reconstruction of the average MLDF by changing these two variables.

Figure 5.23 shows the relative change of the fit parameters with the acquisition time and number of pads. It can be seen that an increase in acquisition time does not guarantee better fit parameters. When increasing the number of pads, that is, when increasing the effective area of the RPC, the fit parameters get better. A maximum distance of 1500 m, instead of the shown 1000 m, was also tested and there were no significant improvements in these results.

5.4 ELECTROMAGNETIC CONTAMINATION

When working with real air shower's data, such as the data obtained with TdF's RPC, it is mandatory to know about the EM component of an air shower. Even though the RPC is below

5 Towards an MLDF at TdF

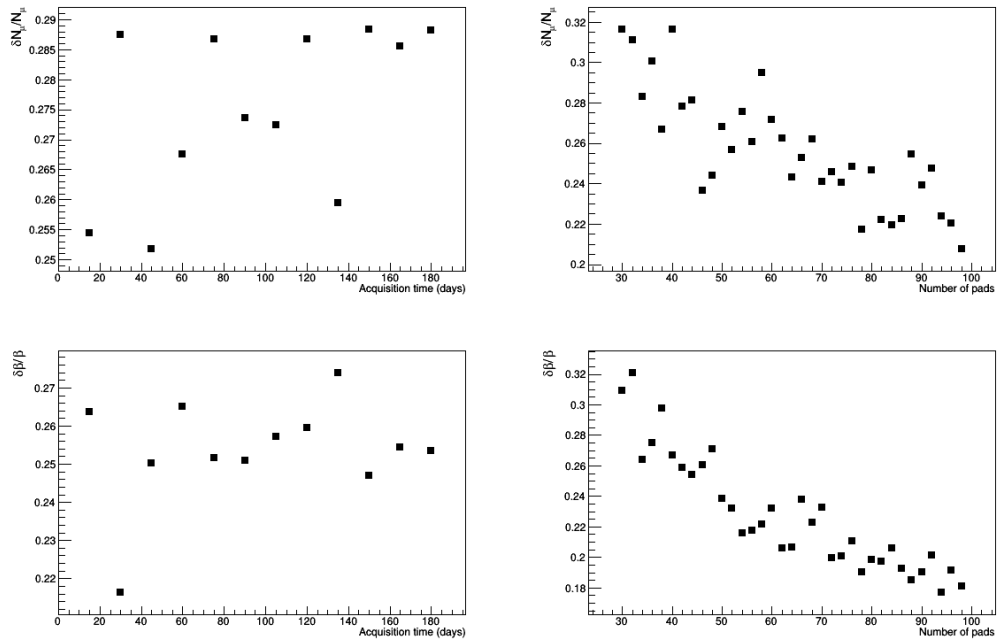


Figure 5.23 – Graphics of the relative change of the fit parameters with the acquisition time and number of pads. The default acquisition time is 30 days and the default number of pads is 48. $\delta \beta / \beta$ is the relative uncertainty in β .

a mass of water, the EM contamination is not negligible. As such, the study of the EM component under our experimental conditions is a necessary step in order to obtain an accurate number of muons by subtracting from the measured particles those that are EM particles. This is done by analyzing simulations designed in such a way that they represent the experimental apparatus that is used for the detection. The graphics in this section are for simulations using QGSJet-II-04 done in the framework of the AugerPrime upgrade studies with the Offline software and consider Water-Cherenkov tanks with 4 RPCs below. Here, it is considered, again, a proton/iron primary with a primary energy of $10^{17}/10^{17.5}$ eV. The zenith angle is 40° when the primary is a proton and 38° when the primary is an iron nuclei. The graphics below are the relative EM component, $\frac{\langle EM_{\text{particles}} \rangle}{\langle N_{\mu} \rangle}$, as a function of the core distance. The EM_{hits} were found by subtracting the number of muon hits from the total hits.

Figures 5.24 is for proton primary with 10^{17} eV (top) and $10^{17.5}$ eV (bottom). It shows that at a core distance of roughly 200-300 m the number of EM particles is larger than the number of muons detected by the 4 RPCs. As the distance increases, the EM component starts being absorbed by the atmosphere and the muon component dominates. At around 700 m, the EM component seems to be about 20-30 %.

Figures 5.25 are the relative number of EM particles with respect to the number of muons for simulations initiated by an iron primary with 10^{17} eV (top) and $10^{17.5}$ eV (bottom). At 700 m, the EM component is around 20 %.

This does not mean that we have to consider only events with a distance to the shower axis larger than 700 m. Since we are interested in finding out how many muons there are in the number of particles detected, we could do a parametrization of the curves with the distance and calculate the muon purity for each event given by the distance from the detector to the shower. It is, however, important to note that these simulations are for QGSJet-II-04 and such a parametrization could be model dependent. A more detailed analysis would need to be done to conclude on what the best course of action would be.

Another thing that needs to be considered are the atmospheric muons. When an RPC detects a muon, it does not guarantee that the muon is from a given air shower, it could be a muon from another air shower, called an atmospheric muon. The rate of atmospheric muons in MARTA's RPCs was shown to be in the order of 350 particles per minute per pad [71]. The influence of those 350 particles per minute per pad in the detection of air-shower muons is negligible. For example, considering the number of events after the LTP in the Toy-MC tool (19442), the total number of atmospheric particles that would be detected in an RPC with 48 pads would be:

$$N_{\text{atms},\mu} = \frac{350 \text{ particles}}{60 \text{ s} \times \text{pad}} \times 19442 \text{ events} \times 1 \times 10^{-6} \frac{\text{s}}{\text{event}} \times 48 \text{ pads} = 5.4 \quad (5.4.1)$$

The 1×10^{-6} s is the time window to search for hits, in the RPC, for each event. These 5.4 muons would be distributed over all the Infill area since that is the area we used for the cosmic ray flux. Considering only distances closer to the shower axis the number of atmospheric particles detected would be lesser than 5 particles over a 1-month period, which is surely negligible.

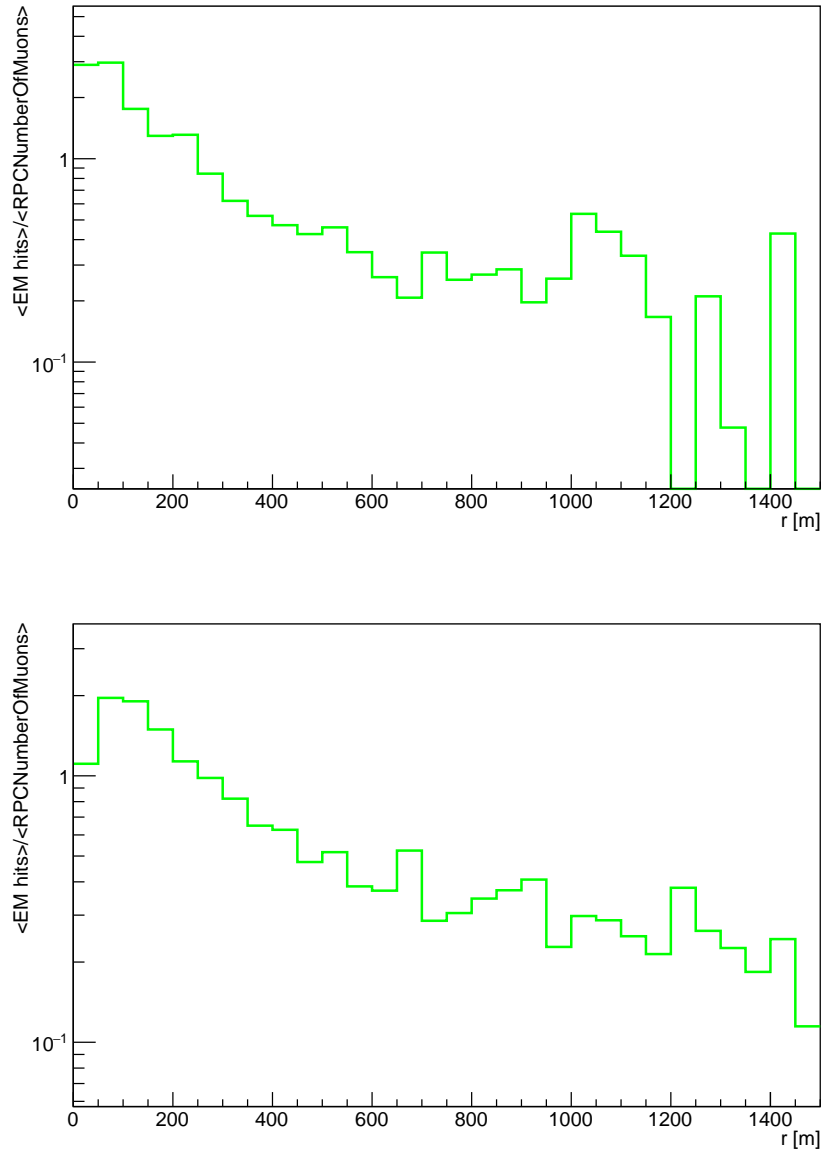


Figure 5.24 – Average number of EM particles relative to the average number of muons measured by 4 RPCs below WCDs as a function of the core distance. Top is for a proton primary with 10^{17} eV and bottom for a proton primary with $10^{17.5}$ eV. Both for $\theta = 40^\circ$. The simulations consist of 422 events for the top graphic and 498 for the bottom one. The hadronic interaction model used is QGSJet-II-04.

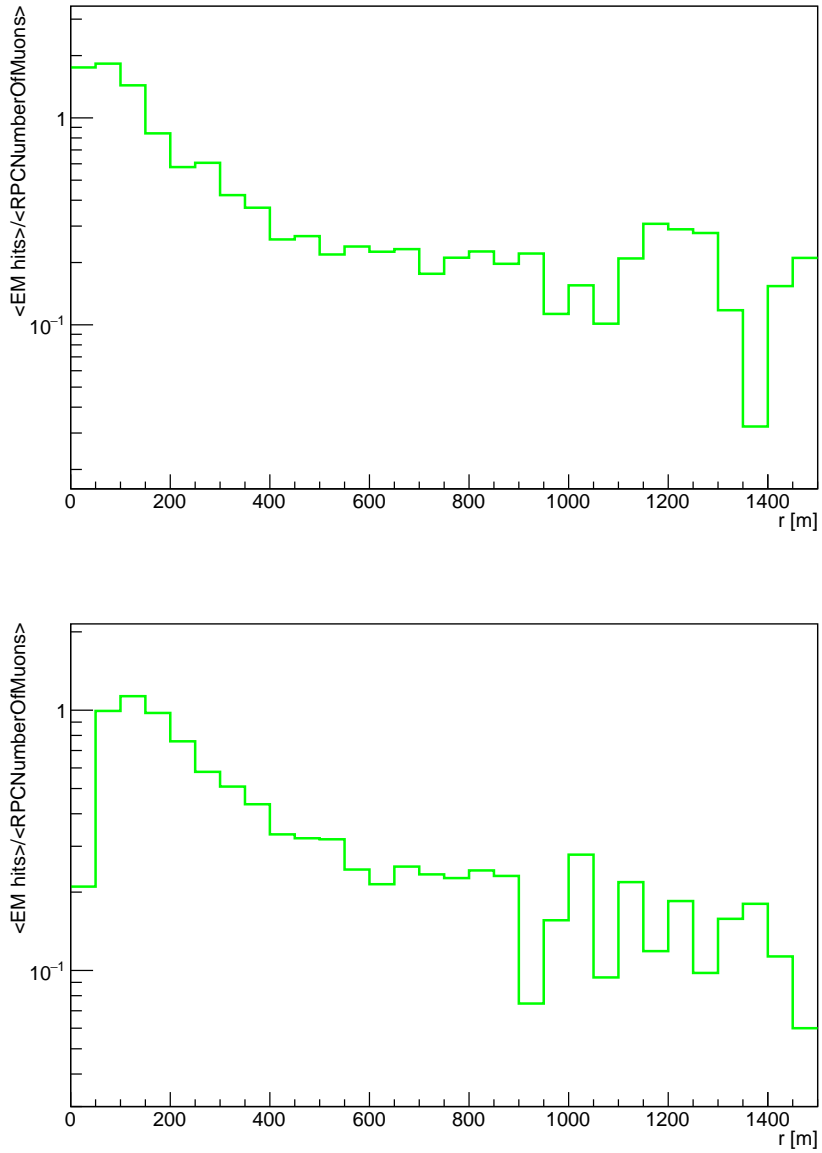


Figure 5.25 – Average number of EM particles relative to the average number of muons measured by 4 RPCs below WCDs as a function of the core distance. Top is for an iron primary with 10^{17} eV and bottom for an iron primary with $10^{17.5}$ eV. Both for $\theta = 38^\circ$. The simulations consist of 438 events for the top graphic and 405 for the bottom one. The hadronic interaction model used is QGSJet-II-04.

6 DATA ANALYSIS

This section will focus on data obtained by the experimental setup in the station *Tierra Del Fuego* (TdF) as well as an introduction to the setup itself. For the objective of this thesis, which is to get a mean muon LDF at TdF, one needs to obtain a muon density at TdF and its respective distance to the shower axis. Since the muon density will be measured by the use of RPCs, three sets of analysis will be presented here:

- T3 requests to TdF;
- RPC's data;
- Monitoring of the RPCs;

The *T3 requests to TdF* will allow us to obtain information regarding the reconstruction of an event by the CDAS. This is a necessary step to find the distance from the shower axis for a given event. The data taken by the RPCs, which is essentially how many particles per event the RPCs detected, is the main observable to calculate the muon densities at TdF. Finally, the monitoring of the RPCs needs to be done to provide information regarding their state and their usefulness to the measurement in question. Here, the RPC's efficiency will be found to, together with the number of particles, obtain the *true* density of muons.

Each sub-section will focus on a particular set of data, namely, T3 requests to *Tierra Del Fuego* (T3 file), particles detected by the RPCs (main data file) and monitoring of the RPCs.

6.1 EXPERIMENTAL SETUP

This station's experimental setup is the first prototype of the MARTA project [54]. The MARTA project aims for a more precise measurement of the muon content of extensive air showers. It consists of 8 tanks in the infill region but in a different configuration in which the tanks are separated by 10 m instead of the usual 750 m. The project's idea is for 4 RPCs below the WCD. The mass over-burden of the water, tank, and the pre-cast used to lift it, provides some shielding from the EM component. However, the station that is used in this thesis has two RPCs, not 4, below the WCD, one on top of the other. The tank in which these RPCs are installed is named after *Tierra Del Fuego*, shortened to TdF.

Figure 6.1 is a picture of this tank. Figure 6.2 shows the position of the two RPCs with respect to the tank and a zoom on the RPCs and figure 6.3 shows the position of the RPCs with respect to the PMTs (left) and a map with the coordinates of the pads (right). The RPCs are in the same position vertically in order to define a trigger condition using one RPC and to measure the efficiency in the other one [72]. This work will focus on data obtained with the top RPC.

The RPCs consist of 8 plates each with 8 pads (8×8) with a sensitive gas volume of $1200 \times 1500 \times 1.9 \text{ mm}^3$ and the area of each pad/electrode is $180 \times 140 \text{ mm}^2$. Of a total of 64 pads

for each RPC, 56 (7×8) are instrumented from the top RPC and 24 (3×8) from the bottom RPC. The RPCs are closed inside an acrylic box and 9 sensors for temperature, 1 for pressure and 2 to measure the relative humidity are placed in the surface of the RPCs.¹ All these parts are also closed in a sealed aluminium shielding box that provides some safeguards against changing environmental conditions.



Figure 6.1 – Picture of TdF’s station. Below the tank there are 2 RPC units, one on top of the other. [74]

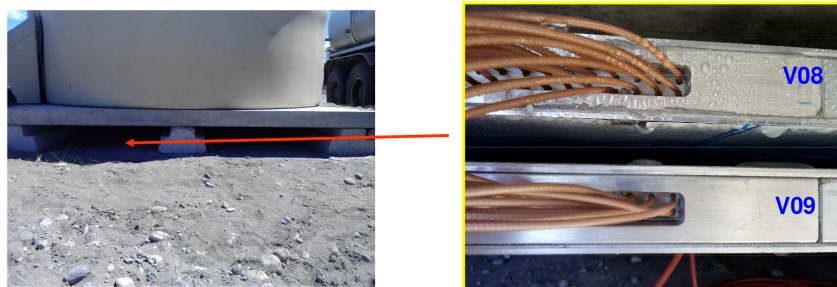


Figure 6.2 – Picture representing the position of the two RPCs in TdF’s station a zoom of the RPCs. [74]

Since this station is not standard when compared to the bulk of surface detectors in the observatory, it needs additional hardware and software. This thesis is not about these changes to the default setup. However, a very brief description of the data acquisition system follows.

6.1.1 DATA ACQUISITION SYSTEM

In order to have reconstructed information regarding a cosmic ray event, such as the primary energy and the core distance to TdF’s station, one has to combine information obtained with several surface stations. Data obtained with TdF’s RPCs are not sufficient for event analysis, and as such, TdF’s single board computer (SBC) needs to communicate with CDAS. The SBC records a

1. For a detailed description of these RPCs see [73].

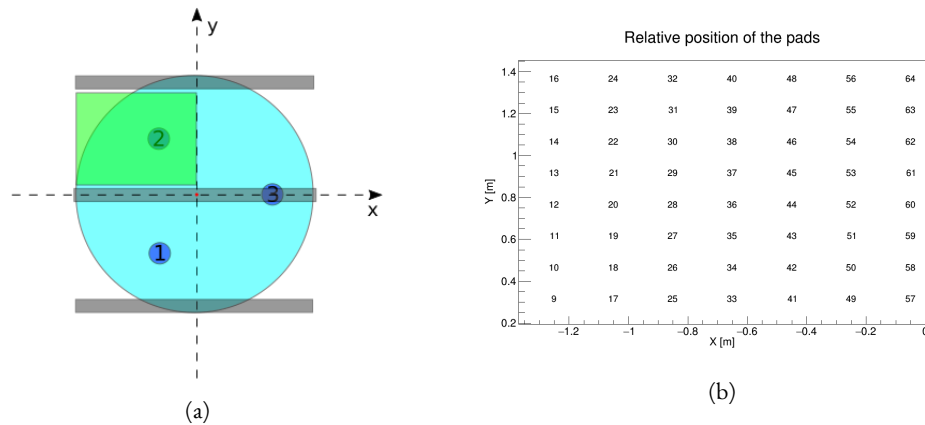


Figure 6.3 – Left: Scheme of a top view of TdF's station. Light blue represents the Cherenkov tank and in dark blue, numbered from 1 to 3, are the PMTs. In dark-grey are the concrete precasts which serve to lift the tank. Below the tank, represented as green, there are 2 RPCs, one on top of the other. Image is not to scale. Right: Map of pad's positions.

T1 table with several hundred of the last events that verified the T1 condition, which is a single detector trigger. A T3 trigger is done at the CDAS which sends a T3 request to the needed SD's, perhaps TdF. After a T3 request is done to this station, the event that triggered this T3 is looked-up in the T1 table and from this interaction it obtains the respective GTS and LTS, global time stamp and local time stamp, respectively. After a T3 request is verified, some data regarding this event is sent to a Raspberry Pi (which is also located at TdF) and written to a file which we call *T3 file*. This data contains the GPS and LTS.

The RPCs are connected to the tank's unified board (UB) and are programmed in such a way that when an event passes the T1 trigger and a pad on the top RPC is activated the RPC's information regarding the state of the pads for that event along with the LTS and tank time-stamp is saved on a file for posterior analysis.

6.2 T3 REQUESTS TO TdF

The T3 file is a CSV file in which each line corresponds to a different event. When a T3 trigger request (henceforth abbreviated to T3 request) is made to the TdF station, the following information is written to this T3 file:

- t3_evid;
- t3_offset;
- t3_window;
- t3_GPS_second;
- t3_GPS_micro;
- t3_ID (LTS);
- t3_delay;

For this thesis, the important parameters are the GPS and the `t3_ID`, which is the LTS.

The `t3_window` is a time window, in microseconds, for a T3 trigger request by the CDAS to the SDs. It can have 3 values, 0, 20 or 30. A T3-window of 0 is a normal T3, as explained in section 3.3.2. T3-window of 20 is a trigger by the FDs and a T3-window of 30 μs is an event that had, in a given surface station, a T3 but not a T2. This is possible when a T1 is within 30 μs of the T3 while having the T2 condition denied. In the time period analyzed here, there were 176681 SDs with a T3-window of 0 and 79817 SDs with a T3-window of 30.

This T3 file has data acquired between 07/December/2016 and 11/January/2017, 36 days. This file serves as the bridge between data taken by the RPCs and ADST (Advanced Data Summary Tree) files. Using this T3 file one can query ADST and CDAS files to find the relevant reconstructed information such as the core distance to the TdF station, which is needed for the reconstruction of an LDF at TdF.

In the time frame of this thesis, the bridge between this T3 file and the RPCs data could not be done. We can, however, still query the CDAS and ADST files for the relevant time period and find some relevant information pertaining to this T3 file.

6.2.1 QUERYING CDAS FILES

A cosmic ray event detected by Auger's surface detector array which is also in the CDAS files can be associated with a given event in the T3 file by comparing their GPS time, since both the events in the CDAS and in the T3 file have that timing information readily available.

Using the *Offline* framework with the goal of having a deeper understanding of the T3 file and its capacity to bridge the RPC's data to tank's data, the following was done:

- Find the number of events in the CDAS in the relevant time period;
- For all the events in the CDAS for the relevant time period, find how many times TdF accepted the T3 request;
- Find how many events are simultaneously in the 2 files, CDAS and T3 file;
- For the events that are in both files, add a column to the T3 file with the ID of the event in the CDAS;
- For the events that are in both files, add a column to the T3 file with a 1 or 0, depending if the TdF accepted the T3 request or not, respectively;

The two added columns will prove useful when analyzing ADST files.

By querying the CDAS files and comparing it to the data in our T3 file, the following information was compiled:

The rate of events in the T3 file is about 116 events per day and 225 had T3 accepted by TdF. The efficiency in saving events in the T3 file is about 2%, 4176 in 180210 events. The reason for this low efficiency in saving events is still not understood.

The number of events in the T3 file (4176) is expectedly larger than the number of events in that file that had the T3 condition accepted by TdF (225). The difference between these two numbers are events in which the T3 request was not accepted by TdF. The T3 condition was already explained in section 3.3.2. It requires spatial and temporal coincidences between the T2 from different surface stations and, if those are not met, the T3 request is denied. An event can, however,

| | |
|---|-------------|
| Number of events in the CDAS | 474668 |
| T3 requests to TdF | 180210 |
| Accepted T3 requests | 8703 |
| Events in the T3 file that had T3 accepted by TdF | 225 |
| Events in the T3 file | 4176 |
| Events in both files (CDAS and T3) | 4176 |
| % of saved events | ≈ 2 |

Table 6.1 – Information relative to the comparison of the T3 file with the CDAS files. All numbers are correspondent to cosmic ray data taken between 07/December/2016 and 11/January/2017. % of saved events is the ratio between the number of events in the T3 file and the T3 requests to TdF (obtained by the CDAS) in that time period.

have the T3 request denied by a given station and still transition to a T4, T5 and eventually be reconstructed.

6.2.2 QUERYING ADST FILES

The GPS time in the T3 file can also be used to find the respective event, if present, in the ADST files. Only cosmic ray events that passed all triggers and are successfully reconstructed appear in those files. By querying the ADST files for cosmic ray events in the period of our acquisition time the following steps were taken in order to have some additional information regarding the events in the T3 file, which are useful events towards obtaining a mean muon LDF at TdF.

- Find the number of events in that time period in which TdF participated in its reconstruction;
- Find the number of events in the ADST files in that time period;
- Find the number of hits (same GPS second and nanosecond in both files);
- Add a new column to the T3 file answering "Is the event in the ADST files?";
- Count the number of events in the T3 file that are also in the ADSTs and had T3 accepted/denied by TdF;
- Find the number of events that are in both files, had T3 accepted by TdF and TdF participated in its reconstruction;
- Find the number of events, in the acquisition time, that had TdF in the list of stations;
- Draw distributions for the energy, zenith angle and total signal in TdF's station for the cosmic ray events that are in the T3 file and had T3 accepted by TdF;

Table 6.2 summarizes the results of comparing our T3 file with the ADST files relevant to the time period in question.

Of the 225 events that are in the T3 file and had T3 accepted by TdF, as we previously found by querying the CDAS files, 93 of those were reconstructed in the Infill SD array with the help of TdF's station.

Of the events that are in both files (1037), 9% were reconstructed with the help of TdF (94). In section 5.3.5, we reconstructed an MLDF with 19442 simulated cosmic ray events and obtained,

| | |
|--|-------|
| Number of events in the ADSTs | 45338 |
| Events in both files (hits) | 1037 |
| Events in ADST with T3 accepted by TdF | 93 |
| Events in which TdF participated | 4156 |
| Hits in which TdF participated | 94 |

Table 6.2 – Information relative to the comparison of the T3 file with ADST files. All numbers correspond to cosmic ray data taken between 07/December/2016 and 11/January/2017. *Hits* refers to events that are simultaneously in both the T3 file and in an ADST file.

from the fit of the muon density as a function of distance, a relative uncertainty of $\approx 29\%$ and $\approx 26\%$ for the fit parameters N_μ and β , respectively. With only 93 events, the relative uncertainty in a MLDF reconstruction would be too large. To improve the reconstruction of an MLDF at TdF, the acquisition time would need to be expanded. Other than increasing the acquisition time, the number of events in which TdF participated in their event reconstruction could be increased by increasing the % of saved events, which we saw in the previous sub-section to be 2%.

Figures 6.4, 6.5, 6.6 show the reconstructed primary energy, zenith angle and distance from the shower axis to TdF. These distributions are for cosmic ray events that are simultaneously in the T3 file and ADST files, had T3 accepted by TdF and in which TdF participated in its reconstruction.

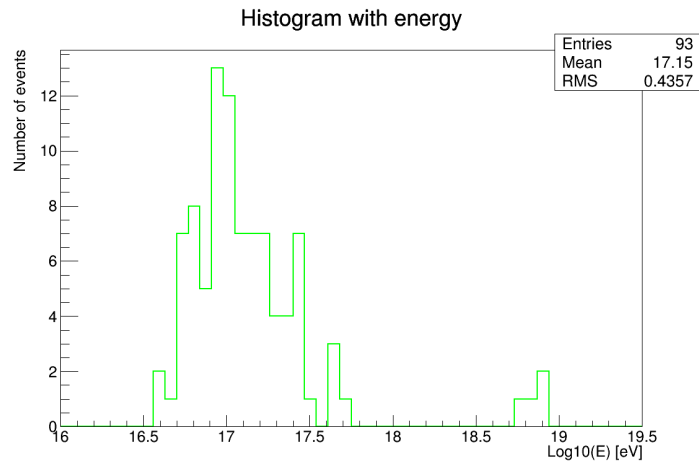


Figure 6.4 – Reconstructed energy of the primary particle for the events that are both in the T3 file and ADST files, had T3 accepted by TdF and in which TdF participates.

The distribution of the reconstructed energy, figure 6.4, shows two opposing behaviors: the decrease of the cosmic ray flux with an increase in energy and an increase in the LTP with an increase in energy. There are more events for a primary energy in the range $[10^{17}, 10^{17.5}]$ eV than $[10^{16.5}, 10^{17}]$ eV due to the surface array being less efficient for those energies, as figure 6.7 shows. There are no events with an energy in the range $[10^{18}, 10^{18.5}]$ which could be explained by the decrease in the flux of cosmic rays when compared to lower energies. Because of that, the regular surface array (as opposed to the infill array), is more likely to detect such events. As seen in figure

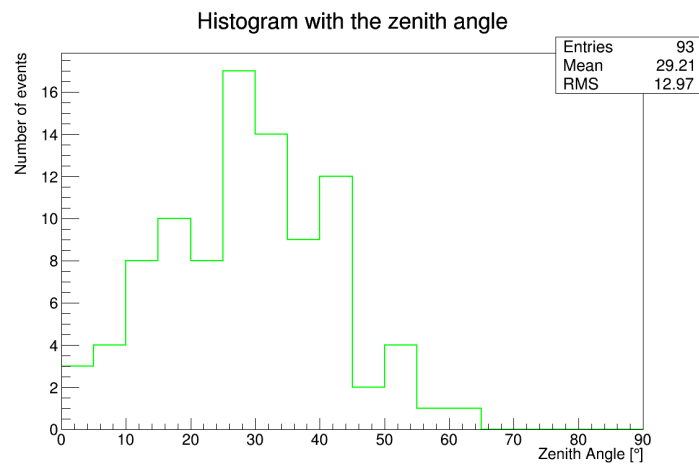


Figure 6.5 – Reconstructed zenith angle of the primary particle for the events that are both in the T3 file and ADST files, had T3 accepted by TdF and in which TdF participates.

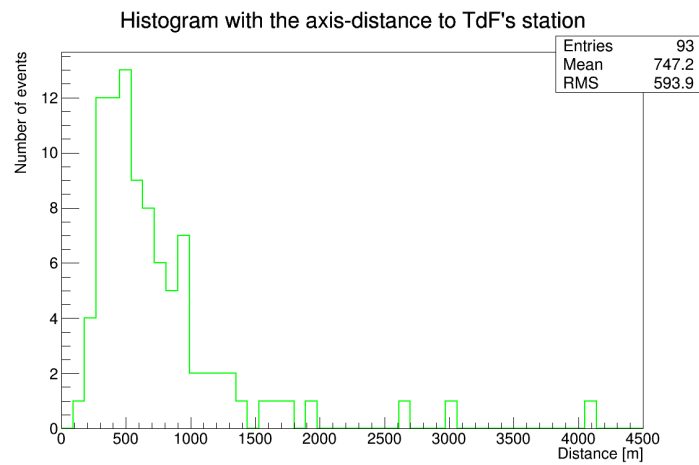


Figure 6.6 – Distribution of the axis' distance to TdF's station for the events that are both in the T3 file and ADST files, had T3 accepted by TdF and in which TdF participates.

6.7, the LTP for the regular surface array reaches 1 only at around $10^{18.7}$, for both proton and iron primaries.

Figure 6.6 are the distances from the shower axis to TdF that would be considered for the final average muon LDF.

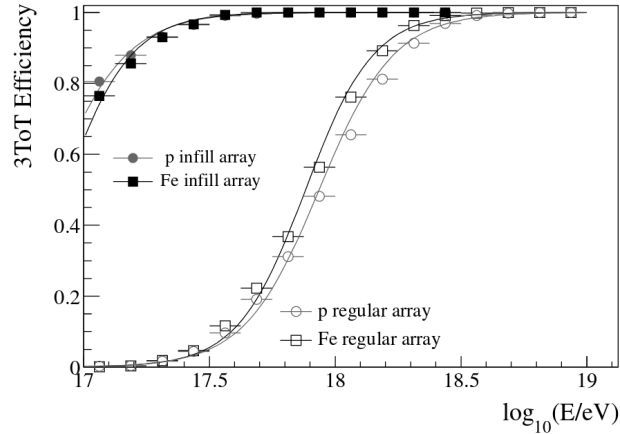


Figure 6.7 – Efficiency of the 3ToT trigger for both the infill and regular array from simulations of iron and proton primaries. [75]

6.3 RPC'S DATA

The main file with the data obtained with the top RPC has essentially 4 columns of information and each line represents a different cosmic ray event:

- Tank timestamp;
- Marta ID (Tank ID);
- Channels;
- Date (Of the form Wed 7 15:18:00 2016)

The RPC file that will be studied in this chapter acquired data between 7/Dec/2016 and 3/Jan/2017. The channels column is of particular interest as the information whether or not a particular pad detected a particle is shown with a 1 (detected a particle) or a 0 (did not detect a particle). The condition for writing an event to this file is a T1 trigger in the tank in combination with at-least 1 hit in the TOP RPC.

In addition to this RPC file there is also a file with background data which will be analyzed first.

6.3.1 BACKGROUND PARTICLES

In order to validate the state of each pad, one needs to study their background detection. A file with the background frequency for each pad along with the time of detection is also studied

here. The file with the background data has 81 columns, one for each pad and an additional column with the date. The file analyzed here has data taken between 7/Dec/2016 and 9/Jan/2017. Every 10 minutes, roughly, a different measurement is done and written to the file.

The background frequency for each pad can be in 3 intervals, depending on its state:

- Dead pad: $f_{\text{background}} = 0$ Hz;
- Active pad: $0 \text{ Hz} < f_{\text{background}} < 1000$ Hz;
- Noisy pad: $f_{\text{background}} \geq 1000$ Hz;

Only active pads are of interest for an accurate description of the physics of cosmic rays, noisy and dead pads need to be removed from the analysis. Figures 6.8 and 6.9 show the number of active pads and the average background frequency for active and non-active pads, respectively.

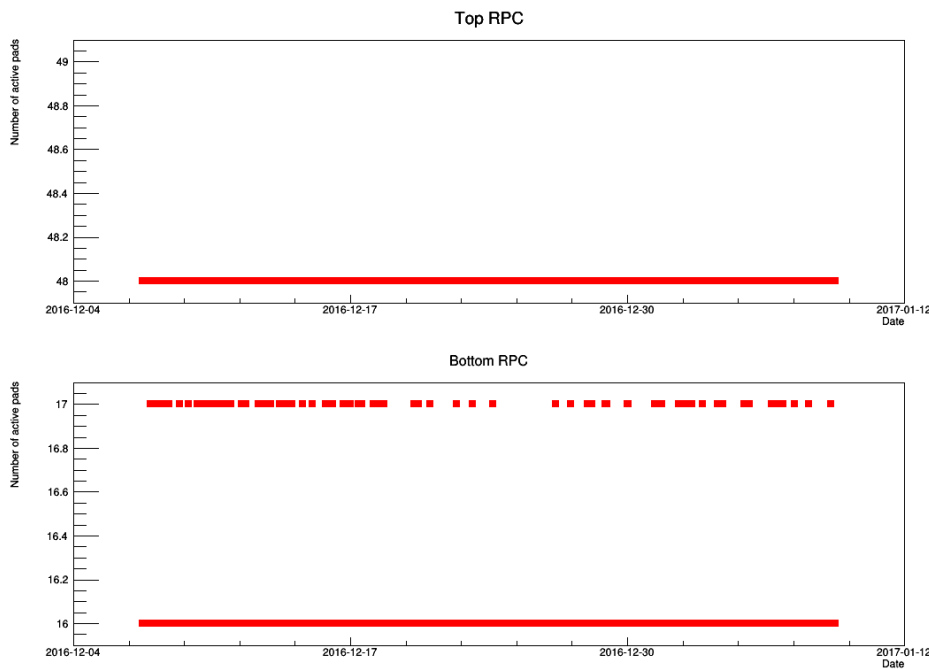


Figure 6.8 – Number of active pads as a function of date for the top (top figure) and bottom (bottom figure) RPCs.

Knowing that the top RPC is composed of 56 pads, figure 6.9 shows that the number of active pads is stable over time and that 8 pads are not active. Those 8 pads correspond to the last 8 of the top RPC which make an RPC plate. By removing those 8 pads from the analysis, figure 6.9 bottom left shows that the background frequency behaves as expected. An analogous study was done for the bottom RPC.

The bottom left graphic in figure 6.9 shows that there are two regimes for the average background when considering only active pads. One is centered at around 60 Hz and the other at around 90 Hz. This could be some electronic miss-behavior, for example, a bad contact. While this is not worrisome, since the frequencies are well within the range for an active pad, it is something that needs to be considered. The same behavior is also seen for the bottom RPC.

6 Data Analysis

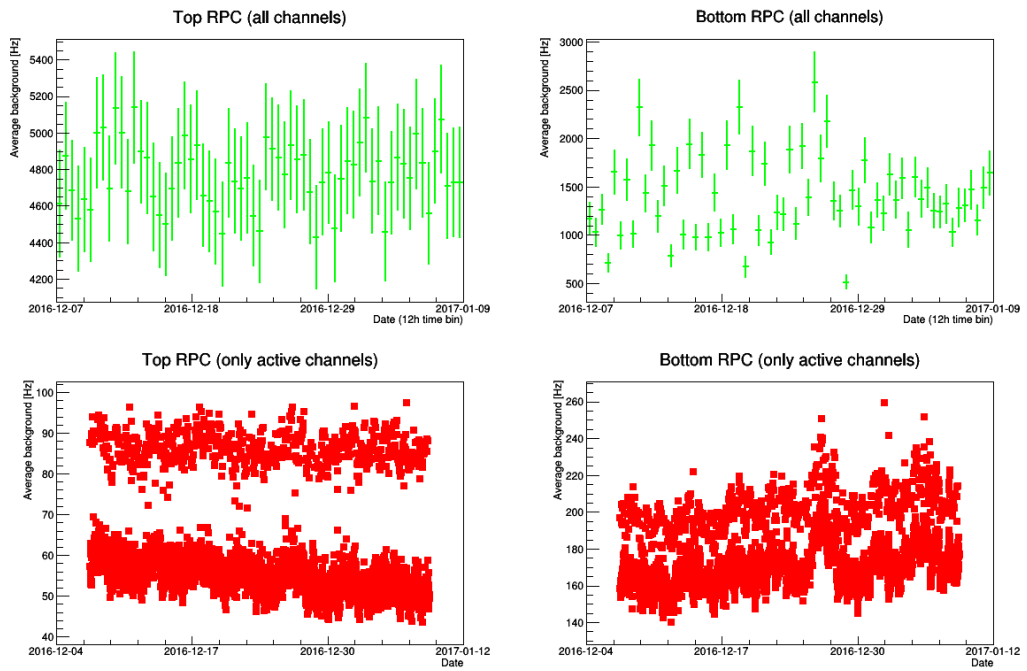


Figure 6.9 – Average value of the background frequency as a function of date for the top (left figures) and bottom (right figures) RPCs, for all channels (top figures) and active channels only (bottom figures). The top figures are TProfiles: the interception of the horizontal bar (width of each bin) with the vertical bar is the mean value of the background and the vertical bar is the standard error on the mean. In the bottom figures, each point represents a single measurement.

Only the top RPC will be studied henceforth. Appendix B has the background frequency for all active pads as a function of date.

6.3.2 SECONDARY PARTICLES DETECTED BY THE RPC

The main file with the contents of the detection of particles using RPCs at TdF will now be analyzed.

In the previous section the number of active pads in the top RPC was shown to be 48. Figure 6.10, which is the distribution of multiplicities, shows a local peak for the bin of 13 particles. This peak is not explained by the physics of cosmic rays nor is it a saturation peak, as is the peak for 48 particles in the same distribution. The saturation peak has contributions from cosmic ray events that will generate 48 particles that will be detected at TdF's top RPC but also from events that will generate more than those 48 particles.

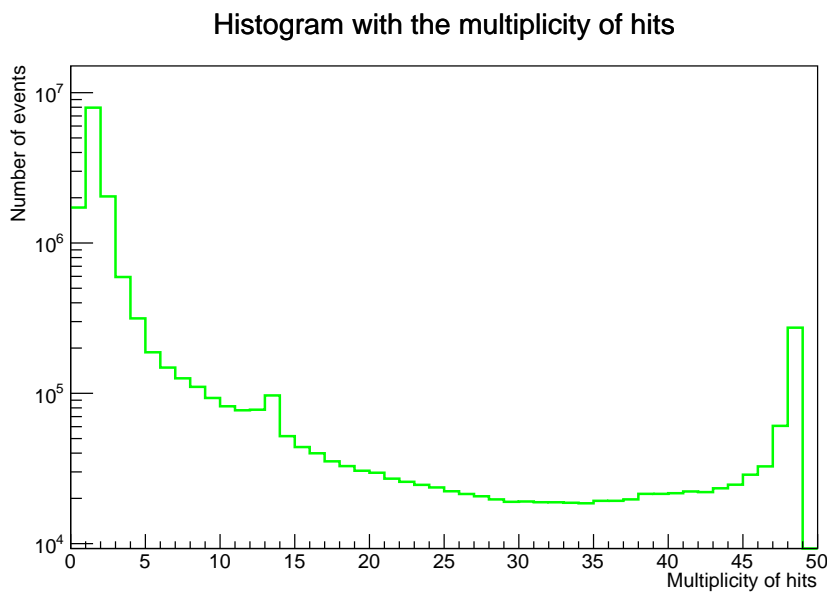


Figure 6.10 – Distribution of the number of particles considering active pads (9 through 56) for the top RPC.

In order to understand the peak for the 13th bin in figure 6.10, an histogram with the pairs of pad numbers showing cross-talk effects for a multiplicity of 13 was drawn. Figure 6.11 shows that. It can be seen that some bins colored as bright yellow have an unreasonable higher number of entries. Those bins correspond to pads number 9, 16, 17, 24, 25, 32, 33, 40, 41, 48, 49, 52 and 56.

Having removed those 13 pads from the analysis, there are now 35 pads being considered.

Removing those 13 pads and re-doing the distribution of the number of particles gives figure 6.13. It shows that there is no longer a peak in the 13th bin. The map of pad's position is in figure 6.12. It shows that the pads that suffer from crosstalk are the pads from the first and last line ($y \approx 0.25\text{m}$ and $y \approx 1.35\text{m}$) due to being more sensitive to environmental conditions. Conditions such as peaks of humidity affect mainly the pads in the border. In the map of pads,

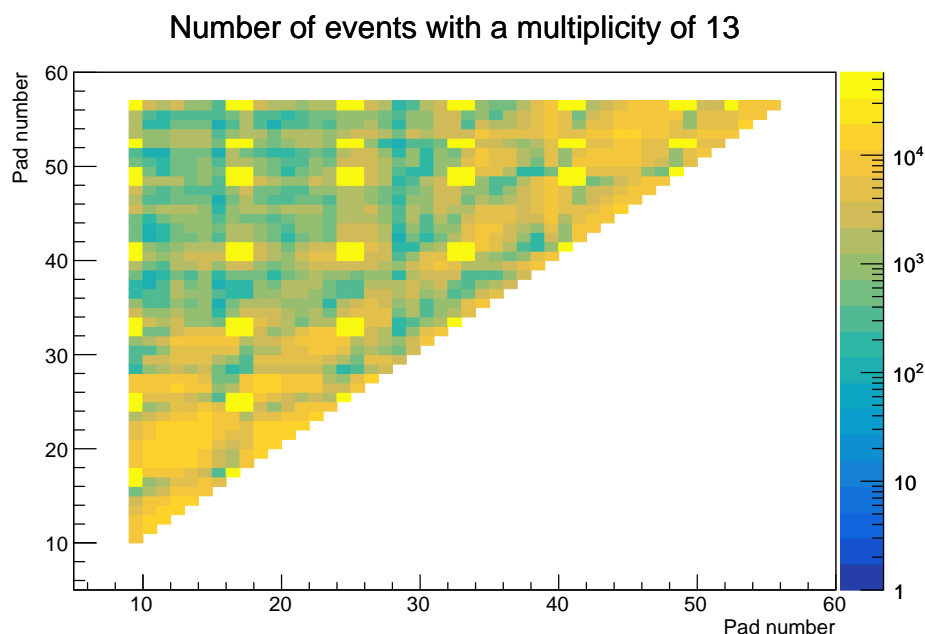


Figure 6.11 – Distribution of pairs of pad numbers showing cross-talk effects for a multiplicity of 13. As an example if a cosmic ray event triggered pads number 1, 4 and 7 (multiplicity 3), then an entry will be added to (1,4), (1,7) and (4,7).

the last column (pads 57 to 64) are also not active pads due to being *noisy* pads (high background frequency), as was already seen in the previous section.

Now that the substandard pads are defined, one can plot the rate of events as a function of time using only the 35 pads that were deemed good, which is what is done in figure 6.14. Figure 6.15 shows the rate of hits (hits per second) detected in the 35 pads as a function of date and figure 6.16 shows the average multiplicity as a function of date for the same pads. It can be seen that there is a maximum after 26/Dec/2016, also present in a pad-by-pad basis (which can be seen in appendix C).

This peak is not explained by a change of efficiency of the RPC, since, as we will see later, these changes are around 1%, which is not sufficiently large to explain it. However, in that time region, there is a humidity peak and a temperature peak, seen in figures 6.21 and 6.20, respectively. The peak is also visible in the background studies, specially in the 1st to the 8th pad of the bottom RPC, which can be seen in Appendix B.

Since the condition to write an event in the RPC file is to have a T1 condition in the tank, a change of the rate of T1 could explain both the peak and general non-constant-value seen, for example, in figure 6.16. That change of T1's rate could be due to either temperature fluctuations (which would change the quantum-efficiency of the PMTs) and/or it could be a *raining* PMT. Both of these hypothesis would change the value of 1 VEM and, hence, it would change the T1 trigger rate [76] [77]. An increase in the T1 trigger rate would give an increase in both the number of events and number of hits, which is what is seen in figures 6.14 and 6.15.

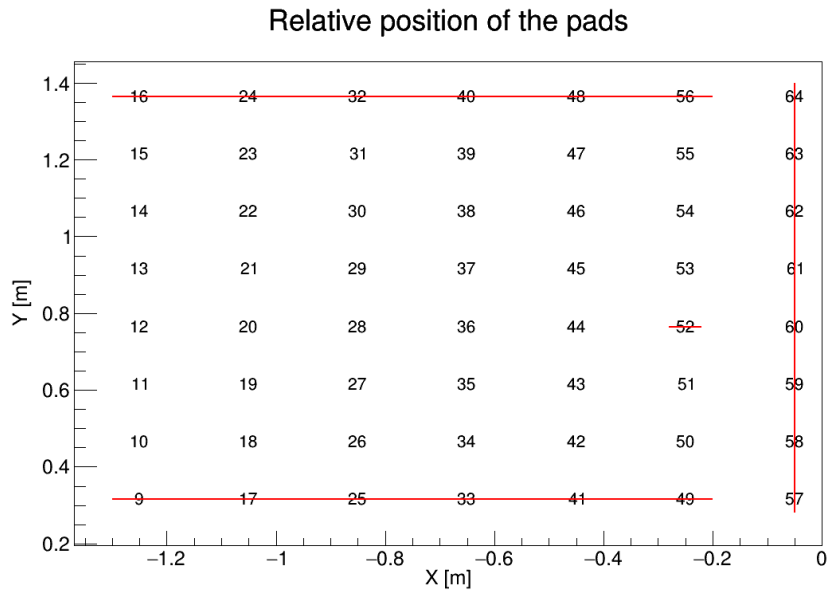


Figure 6.12 – Map of pad's positions. The pads with a red strike-through are pads that are removed from the analysis due to cross-talk effects. The numbering follows the numbering in the RPC file, for example, 17th bit of the channel's column corresponds to the pad number 17.

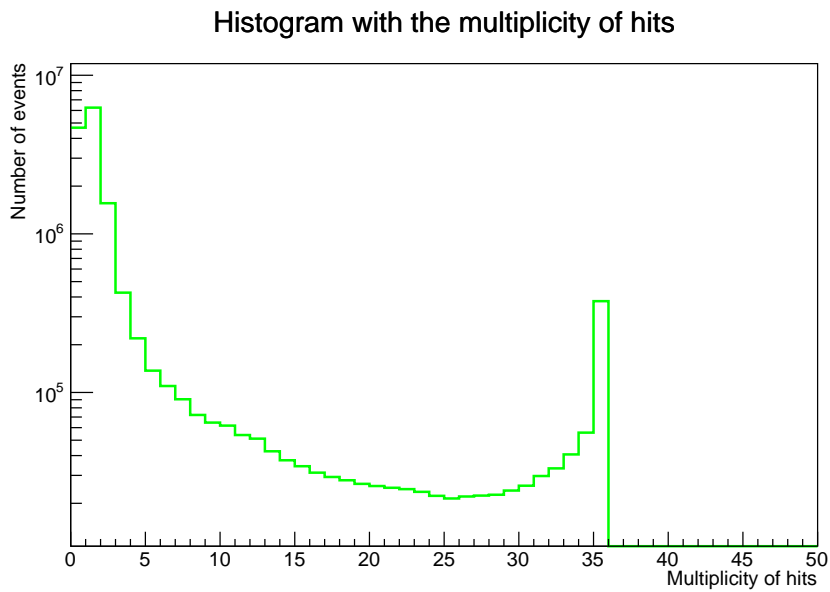


Figure 6.13 – Distribution of the number of particles considering pads 9 through 56 with the exception of the pads numbered 9, 16, 17, 24, 25, 32, 33, 40, 41, 48, 49, 52 and 56 for the top RPC.

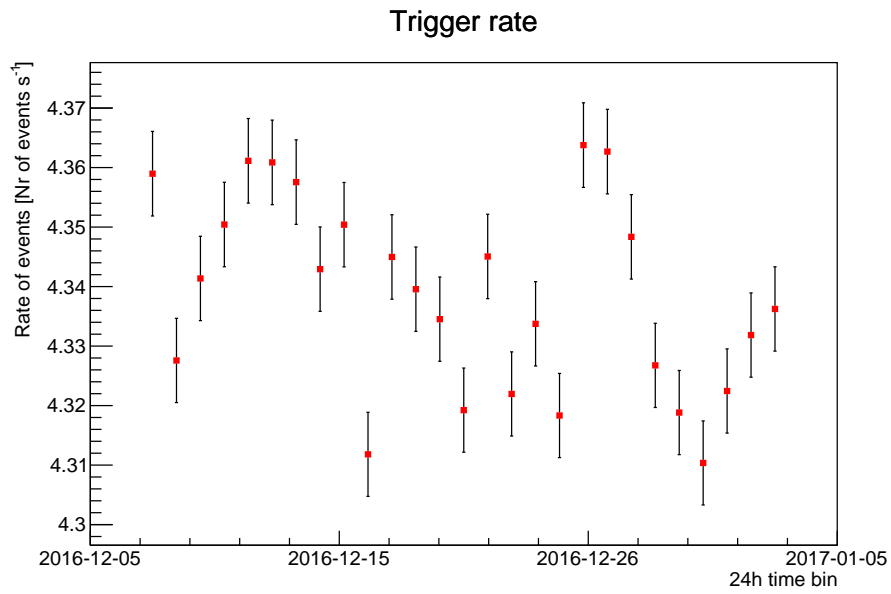


Figure 6.14 – Rate of events as a function of date for the pads that are not striked-through in figure 6.12. The X-axis are time bins with a width of 24 h and the points are centered in their respective bin. The error bars in the rate of events is \sqrt{Nr} events in bin/ Δt , where Δt is the width of the time bin, in seconds.

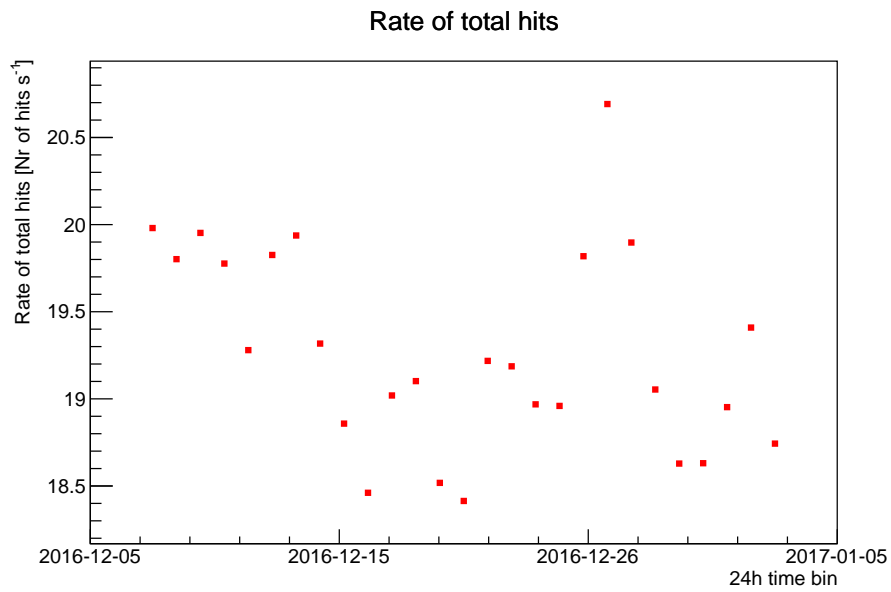


Figure 6.15 – Rate of total hits as a function of date. Only 35 pads were used for particle detection. The X-axis are time-bins with a width of 24 h and the points are centered in their respective bin. The error-bars in the flux of particles is \sqrt{Nr} particles in bin/ Δt , where Δt is the width of the time bin, in seconds.

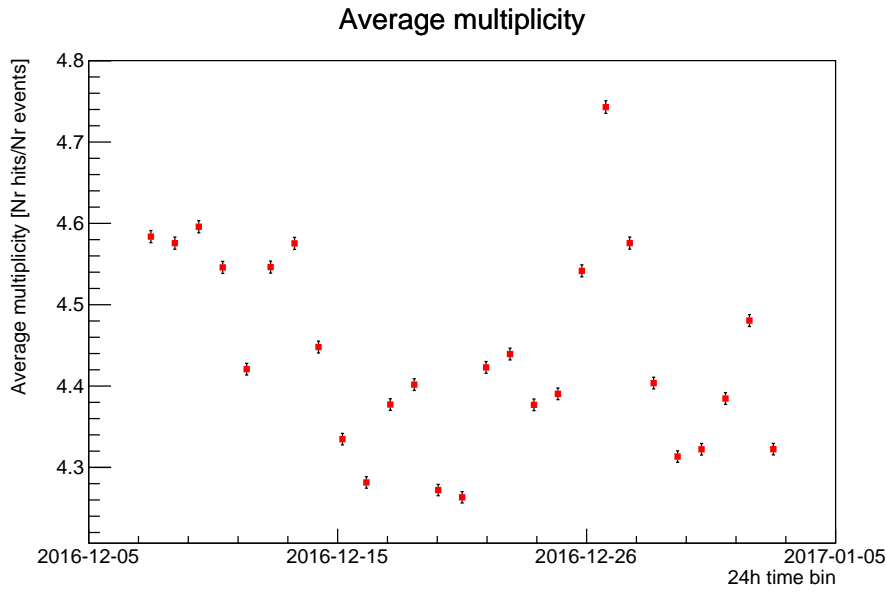


Figure 6.16 – Average multiplicity per bin as a function of date. Only 35 pads were used for particle detection. The X-axis are time-bins with a width of 24 h and the points are centered in their respective bin. The error-bars in the average multiplicity is given by $\left| \frac{1}{\text{Nr events}} \right| \times \sqrt{\text{Nr hits}} + \left| \frac{\text{Nr hits}}{\text{Nr events}^2} \right| \times \sqrt{\text{Nr events}}$.

6.3.3 DENSITY OF MUONS

This RPC file, in combination with the already analyzed T3 File allows for building an MLDF at TdF, which is the objective of this work. Knowing that the Lateral Distribution Function relates the density of particles to a core distance and that the core distance is obtained by querying the ADST files, the missing parameter is the density of particles, which can be calculated as follows:

$$\rho = \frac{\text{Number of hits}}{\text{eff} \times A} \quad (6.3.1)$$

Where eff is the efficiency of the RPC, which we will obtain in section 6.4.2, and A is the active area of the RPC. Since we are interested in muon hits, a correction for the electromagnetic component will need to be done, following the results obtained in section 5.4.

6.3.4 BRIDGE BETWEEN RPC'S DATA AND RECONSTRUCTED EVENTS

The parameter entitled *Tank ID* (LTS) relates the file with the T3 requests to TdF to the file with the RPC data. The LTS should be the same in both the T3 file and RPC file for the same event. This LTS is not ever increasing, it is periodic. Due to its periodicity, an additional parameter that exists in both files needs to be considered in order to find events in both files: timing information (date/GPS time).

A link between these two files was extensively searched but it could not be found. Events in 1 file could not be linked to events in the other file. The reason for this is still unclear. Due to this inability to relate RPC data (muon data) to the reconstructed distance to the station, a mean MLDF at TdF will not be obtained. What follows is an analysis that needs to be done regardless of having a way to relate events between the two files, namely, an analysis of the condition of the RPCs at TdF including the detection of particles, background studies and a calculation of the efficiency of the RPC.

6.4 MONITORING OF THE RPCS

A file with monitoring data for the top RPC taken every minute from 06/Dec/2016 to 04/Jan/2017 is studied here. The pressure, voltage, current, temperature (in 9 different locations of the top RPC) and relative humidity (in 2 locations) are available in order to monitor the status of the RPC. What follows is an analysis of this data.

As is clear in equation 6.3.1, the efficiency of the RPC must be known in order to compute the true density of particles. The RPC's efficiency is a function of the reduced electric field [73], given by equation 6.4.1.

$$\frac{E}{N} = 0.0138068748 \times \frac{V_{\text{eff,Volts}} (T_{\text{C}} + 273.15)}{d_{\text{cm}} P_{\text{mbar}}} [\text{Td}] \quad (6.4.1)$$

where E is the applied electric field and N is the gas numerical density. d_{cm} is the gap width, P_{mbar} is the pressure and T is the temperature. V_{eff} is the effective voltage and is given by:

$$V_{\text{eff}} = V_{\text{applied}} - R_{\text{cm}^2} I \quad (6.4.2)$$

with V_{applied} being the applied voltage, R_{cm^2} the resistance per square centimeter seen by the current and I the current drawn by the chamber. These last two quantities are given as follows:

$$R_{\text{cm}^2} = 10.5 \times 10^{12} \times 10^{\frac{20 - \langle T \rangle}{24.3}} \times \frac{t \times l}{A} \quad (6.4.3)$$

$$I = \langle I \rangle \quad (6.4.4)$$

where t is the amount of glass plates that contribute for each gap (1.5), l is the glass thickness (0.19 cm), A is the of sensitive gas area of the RPC ($120 \times 150 \text{ cm}^2$). $\rho(T) = 10.5 \times 10^{12} \times 10^{(20 - \langle T \rangle)/24.3} \Omega/\text{cm}$ is the volume resistivity. [73]

In order to calculate the efficiency for each monitoring-data entry, a parametrization of the efficiency curve as a function of the reduced electric field for the RPC used here needs to be done. Using the data points taken directly from the efficiency curve of [72], a fit is done using a sigmoid function of the form:

$$f(E/N) = a + \frac{b - a}{1 + \left(\frac{E/N}{c}\right)^d} \quad (6.4.5)$$

where a , b , c and d are fit parameters. Figure 6.17 shows both the points and fit and Table 6.3 are the values for these fit parameters.

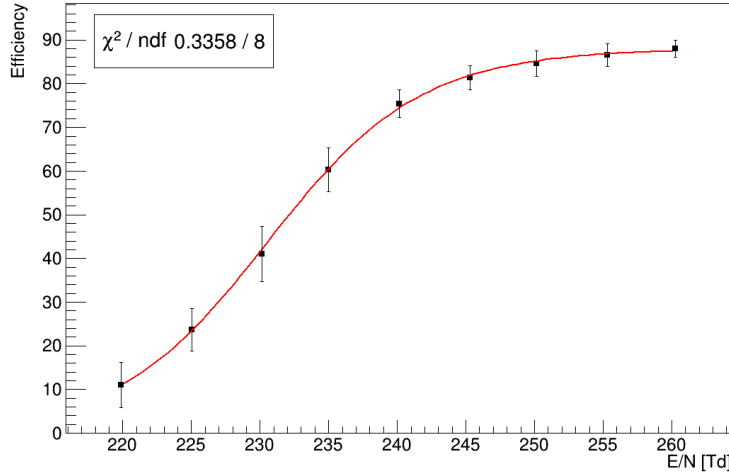


Figure 6.17 – Efficiency curve as a function of the reduced electric field. The red line is a fit using a sigmoid function given by equation 6.4.5. The fit parameters are given in table 6.3.

| Fit Parameter | a | b | c | d |
|---------------|------|-----|-------|------|
| Value | 88.0 | 1.0 | 230.7 | 42.2 |
| Uncertainty | 0.7 | 0.7 | 0.7 | 0.7 |

Table 6.3 – Parameters of the fit to the RPC's efficiency as a function of the reduced electric field, figure 6.17. The parameters are defined in equation 6.4.5.

6.4.1 DATA CLEAN-UP AND MONITORING INFORMATION

Since TdF is in an inhospitable place, a data clean-up was needed. In order for a measurement to be considered as valuable information for an efficiency calculation, it needs to pass certain criteria. An average of the current measurement and the next 9 measurements is done for the individual temperatures and individual relative humidities as well as the pressure. These three averages are referred as next-neighboring-averages (NNA) for pressure, temperature and humidity. All of the following criteria need to be met in order for the measurement to be considered as valid. Non-valid measurements are discarded. The discarded measurements represent variations in temperature, humidity or pressure that are *not real* in the sense that they must be due to read-out errors by the respective sensors.

- Eliminate measurements whose pressure are outside the range]600, 1000[mbar.
- Eliminate measurements in which at-least 1 of the 2 humidity measurements are outside the range]20, 100[%.

- Eliminate measurements in which at-least 1 individual temperature is outside the range $]10, 40[$ °C.
- Eliminate measurements where the absolute value of the difference between the current pressure and NNA-pressure is larger than 1.5 mbar. 1.5 mbar is given as 10 % of the daily pressure variation, which is roughly 15 mbar.
- Eliminate measurements where the absolute value of the difference between the humidity and NNA-humidity is larger than 1%. 1% is given as 10 % of the daily relative humidity variation, which is roughly 10%. This is done for each one of 2 available measurements of humidity.
- Eliminate measurements where the absolute value of the difference between temperature and NNA-temperature is larger than 0.5 °C. 0.5 °C is given as 10 % of the daily temperature variation, which is roughly 5°C. This is done for each one of the 9 available measurements of temperature.

These cuts reduced 43200 measurements to 32882. The average voltage, average current, average temperature and average relative humidity are in figure 6.18, 6.19, 6.20 and 6.21, respectively. They are given by $\langle V \rangle = (V^+ - V^-)/2$, $\langle I \rangle = (I^+ + I^-)/2$, $\langle T \rangle = \sum_i T_i/9$ and $\langle H \rangle = (H_1 + H_2)/2$. The individual voltage, current, temperature and humidity as a function of time can be seen in appendix D.

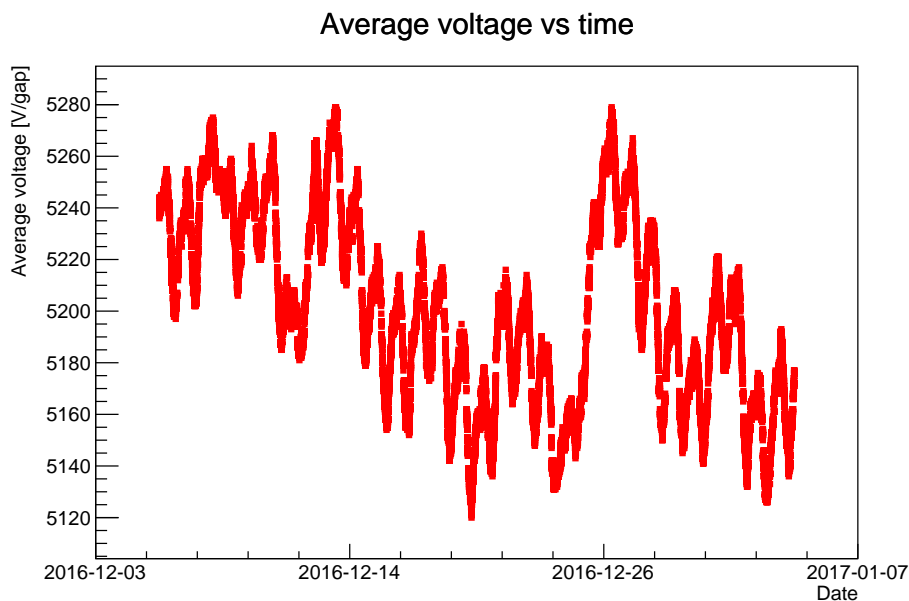


Figure 6.18 – Average voltage for the top RPC as a function of acquisition date.

Pressure is also directly measured with a sensor located in the top RPC and it is shown in figure 6.22.

Figure 6.18 shows a variation in the average voltage that compensates changes in the temperature seen in figure 6.20. This is to maintain a nearly constant efficiency. The average relative

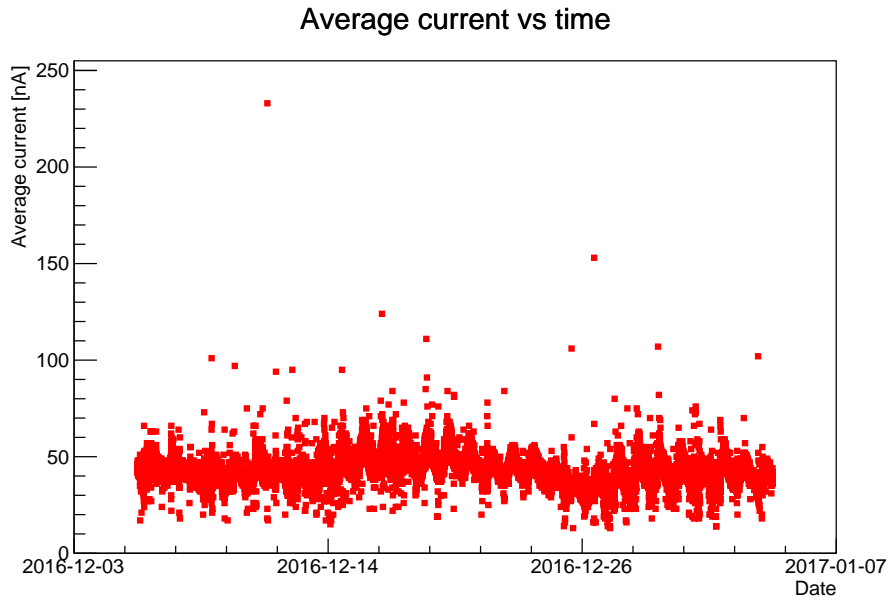


Figure 6.19 – Average current for the top RPC as a function of acquisition date.

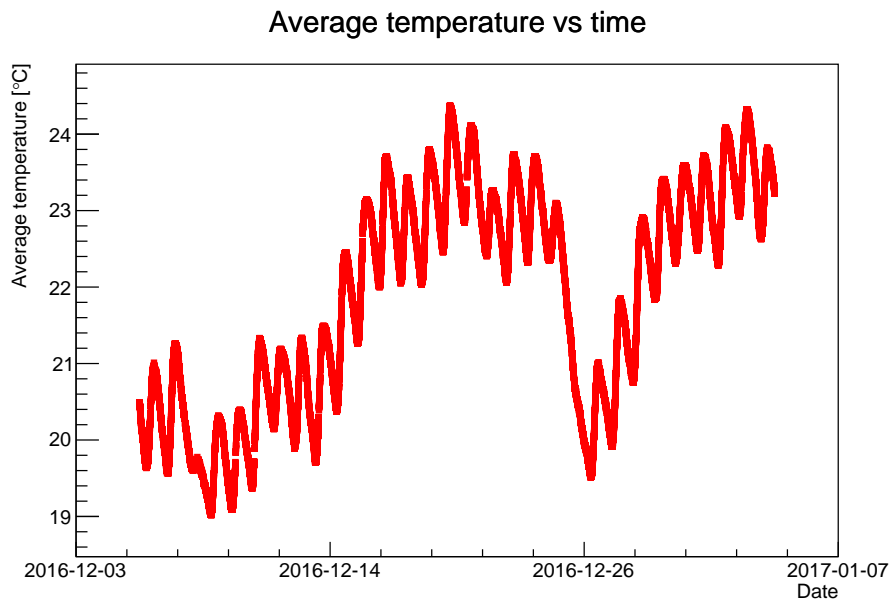


Figure 6.20 – Average temperature for the top RPC as a function of acquisition date.

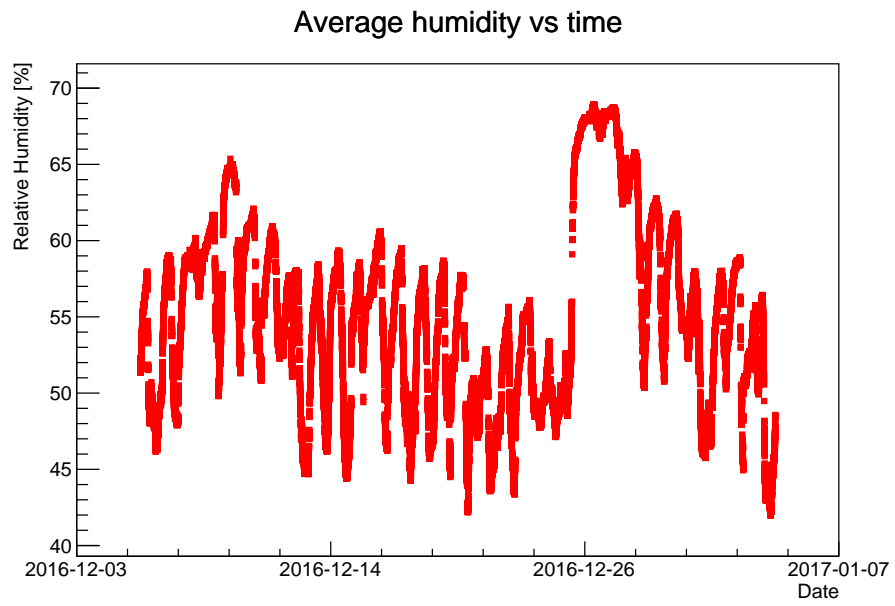


Figure 6.21 – Average relative humidity for the top RPC as a function of acquisition date.

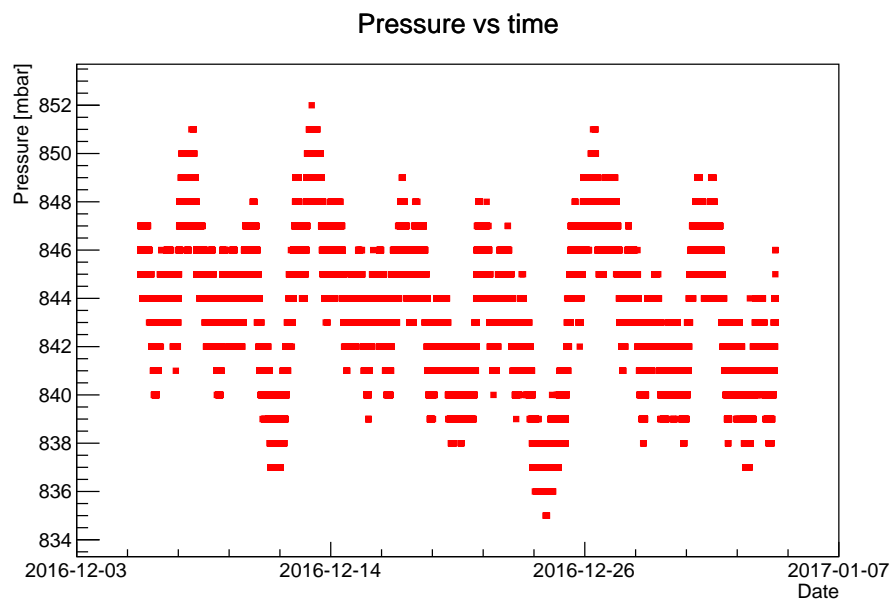


Figure 6.22 – Pressure for the top RPC as a function of acquisition date.

humidity in figure 6.21 shows a peak after 2016-12-26 that may create cross-talk effects, which could help explain the peak in that time period seen in the rate of total hits, figure 6.15. Figure 6.20 also shows a temperature peak in that date.

6.4.2 EFFICIENCY CALCULATION

Given the variables directly obtained by the sensors, which were graphed in the previous section, and using equation 6.4.1 and the parametrization of the efficiency curve given by 6.4.5 it is now possible to obtain an estimated efficiency curve for the acquisition time and physical conditions here studied.

Figure 6.23 is the $R_{cm^2}I$. The effective voltage (V_{eff}) as a function of time is in figure 6.24 and the obtained reduced electric field in figure 6.25. V_{eff} is essentially the applied voltage minus a small contribution of voltage lost by the RPC's sheet's resistance: $R_{cm^2}I$.

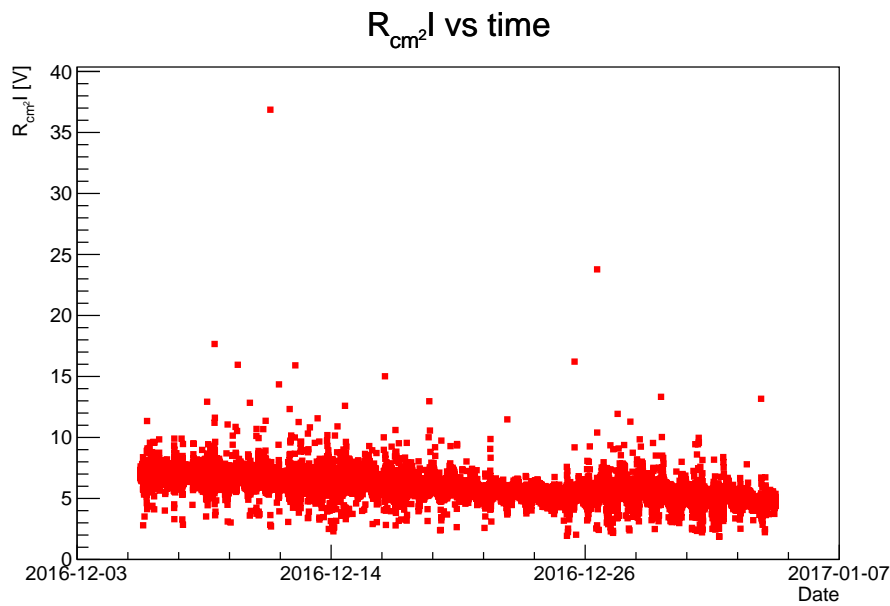


Figure 6.23 – $R_{cm^2}I$ for the top RPC as a function of acquisition date. $R_{cm^2}I$ was calculated using equations 6.4.3 and 6.4.4

The efficiency of the top RPC between 06/Dec/2016 and 04/Jan/2017 is shown in figure 6.26 and as a function of the reduced electric field in figure 6.27. Both these figures show that the efficiency is very stable with values approximately between 84.8% and 86% over the 1-month of measurements studied here. Figure 6.24 shows that V_{eff} counter-acts fluctuations in both temperature (figure 6.20) and pressure (figure 6.22), guaranteeing a steady value of efficiency over time.

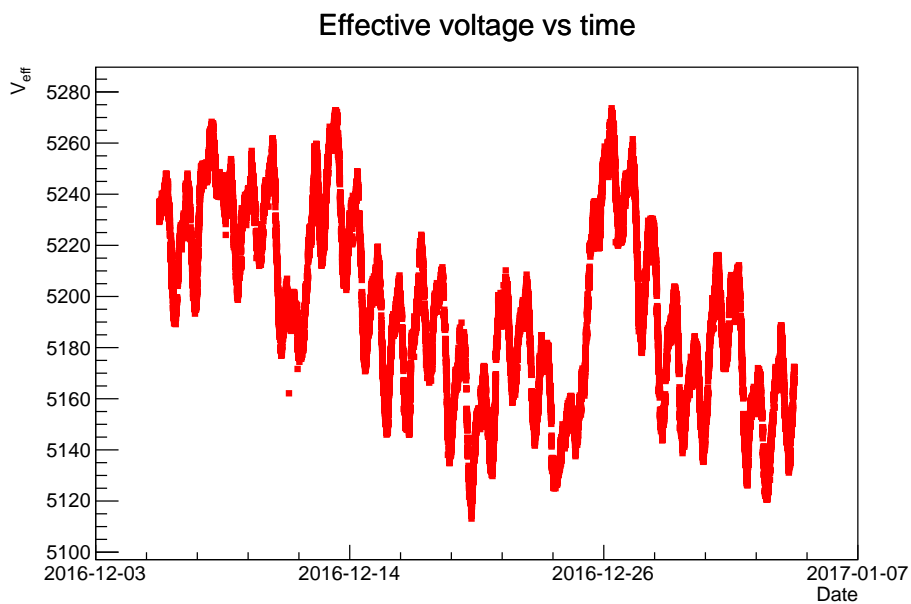


Figure 6.24 – Effective voltage for the top RPC as a function of acquisition date. V_{eff} was calculated using equation 6.4.2.

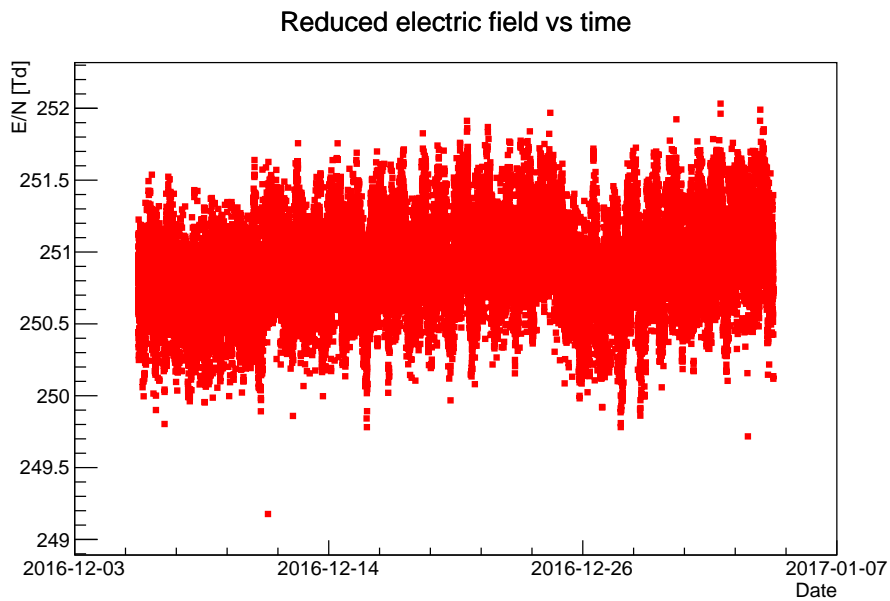


Figure 6.25 – Reduced electric field for the top RPC as a function of acquisition date. E/N was calculated using equation 6.4.1.

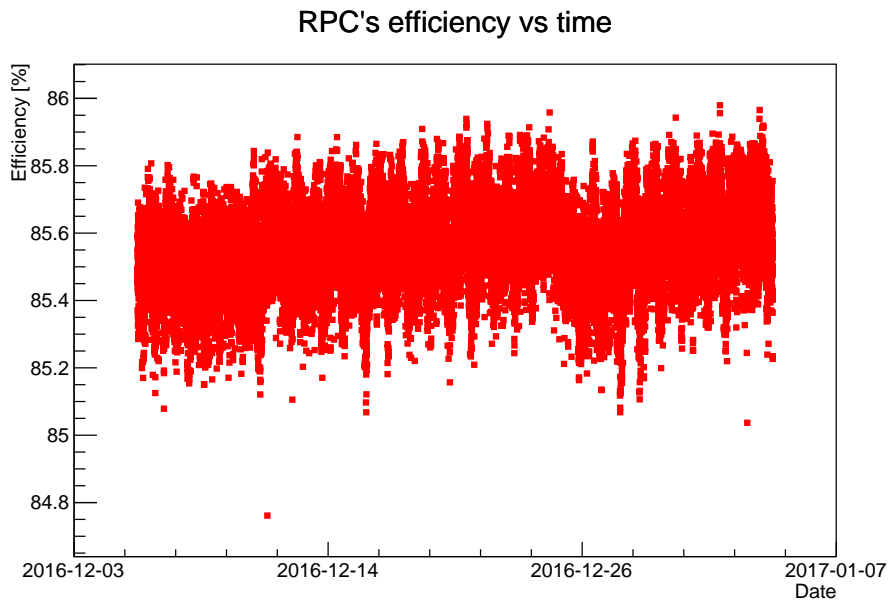


Figure 6.26 – Efficiency for the top RPC as a function of acquisition date. The efficiency was calculated using the parametrization given by equation 6.4.5.

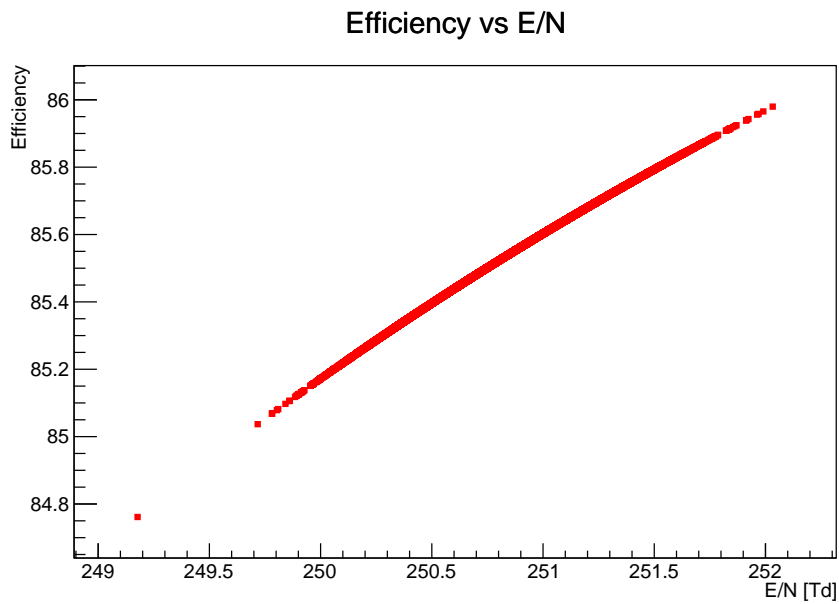


Figure 6.27 – Efficiency for the top RPC as a function of the reduced electric field. The efficiency was calculated using the parametrization given by equation 6.4.5 and the reduced electric field using equation 6.4.1.

7 CONCLUSION

The field of cosmic rays is still quite new, barely 100 years old. It has, however, already given plenty of contributions to the general particle physics community, such as the discovery of the positron and the muon. In cosmic rays, the open-questions are plenty and interesting. The universe itself is at study, from the smallest to the largest.

The energy range is large, over 13 orders of magnitude. There are some structures in the energy spectrum, characterized by a change of the spectral index, that are not fully understood, though there is a general agreement to their causes. The nature of the cosmic rays is also still debatable with the Auger observatory upgrading their detectors to address this question of the mass composition. The source and acceleration mechanisms of UHECRs is also a targeted phenomena, with a recent result by the Pierre Auger Collaboration finding an extra-galactic origin for these particles.

Several experiments have analyzed the "muon puzzle", an apparent excess of muons of data over simulations. The Pierre Auger Collaboration found an excess of muons up to 80% for hybrid events with a zenith angle larger than 60° . Telescope Array and IceTop also measured a muon excess for the outer parts of the shower while EAS-MSU and IceTop found no excess for distances closer to the shower axis. This suggests that the current understanding of the air-shower development is deficient in regards to the hadronic interactions and in need of both experimental and theoretical studies to fully understand the origin of the muon puzzle.

This thesis' objective was to obtain an average muon LDF with the use of a test non-standard experimental setup. This experimental setup consisted in using two RPCs below a WCD. In order to obtain the average MLDF, the muon density for each event, measured by the top RPC, would need to be validated with ADST files in order to obtain the respective distance to the shower axis. This bridge proved to not be possible and, unfortunately, the average MLDF was not done. However, all the analysis up until that point was, and, once the bridge is possible, the MLDF should be easily and rapidly obtained. Figure 7.1 is a scheme of structure of the thesis.

A Monte-Carlo tool was built using a parametrization of an MLDF with full CORSIKA simulations and the Heitler model. We found that an increase in the number of pads of the top RPC is important to reduce the uncertainty in the fit parameters of the MLDF. We also studied the EM contamination for 4 primaries and found that only at around 700 m from the shower axis the ratio of average EM hits to average muon hits was about 20%. Further studies are needed to accurately remove the EM hits in the total RPC hits. The rate of atmospheric muons in MARTA's RPCs is negligible.

In section 6 we found that only approximately 2% of the events that had a T3 request to TdF were being saved to the data file. The reason for this is still unknown. Only 93 events were reconstructed. Since this is the number of events that would be used to obtain the average MLDF,

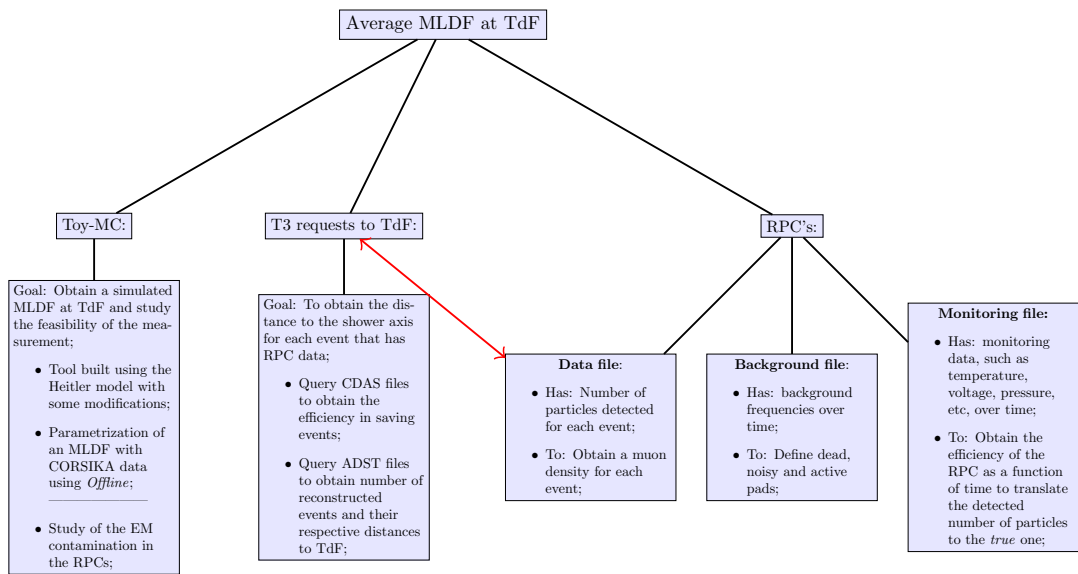


Figure 7.1 – Mind-map of the thesis. The arrow in red represents a bridge that could not be done.

it is of uttermost importance to increase it. The fraction of saved events to the data file, 2%, needs to be increased to be able to reconstruct an MLDF using data obtained over a 1-month period.

The monitoring of the RPCs proved that they are in good conditions with a constant and high efficiency, around 85%. The background studies of the top RPC showed that 8 pads were too noisy and needed to be removed from the analysis.

The main data obtained by the RPC, the particle hits, showed that 13 pads were suffering from cross-talk effects, which raised the effective number of hits. They needed to be removed from the analysis. The trigger rate and the rate of total hits showed a peak that is coincident with a humidity and temperature peak. The best hypothesis for that peak is a change of the T1 rate of the tank, since that is a condition for saving RPC data.

A DISTANCE TO THE SHOWER AXIS

The 3D distance (core distance) is the minimum distance between a point (the detector) and an axis (shower axis). Defining the detector position as $X_0 = (u, v, w)$, the position where the primary particle hits the ground as $X_1 = (a, b, c)$ and $X_2 = (a + \sin \theta \cos \phi, b + \sin \theta \sin \phi, c + \cos \theta)$ being a point in the shower axis. θ is the zenith angle and ϕ is the azimuth angle.

The distance is found by using

$$\vec{d} = \frac{|(X_0 - X_1) \times (X_0 - X_2)|}{|X_2 - X_1|} \quad (\text{A.0.1})$$

We have that:

$$\begin{aligned} (X_0 - X_1) &= (u - a, v - b, w - c) \\ (X_0 - X_2) &= (u - a - \sin \theta \cos \phi, v - b - \sin \theta \sin \phi, w - c - \cos \theta) \\ (X_2 - X_1) &= (\sin \theta \cos \phi, \sin \theta \sin \phi, \cos \phi) \text{ with } |X_2 - X_1| = 1 \end{aligned} \quad (\text{A.0.2})$$

The distance is thus:

$$\begin{aligned} d = & \left[(b - v)^2 \cos^2 \theta + (w - c)^2 (\sin \theta \sin \phi)^2 + 2(b - v)(w - c) \cos \theta \sin \theta \sin \phi + \right. \\ & (u - a)^2 \cos^2 \theta + (c - w)^2 \sin^2 \theta \cos^2 \phi + 2(u - a)(c - w) \cos \theta \sin \theta \cos \phi + \\ & \left. (a - u)^2 \sin^2 \theta \sin^2 \phi + (v - b)^2 \sin^2 \theta \cos^2 \phi + 2(a - u)(v - b) \sin^2 \theta \sin \phi \cos \phi \right]^{1/2} \end{aligned} \quad (\text{A.0.3})$$

Considering that the z component of the ground position of the event is 0: $(a, b, c) = (a, b, 0)$ and that the detector's position is $(u, v, w) = (0, 0, 0)$, the distance simplifies:

$$d = \left[(a^2 + b^2) \cos^2 \theta + \sin^2 \theta (a^2 \sin^2 \phi + b^2 \cos^2 \phi) - 2ab \sin^2 \theta \cos \phi \sin \phi \right]^{1/2} \quad (\text{A.0.4})$$

which is the same as equation 5.3.1 in section 5.

B RPC'S BACKGROUND DATA

Figures B.1 through B.9 shows the number of particles as a function of time for each viable pad. Pads 1 through 8th and from the 73rd to th 80th are pads from the bottom RPC. All the others are pads from the top RPC.

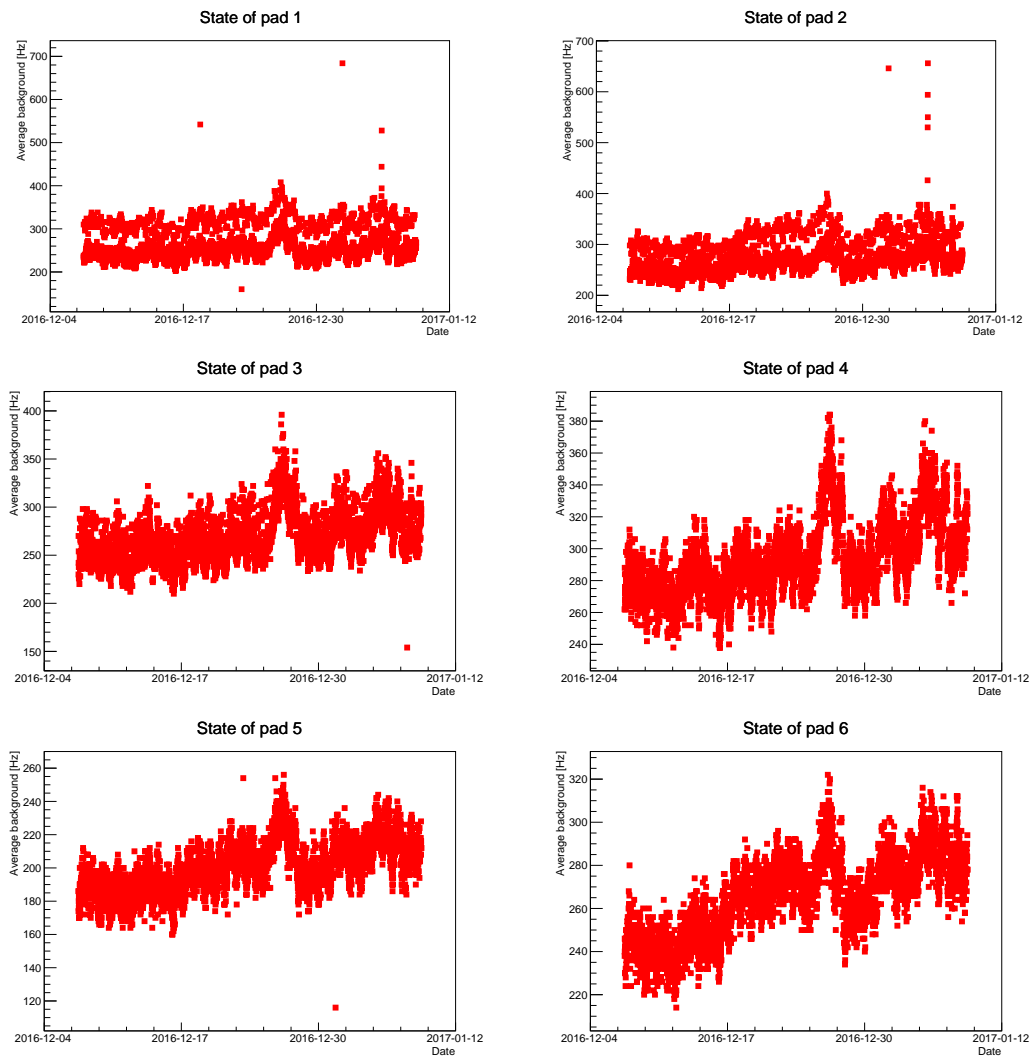


Figure B.1 – Number of particles as a function of date for each pad, from the 1st to the 6th pad. These pads are part of the bottom RPC.

B RPC's Background Data

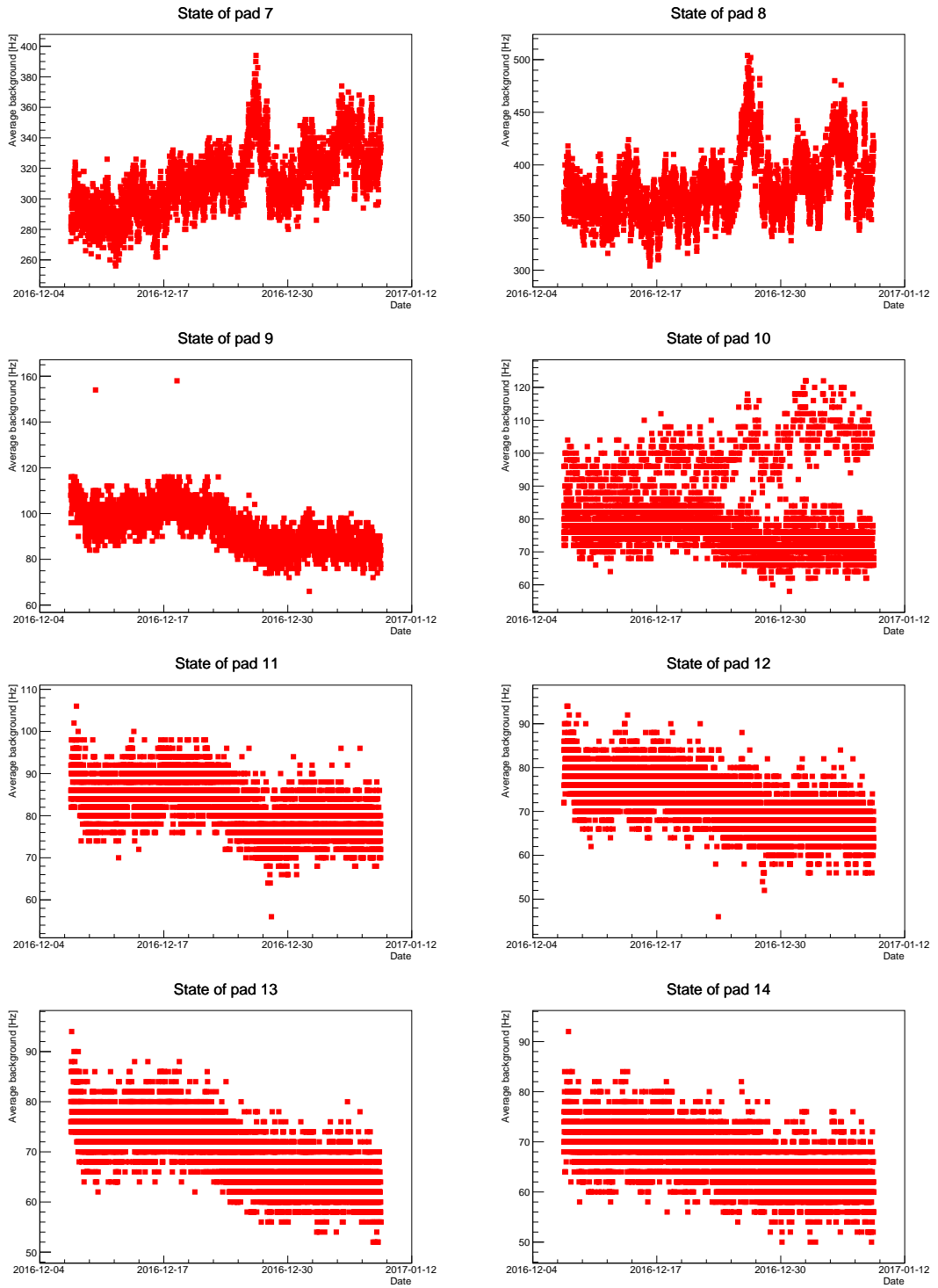


Figure B.2 – Number of particles as a function of date for each pad, from the 7th to the 14th pad. The 7th and 8th pad are part of the bottom RPC.

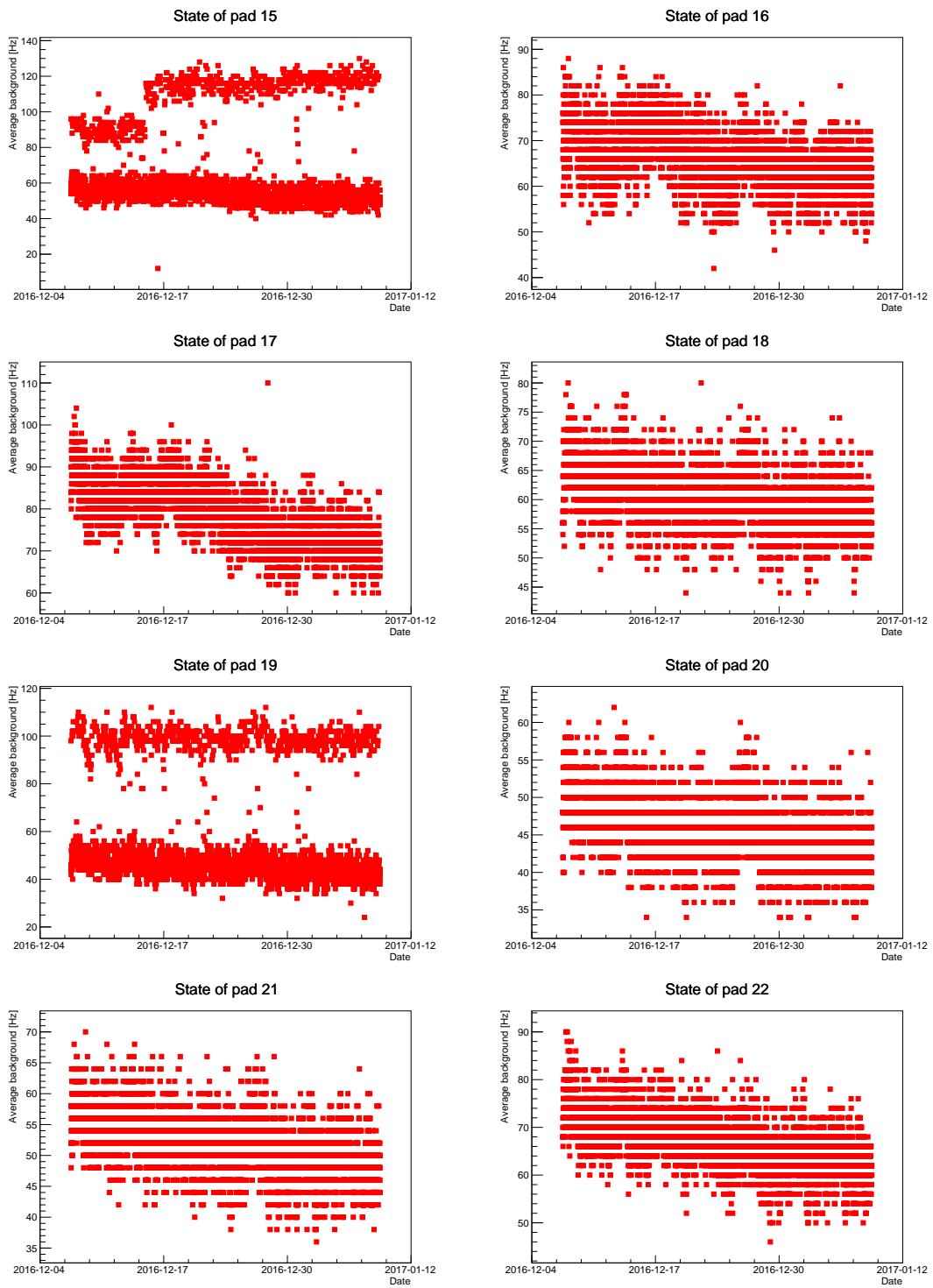


Figure B.3 – Number of particles as a function of date for each pad, from the 15th to the 22nd pad.

B RPC's Background Data

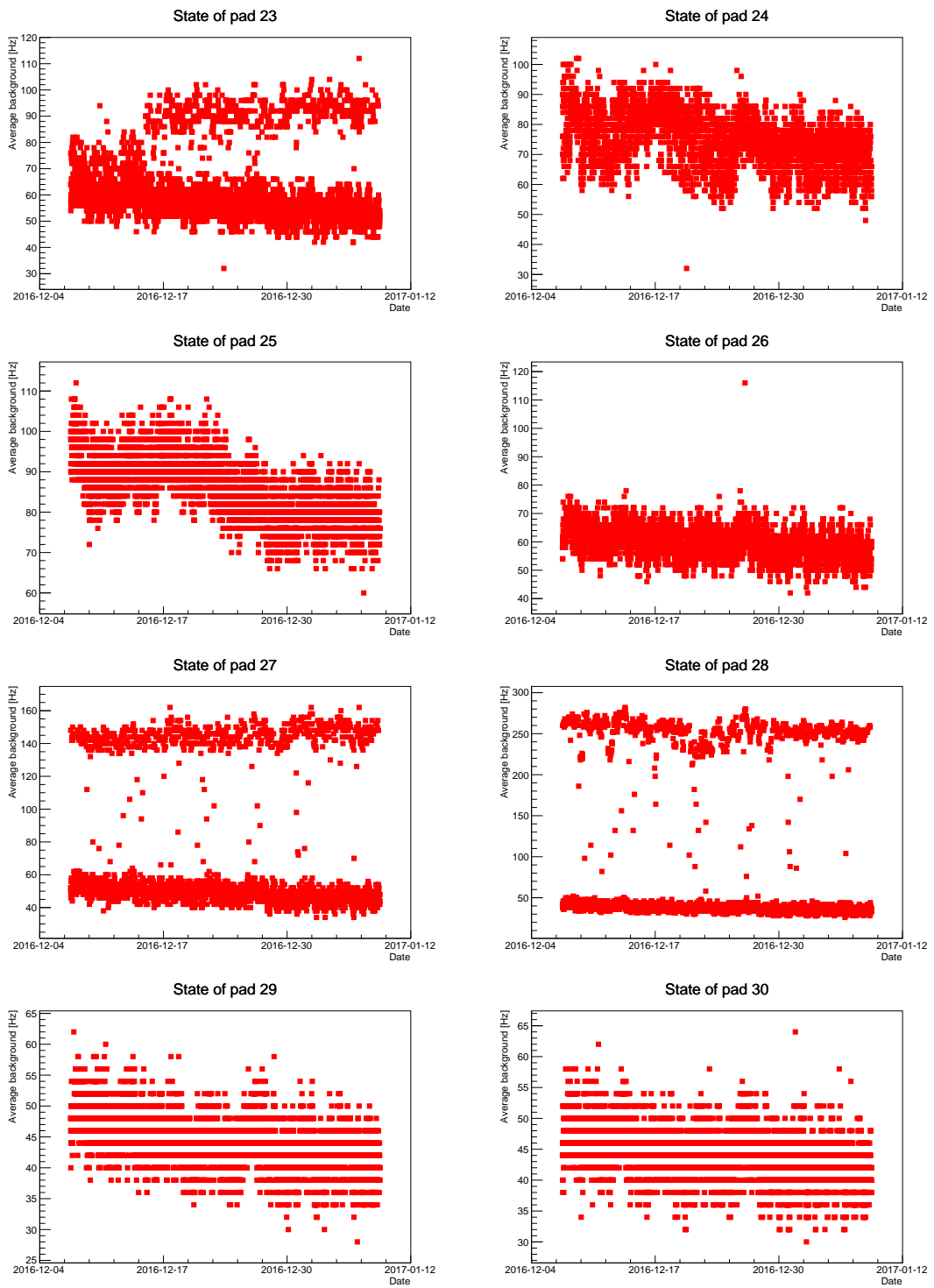


Figure B.4 – Number of particles as a function of date for each pad, from the 23rd to the 30th pad.

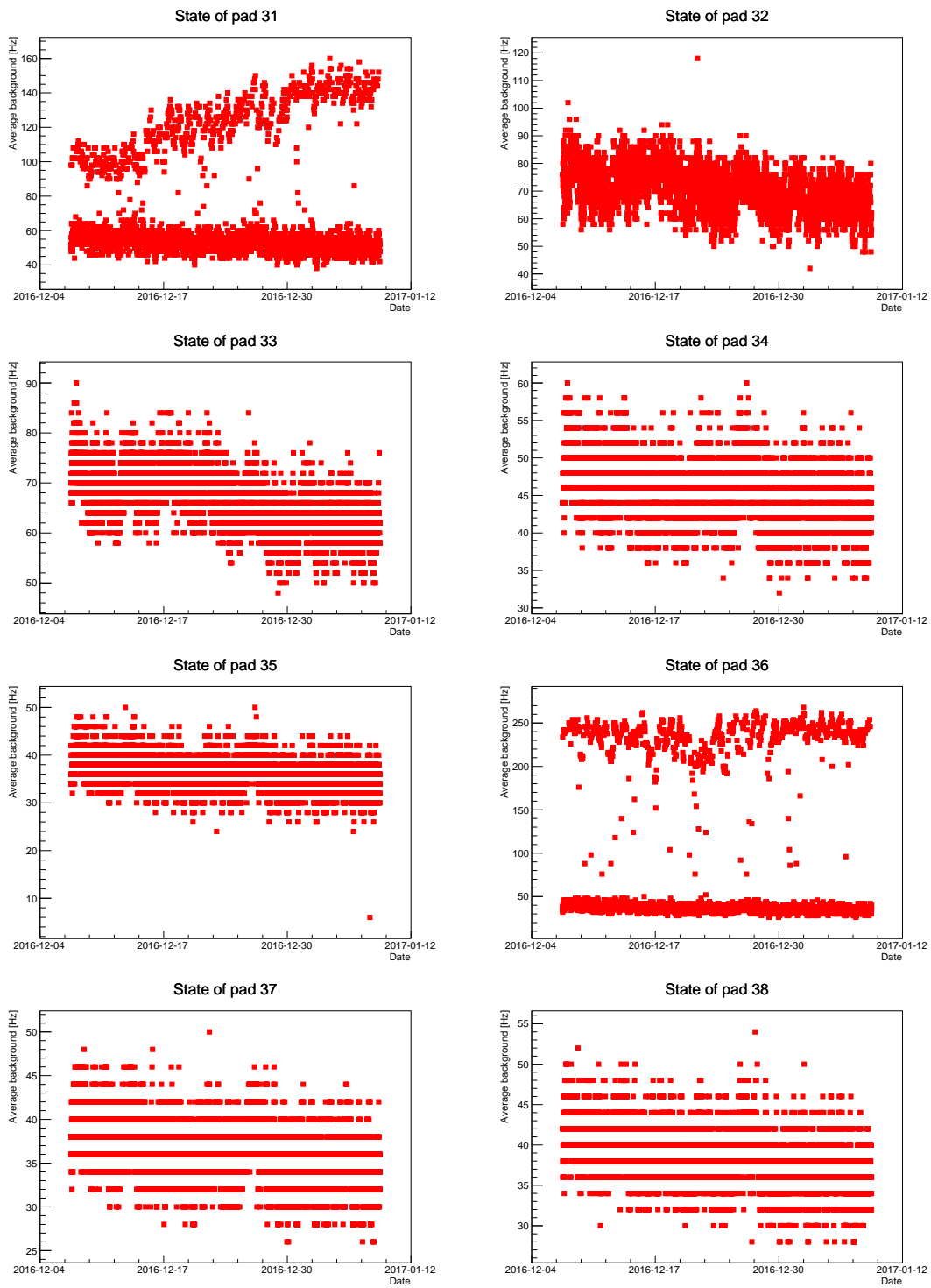


Figure B.5 – Number of particles as a function of date for each pad, from the 31st to the 38th pad.

B RPC's Background Data

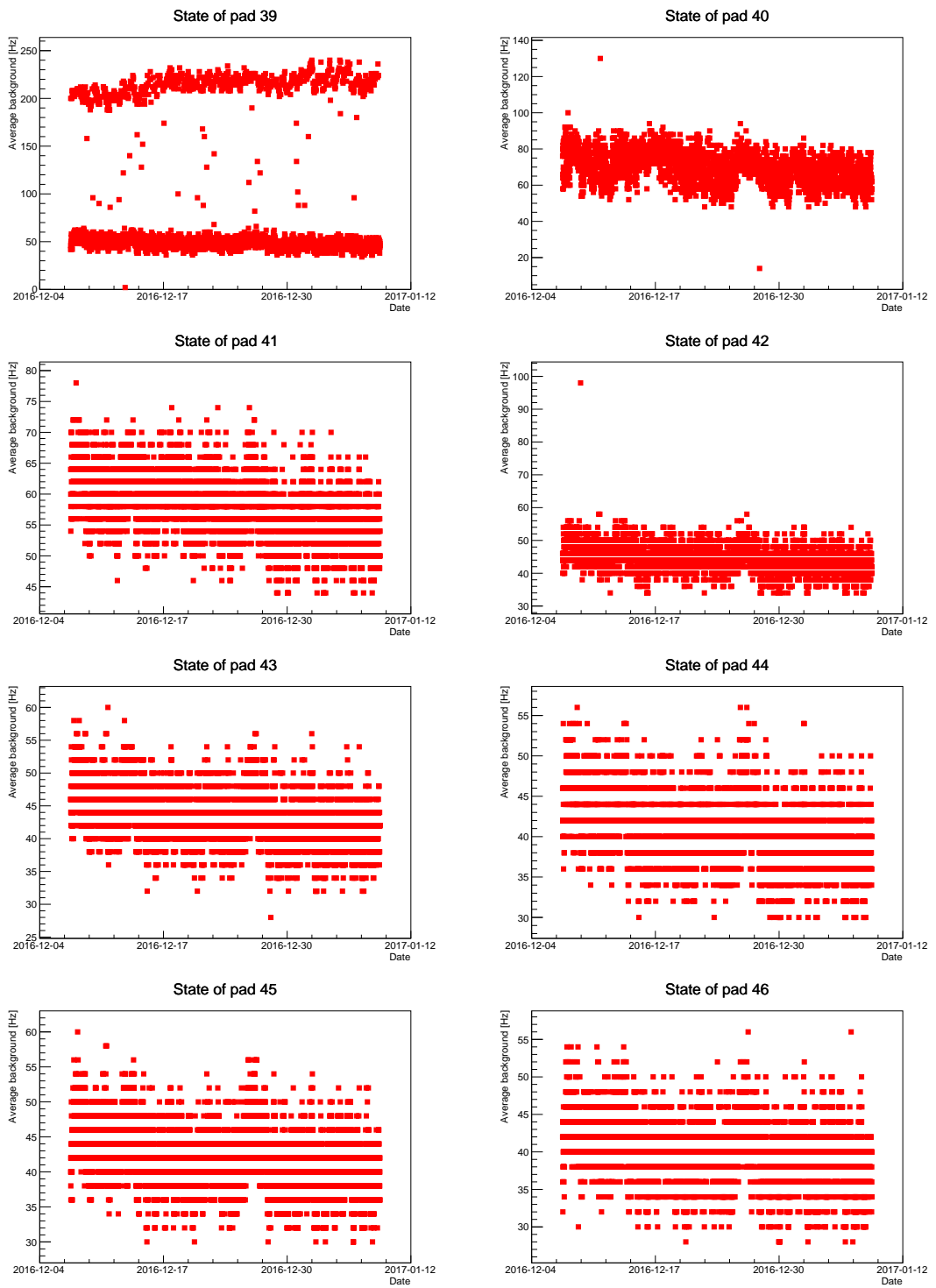


Figure B.6 – Number of particles as a function of date for each pad, from the 39th to the 46th pad.

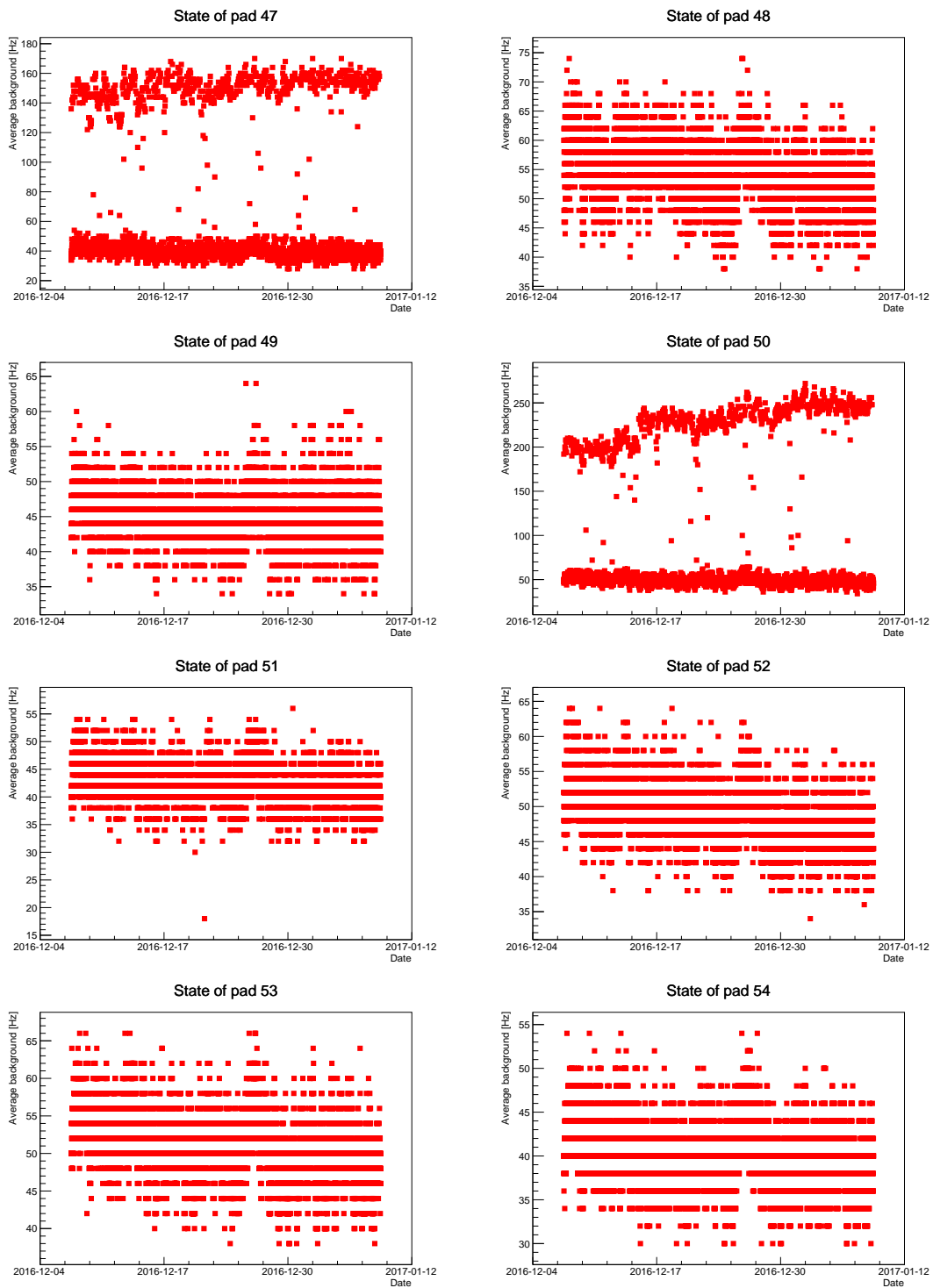


Figure B.7 – Number of particles as a function of date for each pad, from the 47th to the 54th pad.

B RPC's Background Data

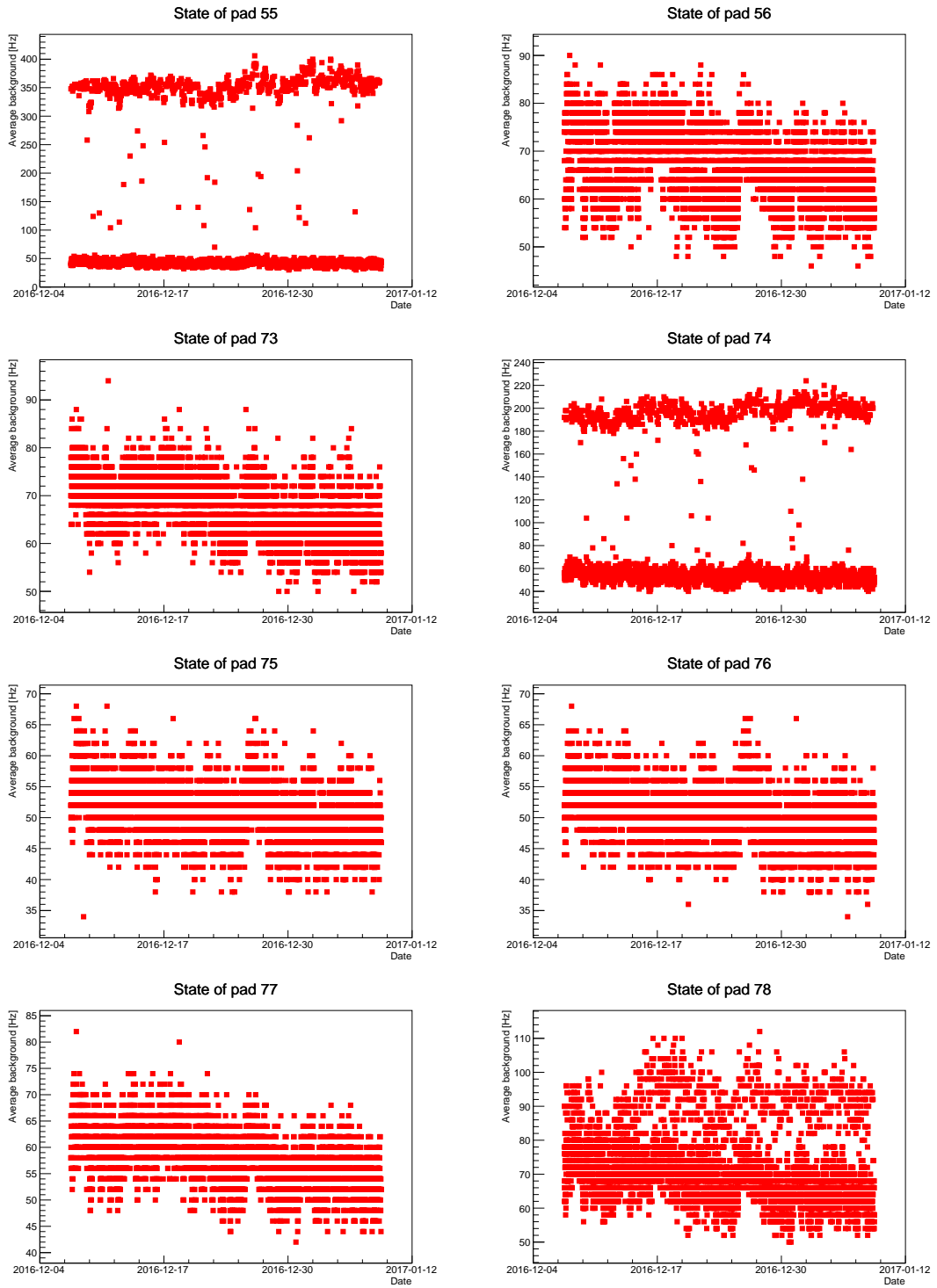


Figure B.8 – Number of particles as a function of date for each pad, from the 73rd to the 78th pad as well as the 55th and 56th. The 73rd through the 78th are pads from the bottom RPC.

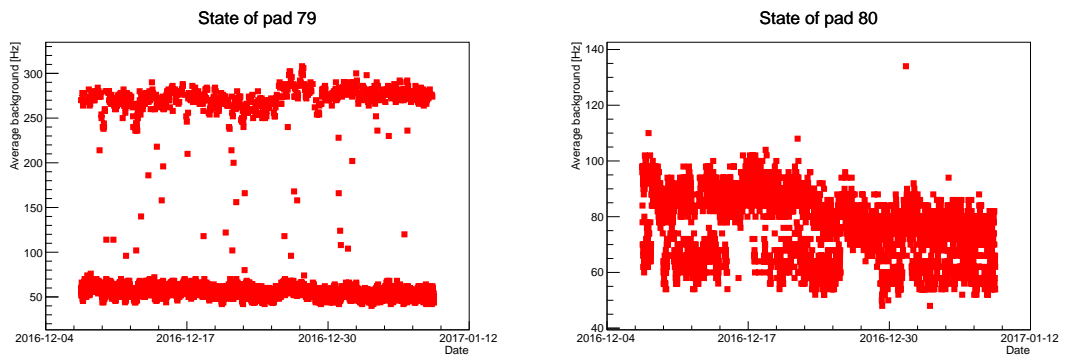


Figure B.9 – Number of particles as a function of date for pads 79th and 80th, which are pads from the bottom RPC.

C RPC'S DATA

Figures C.1 through C.5 shows the number of particles as a function of time for each viable pad.

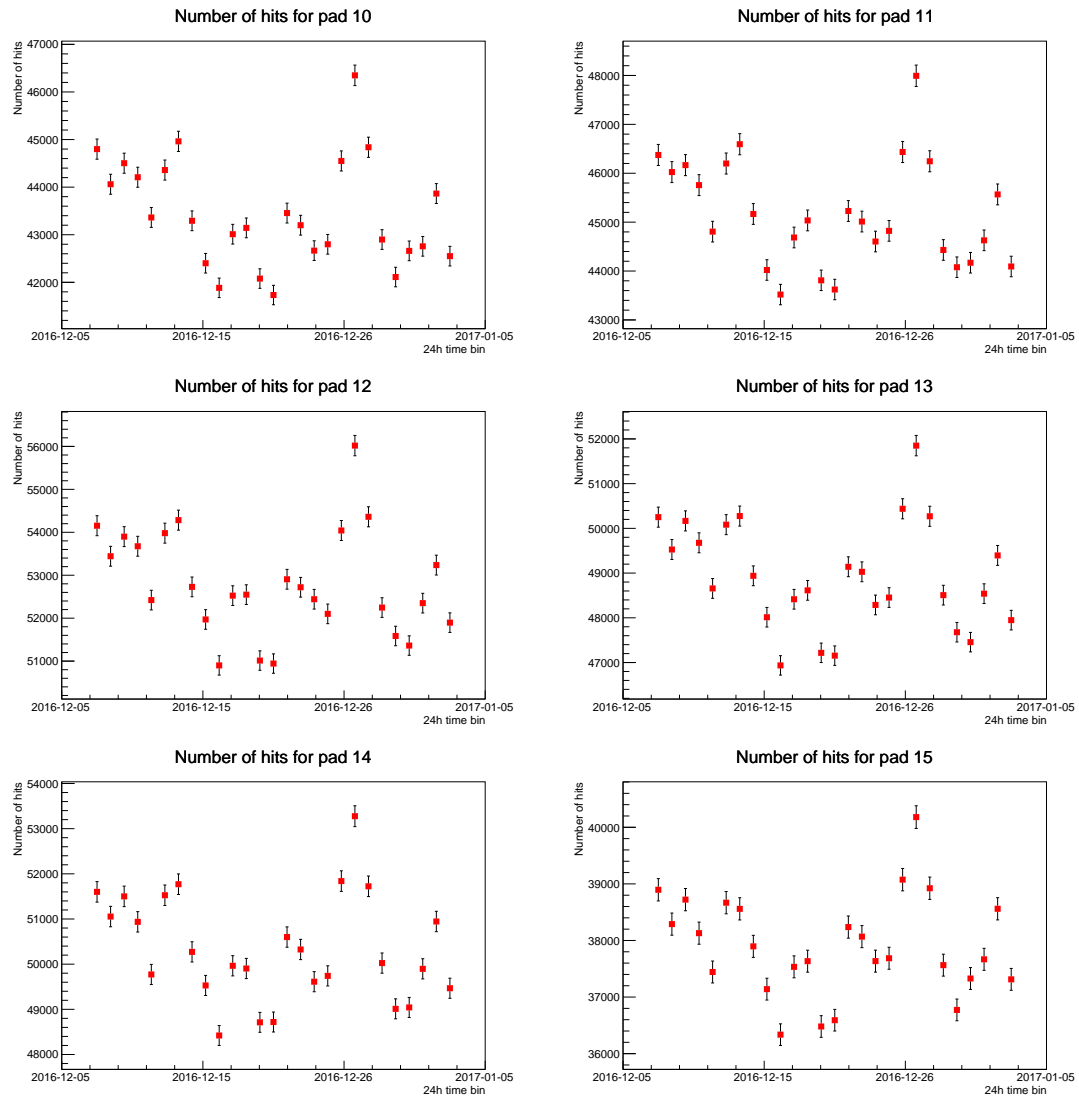


Figure C.1 – Number of particles as a function of date for each pad, from the 10th to the 15th pad.

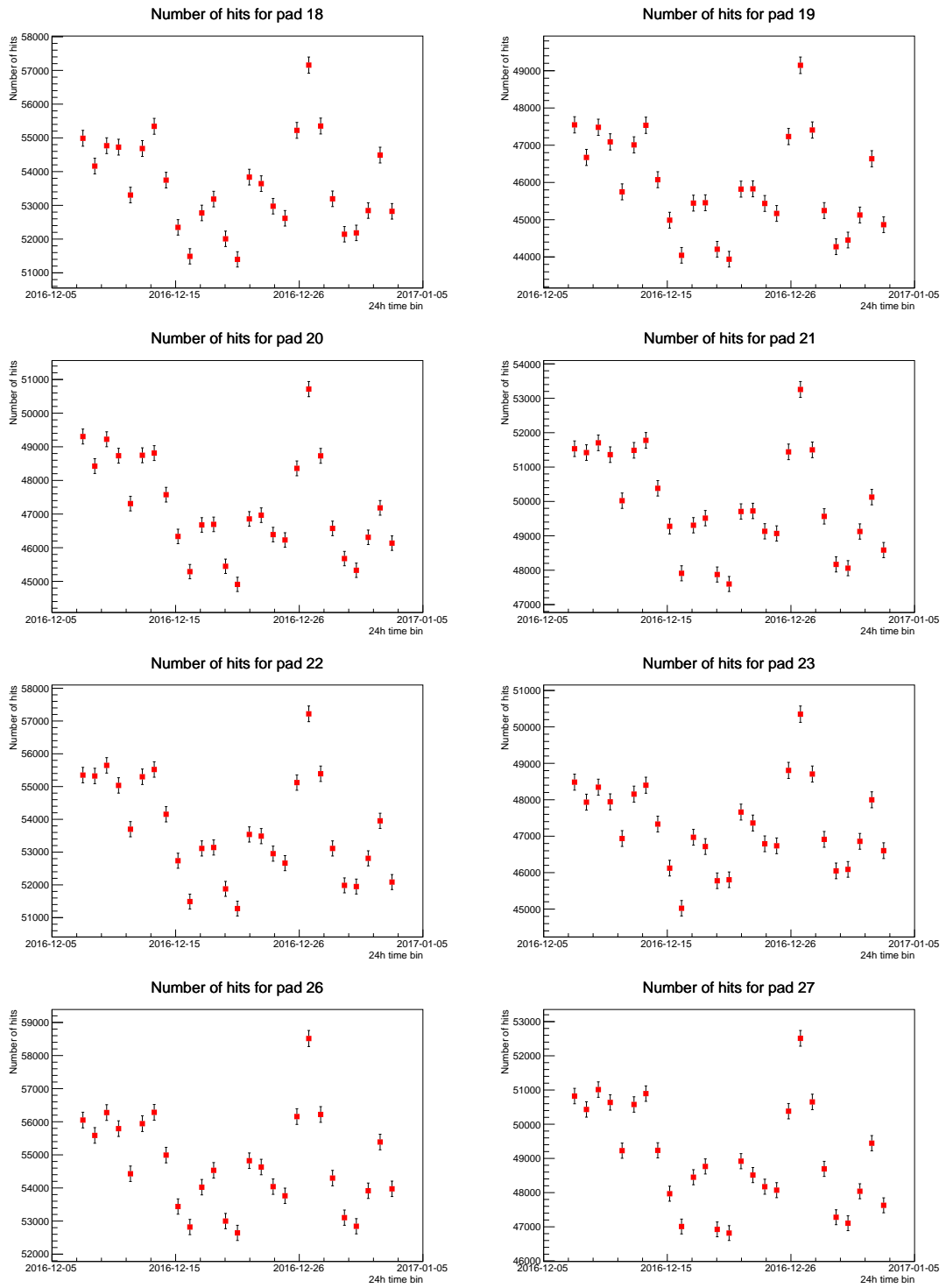


Figure C.2 – Number of particles as a function of date for each pad, from the 18th to the 27th pad with the 24th and 25th pads as an exception.

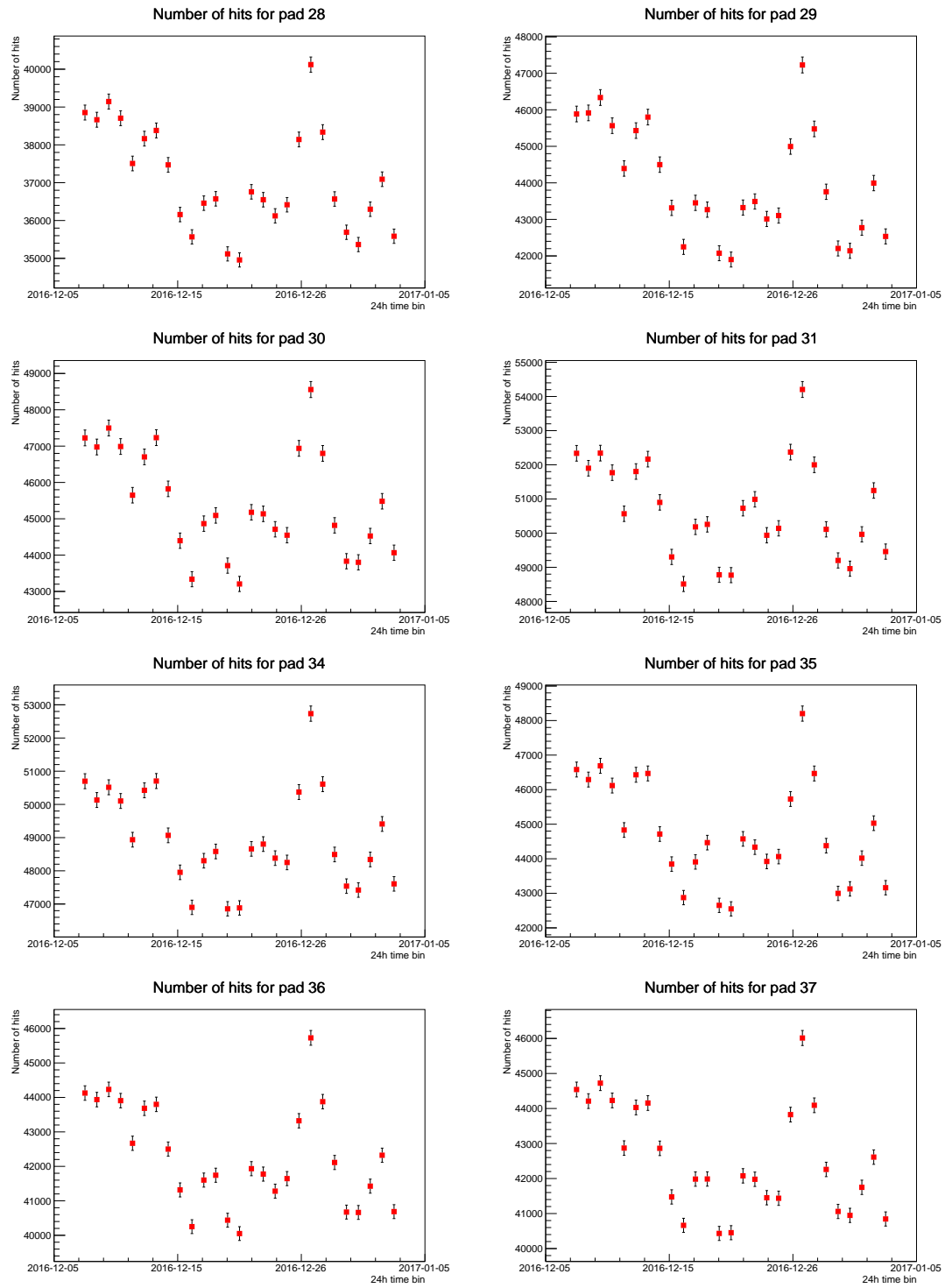


Figure C.3 – Number of particles as a function of date for each pad, from the 28th to the 37th pad with the 32nd and 33rd pads as an exception.

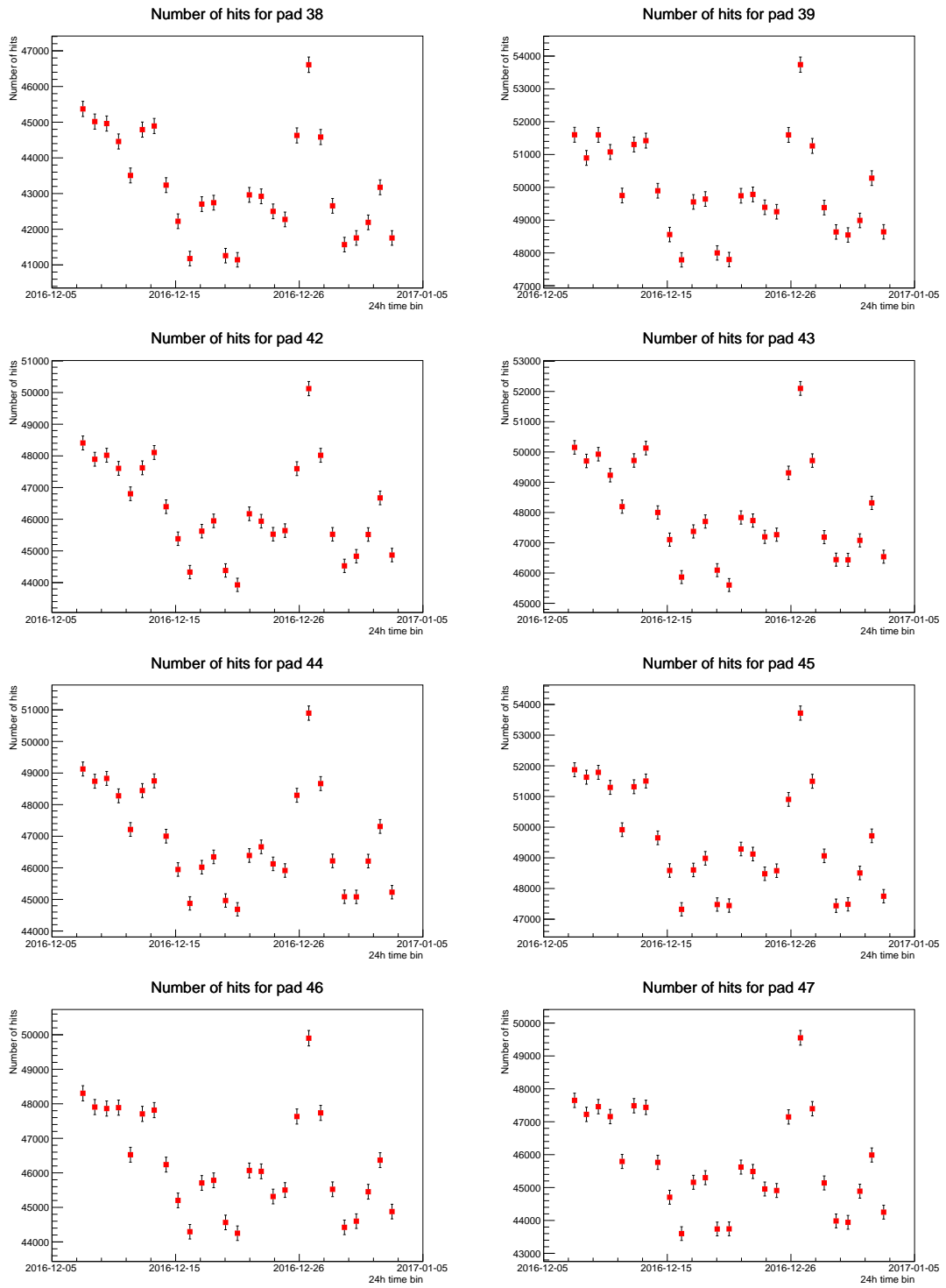


Figure C.4 – Number of particles as a function of date for each pad, from the 38th to the 47th pad with the 40th and 41st pads as an exception.

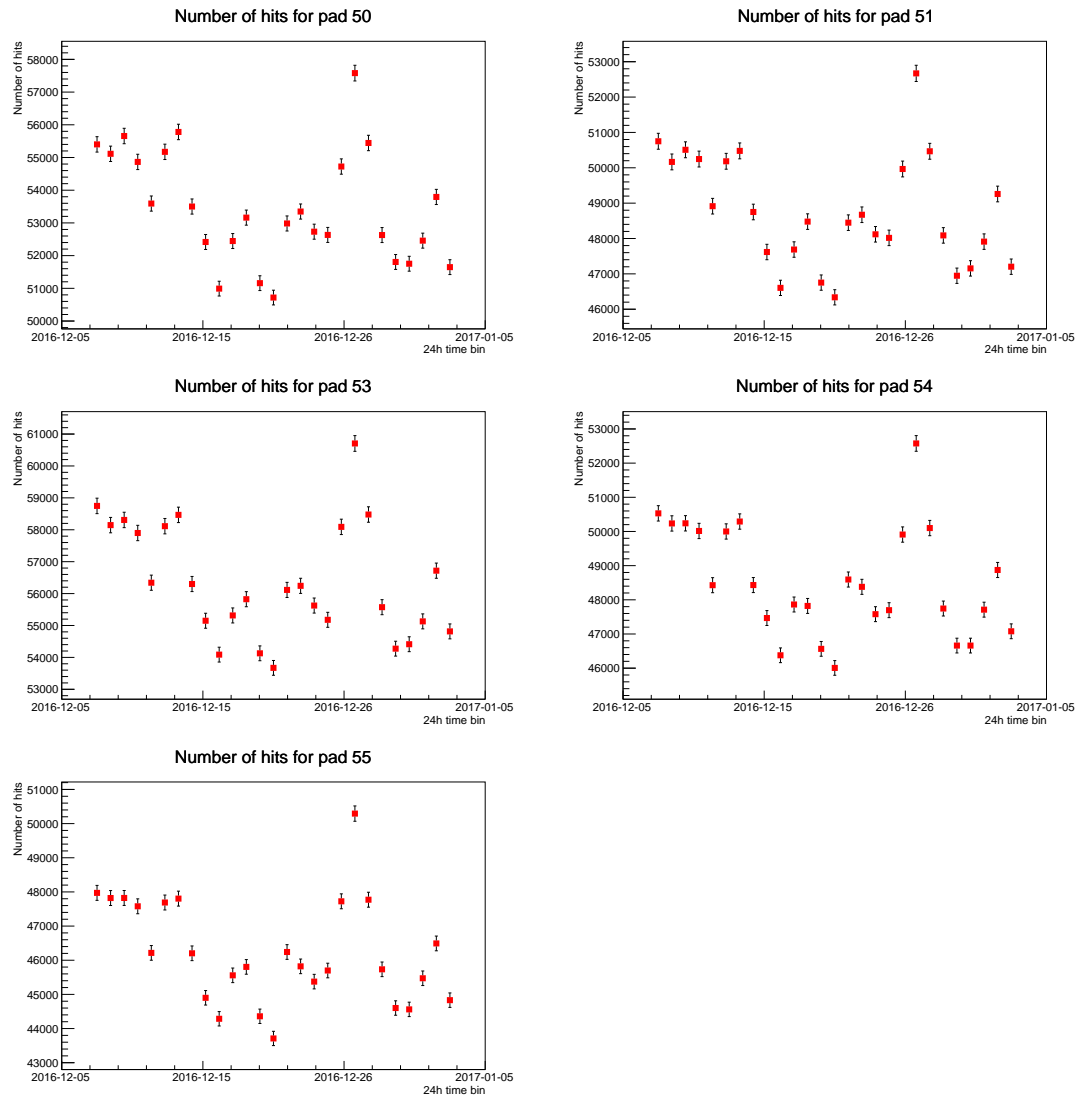


Figure C.5 – Number of particles as a function of date for each pad, from the 50th to the 55th pad with the 52nd pad as an exception.

D RPC'S MONITORING DATA

The graphics for the individual temperatures are in figure D.1 and for the positive/negative current and voltage as well as humidity obtained by two different sensors are in figure D.2.

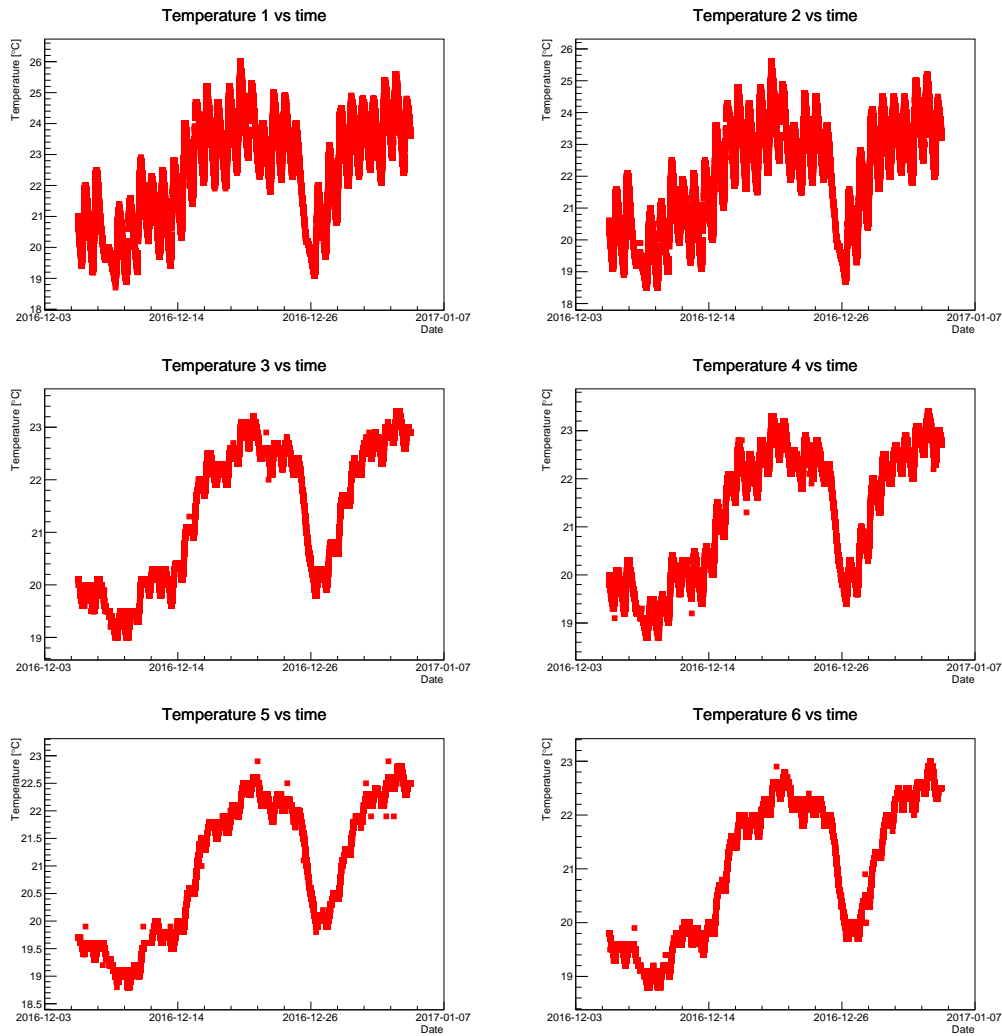


Figure D.1 – Individual temperatures as a function of date of measurement. These figures are post data-clean-up explained in section 6.4.1.

D RPC's Monitoring Data

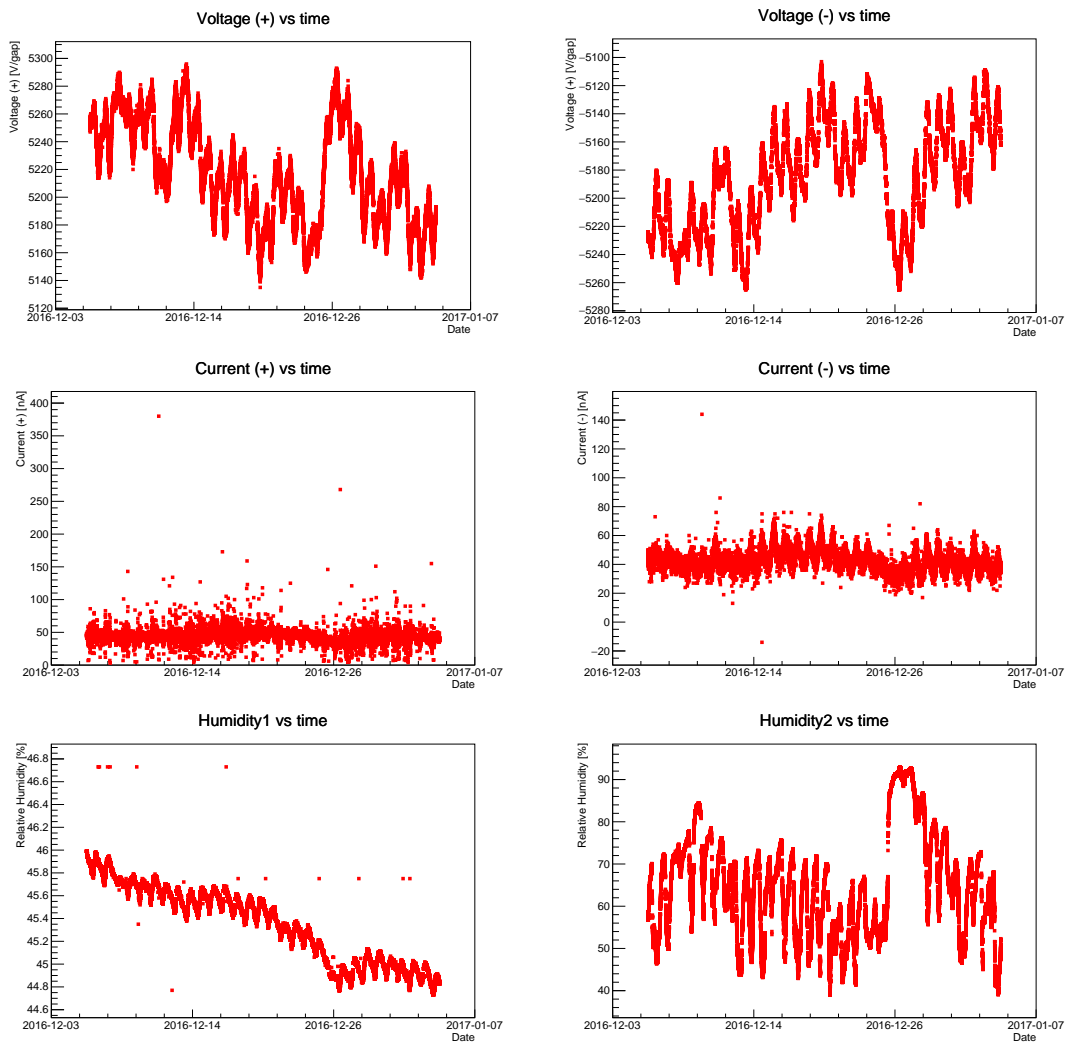


Figure D.2 – Voltage, current and average humidity as a function of date of measurement. These figures are post data-clean-up explained in section 6.4.1.

BIBLIOGRAPHY

- [1] Alessandro De Angelis and Mário João Martins Pimenta. *Introduction to Particle and Astroparticle Physics: Questions to the Universe*. Springer, 2015.
- [2] Carl D Anderson. The positive electron. *Physical Review*, 43(6):491, 1933.
- [3] James W Cronin. Cosmic rays: the most energetic particles in the universe. *Reviews of Modern Physics*, 71(2):S165, 1999.
- [4] Nobel Media AB 2014. The Nobel Prize in Physics 1936, Nobelprize.org, 2018. [Online; accessed 12-February-2018].
- [5] <https://www.physics.utah.edu/~whanlon/spectrum.html>. Accessed: 2018-07-03.
- [6] T Antoni, WD Apel, AF Badea, K Bekk, A Bercuci, J Blümer, H Bozdog, IM Brancus, A Chilingarian, K Daumiller, et al. KASCADE measurements of energy spectra for elemental groups of cosmic rays: Results and open problems. *Astroparticle physics*, 24(1-2):1–25, 2005.
- [7] Francesco Fenu. The cosmic ray energy spectrum measured using the Pierre Auger Observatory The Pierre Auger energy spectrum. In *The Pierre Auger Observatory: Contributions to the 35th International Cosmic Ray Conference (ICRC 2017)*, pages 9–16, 2017.
- [8] William F Hanlon. Recent Results from the Telescope Array Project. *Nuclear and Particle Physics Proceedings*, 279:15–22, 2016.
- [9] WD Apel, JC Arteaga-Velázquez, K Bekk, M Bertaina, J Blümer, H Bozdog, IM Brancus, P Buchholz, E Cantoni, A Chiavassa, et al. Kneelike structure in the spectrum of the heavy component of cosmic rays observed with KASCADE-Grande. *Physical Review Letters*, 107(17):171104, 2011.
- [10] R Aloisio, V Berezhinsky, and A Gazizov. Transition from galactic to extragalactic cosmic rays. *Astroparticle Physics*, 39:129–143, 2012.
- [11] Pierre Auger collaboration et al. Evidence for a mixed mass composition at the ‘ankle’ in the cosmic-ray spectrum. *Physics Letters B*, 762:288–295, 2016.
- [12] Kenneth Greisen. End to the Cosmic-Ray Spectrum? *Phys. Rev. Lett.*, 16:748–750, Apr 1966.
- [13] G. T. Zatsepin and V. A. Kuz’min. Upper Limit of the Spectrum of Cosmic Rays. *Soviet Journal of Experimental and Theoretical Physics Letters*, 4:78, August 1966.
- [14] Denise Boncioli. Probing Lorentz symmetry with the Pierre Auger Observatory. 2017.
- [15] Kseniya V Ptitsyna and Sergei V Troitsky. Physical conditions in potential accelerators of ultra-high-energy cosmic rays: updated Hillas plot and radiation-loss constraints. *Physics-Uspokhi*, 53(7):691, 2010.

- [16] M Kachelriess. Lecture notes on high energy cosmic rays. *arXiv preprint arXiv:0801.4376*, 2008.
- [17] Enrico Fermi. On the origin of the cosmic radiation. *Physical Review*, 75(8):1169, 1949.
- [18] Thomas K Gaisser, Ralph Engel, and Elisa Resconi. *Cosmic rays and particle physics*. Cambridge University Press, 1990.
- [19] HJ De Vega and N Sanchez. Extreme energy cosmic rays: bottom-up vs. top-down scenarios. In *The Early Universe and the Cosmic Microwave Background: Theory and Observations*, pages 433–449. Springer, 2003.
- [20] Thomas K Gaisser and Todor Stanev. High-energy cosmic rays. *Nuclear Physics A*, 777:98–110, 2006.
- [21] Todor Stanev, Thomas K Gaisser, and Serap Tilav. High energy cosmic rays: sources and fluxes. *Nuclear Instruments and Methods in Physics Research Section A: Accelerators, Spectrometers, Detectors and Associated Equipment*, 742:42–46, 2014.
- [22] A. Aab, P. Abreu, M. Aglietta, et al. Muons in air showers at the Pierre Auger Observatory: Measurement of atmospheric production depth. *Phys. Rev. D*, 90:012012, Jul 2014.
- [23] Jose Bellido. Depth of maximum of air-shower profiles at the Pierre Auger Observatory: Measurements above $10^{17.2}$ eV and Composition Implications. In *The Pierre Auger Observatory: Contributions to the 35th International Cosmic Ray Conference (ICRC 2017)*, pages 40–47, 2017.
- [24] Diego Harari. Ultra-high energy cosmic rays. *Physics of the Dark Universe*, 4:23–30, 2014.
- [25] Pierre Auger Collaboration et al. Observation of a large-scale anisotropy in the arrival directions of cosmic rays above 8×10^{18} eV. *Science*, 357(6357):1266–1270, 2017.
- [26] A Haungs, J Blumer, B Fuchs, D Kang, S Schoo, D Wochele, J Wochele, WD Apel, JC Arteaga-Velázquez, K Bekk, et al. KCDC—The KASCADE Cosmic-ray Data Centre. In *Journal of Physics: Conference Series*, volume 632, page 012011. IOP Publishing, 2015.
- [27] Ralph Engel, Dieter Heck, and Tanguy Pierog. Extensive air showers and hadronic interactions at high energy. *Annual review of nuclear and particle science*, 61:467–489, 2011.
- [28] D Heck, J Knapp, JN Capdevielle, G Schatz, and T Thouw. Report FZKA 6019 (1998). *Forschungszentrum Karlsruhe*, 567, 1997.
- [29] K Nakamura et al. 24.1. Primary spectra.
- [30] J Matthews. A Heitler model of extensive air showers. *Astroparticle Physics*, 22(5):387–397, 2005.
- [31] Alfredo Ferrari, Paola R Sala, Alberto Fasso, and Johannes Ranft. FLUKA: A multi-particle transport code (Program version 2005). Technical report, 2005.
- [32] TT Böhlen, F Cerutti, MPW Chin, Alberto Fassò, Alfredo Ferrari, PG Ortega, Andrea Mairani, Paola R Sala, G Smirnov, and V Vlachoudis. The FLUKA code: developments and challenges for high energy and medical applications. *Nuclear data sheets*, 120:211–214, 2014.
- [33] Steffen A Bass, Mohamed Belkacem, Marcus Bleicher, Mathias Brandstetter, L Bravina, Christoph Ernst, Lars Gerland, M Hofmann, S Hofmann, Jens Konopka, et al. Microscopic

- models for ultrarelativistic heavy ion collisions. *Progress in Particle and Nuclear Physics*, 41:255–369, 1998.
- [34] Marcus Bleicher, E Zabrodin, Christian Spieles, Steffen A Bass, Christoph Ernst, Sven Soff, L Bravina, Mohamed Belkacem, Henning Weber, Horst Stöcker, et al. Relativistic hadron-hadron collisions in the ultra-relativistic quantum molecular dynamics model. *Journal of Physics G: Nuclear and Particle Physics*, 25(9):1859, 1999.
- [35] David J. Gross and Frank Wilczek. Ultraviolet Behavior of Non-Abelian Gauge Theories. *Phys. Rev. Lett.*, 30:1343–1346, Jun 1973.
- [36] H. David Politzer. Reliable Perturbative Results for Strong Interactions? *Phys. Rev. Lett.*, 30:1346–1349, Jun 1973.
- [37] Hans Joachim Drescher, M Hladik, S Ostapchenko, T Pierog, and Klaus Werner. Parton-based Gribov–Regge theory. *Physics Reports*, 350(2-4):93–289, 2001.
- [38] S Ostapchenko. QGSJET-II: physics, recent improvements, and results for air showers. In *EPJ Web of Conferences*, volume 52, page 02001. EDP Sciences, 2013.
- [39] T Pierog, Iu Karpenko, JM Katzy, E Yatsenko, and K Werner. EPOS LHC: Test of collective hadronization with data measured at the CERN Large Hadron Collider. *Physical Review C*, 92(3):034906, 2015.
- [40] Pierog, Tanguy. Modelling hadronic interactions in cosmic ray Monte Carlo generators. *EPJ Web of Conferences*, 99:09002, 2015.
- [41] David d’Enterria and Tanguy Pierog. Global properties of proton-proton collisions at $\sqrt{s} = 100$ TeV. *Journal of High Energy Physics*, 2016(8):170, 2016.
- [42] Ralf Ulrich. Extension of the measurement of the proton-air cross section with the Pierre Auger Observatory. *PoS, ICRC2015:401*, 2016.
- [43] A. M. Hillas. Two interesting techniques for Monte-Carlo simulation of very high energy hadron cascades. *International Cosmic Ray Conference*, 8:193–196, 1981.
- [44] Dieter Heck, G Schatz, J Knapp, T Thouw, and JN Capdevielle. CORSIKA: A Monte Carlo code to simulate extensive air showers. Technical report, 1998.
- [45] Pierre Auger Collaboration et al. The Pierre Auger Cosmic Ray Observatory. *Nuclear Instruments and Methods in Physics Research Section A: Accelerators, Spectrometers, Detectors and Associated Equipment*, 798:172–213, 2015.
- [46] Alexander Aab, Pedro Abreu, Marco Aglietta, Imen Al Samarai, IFM Albuquerque, Ingomar Allekotte, Alejandro Almela, J Alvarez Castillo, Jaime Alvarez-Muñiz, GA Anastasi, et al. Spectral calibration of the fluorescence telescopes of the pierre auger observatory. *Astroparticle Physics*, 95:44–56, 2017.
- [47] Z. Szadkowski. *Triggers for the Pierre Auger Observatory, the current status and plans for the future*, volume 13. 3 of *EuCARD Editorial Series on Accelerator Science and Technology*. 2012.
- [48] J Abraham, P Abreu, M Aglietta, EJ Ahn, D Allard, I Allekotte, J Allen, J Alvarez-Muñiz, M Ambrosio, L Anchordoqui, et al. Trigger and aperture of the surface detector array of the Pierre Auger Observatory. *Nuclear Instruments and Methods in Physics Research Section A: Accelerators, Spectrometers, Detectors and Associated Equipment*, 613(1):29–39, 2010.

- [49] Pierre Auger Collaboration et al. The Pierre Auger Observatory Upgrade" AugerPrime". *Preliminary Design Report*.
- [50] Darko Veberič and Markus Roth. *Offline reference manual: SD reconstruction*. Univerza v Novi Gorici, 2005.
- [51] K Kamata. K. kamata and j. nishimura, prog. theor. phys. suppl. 6, 93 (1958). *Prog. Theor. Phys. Suppl.*, 6:93, 1958.
- [52] K Greisen. The extensive air showers. *Progress in cosmic ray physics*, 3(1), 1956.
- [53] Alexander Schulz et al. The measurement of the energy spectrum of cosmic rays above 3×10^{17} eV with the Pierre Auger Observatory. *Proceedings of the 33rd ICRC, Rio de Janeiro, Brasil*, 2013.
- [54] P Abreu, S Andringa, P Assis, A Blanco, V Barbosa Martins, P Brogueira, N Carolino, L Cazon, M Cerda, G Cernicchiaro, et al. MARTA: A high-energy cosmic-ray detector concept with high-accuracy muon measurement. *arXiv preprint arXiv:1712.07685*, 2017.
- [55] R Santonico and R Cardarelli. Development of resistive plate counters. *Nuclear Instruments and Methods in physics research*, 187(2-3):377–380, 1981.
- [56] T. Abu-Zayyad, K. Belov, D. J. Bird, J. Boyer, Z. Cao, M. Catanese, G. F. Chen, R. W. Clay, C. E. Covault, J. W. Cronin, H. Y. Dai, B. R. Dawson, J. W. Elbert, B. E. Fick, L. F. Fortson, J. W. Fowler, K. G. Gibbs, M. A. K. Glasmacher, K. D. Green, Y. Ho, A. Huang, C. C. Jui, M. J. Kidd, D. B. Kieda, B. C. Knapp, S. Ko, C. G. Larsen, W. Lee, E. C. Loh, E. J. Mannel, J. Matthews, J. N. Matthews, B. J. Newport, D. F. Nitz, R. A. Ong, K. M. Simpson, J. D. Smith, D. Sinclair, P. Sokolsky, P. Sommers, C. Song, J. K. K. Tang, S. B. Thomas, J. C. van der Velde, L. R. Wiencke, C. R. Wilkinson, S. Yoshida, and X. Z. Zhang. Evidence for Changing of Cosmic Ray Composition between 10^{17} and 10^{18} eV from Multicomponent Measurements. *Phys. Rev. Lett.*, 84:4276–4279, May 2000.
- [57] Ralph Engel et al. Test of hadronic interaction models with data from the Pierre Auger Observatory. *arXiv preprint arXiv:0706.1921*, 2007.
- [58] Alexander Aab, P Abreu, M Aglietta, EJ Ahn, I Al Samarai, IFM Albuquerque, I Allekotte, J Allen, P Allison, A Almela, et al. Muons in air showers at the Pierre Auger Observatory: Mean number in highly inclined events. *Physical Review D*, 91(3):032003, 2015.
- [59] A. V. Glushkov, I. T. Makarov, M. I. Pravdin, I. E. Slepsov, D. S. Gorbunov, G. I. Rubtsov, and Sergey V. Troitsky. Muon content of ultrahigh-energy air showers: Yakutsk data versus simulations. *JETP Lett.*, 87:190–194, 2008.
- [60] J. G. Gonzalez. Measurement of the Muon Content of Air Showers with IceTop. *J. Phys. Conf. Ser.*, 718(5):052017, 2016.
- [61] Yu A Fomin, NN Kalmykov, IS Karpikov, GV Kulikov, M Yu Kuznetsov, GI Rubtsov, VP Sulakov, and SV Troitsky. No muon excess in extensive air showers at 100–500 PeV primary energy: EAS–MSU results. *Astroparticle Physics*, 92:1–6, 2017.
- [62] Hans Dembinski. Investigating cosmic rays and air shower physics with IceCube/IceTop. In *EPJ Web of Conferences*, volume 145, page 01003. EDP Sciences, 2017.
- [63] RU Abbasi, M Abe, T Abu-Zayyad, M Allen, R Azuma, E Barcikowski, JW Belz, DR Bergman, SA Blake, R Cady, et al. Study of muons from ultra-high energy cosmic ray air

- showers measured with the Telescope Array experiment. *arXiv preprint arXiv:1804.03877*, 2018.
- [64] Federico Sanchez Sarah Müller, Markus Roth. Study of the muon content of extensive air showers with AMIGA data. Auger Analysis Meeting, Paris, June 06, 2017.
- [65] Alexander Aab, P Abreu, M Aglietta, EJ Ahn, I Al Samarai, IFM Albuquerque, I Allekotte, JD Allen, P Allison, A Almela, et al. Testing hadronic interactions at ultrahigh energies with air showers measured by the Pierre Auger Observatory. *Physical review letters*, 117(19):192001, 2016.
- [66] Stefano Argiro, SLC Barroso, J Gonzalez, Lukas Nellen, T Paul, TA Porter, L Prado Jr, M Roth, R Ulrich, and D Veberič. The offline software framework of the Pierre Auger Observatory. *Nuclear Instruments and Methods in Physics Research Section A: Accelerators, Spectrometers, Detectors and Associated Equipment*, 580(3):1485–1496, 2007.
- [67] ea WD Apel, JC Arteaga, AF Badea, K Bekk, M Bertaina, J Blümer, H Bozdog, IM Brancus, P Buchholz, E Cantoni, et al. The cascade-grande experiment. *Nuclear Instruments and Methods in Physics Research Section A: accelerators, spectrometers, detectors and associated equipment*, 620(2-3):202–216, 2010.
- [68] A Tapia, D Melo, F Sánchez, A Sedoski Croce, JM Figueira, B García, N González, M Josebachuili, D Ravnigani, B Wundheiler, et al. Study of the chemical composition of high energy cosmic rays using the muon LDF of EAS between $10^{17.25}$ eV and $10^{17.75}$ eV. *arXiv preprint arXiv:1501.02217*, 2015.
- [69] Ines Valino. The flux of ultra-high energy cosmic rays after ten years of operation of the Pierre Auger Observatory. *PoS*, page 271, 2015.
- [70] Pierre Auger Observatory. Measurement of the Energy Spectrum of Cosmic Rays between 0.1 EeV and 30 EeV with the Infill Extension of the Surface Detector of the Pierre Auger Observatory. *Internal Report GAP-2012-136*, 2012.
- [71] MARTA - Muon Auger RPC Tank Array. Second report on the Auger Data Challenge, 2014.
- [72] L Lopes, P Assis, A Blanco, N Carolino, MA Cerda, R Conceição, O Cunha, M Ferreira, P Fonte, R Luz, et al. Outdoor field experience with autonomous RPC based stations. *Journal of Instrumentation*, 11(09):C09011, 2016.
- [73] L Lopes, P Assis, A Blanco, MA Cerda, N Carolino, O Cunha, M Ferreira, P Fonte, L Mendes, M Palka, et al. Resistive plate chambers for the pierre auger array upgrade. *Journal of Instrumentation*, 9(10):C10023, 2014.
- [74] P. Fonte (LIP). MARTA RPCs. 8th MARTA Progress Meeting, March 14-15, 2016.
- [75] F Sanchez. The AMIGA detector of the Pierre Auger Observatory: an overview [173], 2011. *arXiv preprint arXiv:1107.4807*, page 5.
- [76] INAF INFN-Torino, IFSI-Torino and Italy University of Torino. About raining PMTs. *Internal Report GAP-2007-081*, 2007.
- [77] K. Arisaka M. Healy D. Barnhill W. Slater X. Bertou T. Yamamoto A. Chou A. Tripathi, T. Ohnuki. A Systematic Calibration of Surface Detectors using Muon Data from the Engineering Array. *Internal Report GAP-2002-046*, 2002.